NAM

Groningen 2015 Geomechanical Analysis

Suvrat P. Lele, Jorge L. Garzon, Sheng-Yuan Hsu, Nora L. DeDontney, Kevin H. Searles and Pablo F. Sanz (ExxonMobil Upstream Research Company, Spring, TX)

Date November 2015

Editors Jan van Elk & Dirk Doornhof

General Introduction

As part of the studies into induced seismicity in Groningen two geomechanical modelling approaches have been used:

1. Detailed modelling of rupture processes on a generic fault to improve our understanding of this process (Ref. 1 and 2).
2. Modelling of large sections of the field using realistic faults in the Groningen field.

This second modelling approach was started in the Upstream Research Centre of ExxonMobil during 2013 and initial results documented in the Technical Addendum with Winningsplan 2013 (Ref. 3). Since then these models covering large sections of the field haven been further developed.

The primary enhancements of these models are (i) improvements to FE models to include nearly all the mapped faults in the sub-model regions, (ii) inclusion of fault-offsets in the model, (iii) improved pore pressure mapping based on layer information in the reservoir model, (iv) addition of sub-model-3 to improve spatial coverage, and (v) integration with seismological model.

This report documents the further development of this model and the extension of the model to the assessment of seismic hazard. These new models improve the understanding of compaction and fault re-activation due to gas extraction.

References

1. Impact of various modelling options on the onset of fault slip and fault slip response using 2-dimensional Finite-Element modelling, Peter van den Bogert, July 2015
2. Induced seismicity in the Groningen field - statistical assessment of tremors along faults in a compacting reservoir, Rick Wentinck, July 2015.
3. Technical Addendum to the Winningsplan Groningen 2013; Subsidence, Induced Earthquakes and Seismic Hazard Analysis in the Groningen Field, Nederlandse Aardolie Maatschappij BV (Jan van Elk and Dirk Doornhof, eds), November 2013.

NAM

Title	**Groningen 2015 Geomechanical Analysis**		**Date**	November 2015
			Initiator	NAM
Autor(s)	Suvrat P. Lele, Jorge L. Garzon, Sheng-Yuan Hsu, Nora L. DeDontney, Kevin H. Searles and Pablo F. Sanz	**Editors**	Jan van Elk Dirk Doornhof	
Organisation	ExxonMobil Upstream Research Company, Spring, TX	**Organisation**	NAM	
Place in the Study and Data Acquisition Plan	Study Theme: Geomechanical Modelling Comment: As part of the studies into induced seismicity in Groningen two geomechanical modelling approaches have been used: 1. Detailed modelling of rupture processes on a generic fault to improve our understanding of this process (Ref. 1 and 2). 2. Modelling of large sections of the field using realistic faults in the Groningen field. This second modelling approach was started in 2013 and initial results documented in the Technical Addendum with Winningsplan 2013 (Ref. 2). Since then these models covering large sections of the field haven been further developed. The primary enhancements of these models are (i) improvements to FE models to include nearly all the mapped faults in the sub-model regions, (ii) inclusion of fault-offsets in the model, (iii) improved pore pressure mapping based on layer information in the reservoir model, (iv) addition of sub-model-3 to improve spatial coverage, and (v) integration with seismological model. This report documents the further development of this model and the extension of the model to the assessment of seismic hazard. These new models improve the understanding of compaction and fault re-activation due to gas extraction.			
Directliy linked research	(1) Reservoir engineering studies in the pressure depletion for different production scenarios. (2) Seismic monitoring activities; both the extension of the geophone network and the installation on geophones in deep wells. (3) Geomechanical modelling studies.			

	(4) Subsidence and compaction studies.
Used data	Reservoir Model, Compaction
Associated organisation	ExxonMobil Upstream Research Company, Spring, TX
Assurance	Within URC and by PTU staff.
References	1. Impact of various modelling options on the onset of fault slip and fault slip response using 2-dimensional Finite-Element modelling, Peter van den Bogert, July 2015 2. Induced seismicity in the Groningen field - statistical assessment of tremors along faults in a compacting reservoir, Rick Wentinck, July 2015. 3. Technical Addendum to the Winningsplan Groningen 2013; Subsidence, Induced Earthquakes and Seismic Hazard Analysis in the Groningen Field, Nederlandse Aardolie Maatschappij BV (Jan van Elk and Dirk Doornhof, eds), November 2013.

Groningen 2015 Geomechanical Analysis

Suvrat P. Lele
Jorge L. Garzon
Sheng-Yuan Hsu
Nora L. DeDontney
Kevin H. Searles
Pablo F. Sanz

ExxonMobil Upstream Research Company
Spring, TX

Table of Contents

Executive Summary

The present Groningen 2015 Geomechanical Analysis conducted by URC is a continuation of the 2013 study. The primary objectives were to develop a mechanics-based approach to understand subsurface behavior related to production-induced fault reactivation, and evaluate alternate production strategies that may help minimize fault slip. The 2013 model provided useful insights on the relation between compaction, fault slip and dissipated energy. At the end of 2013 study, it was recognized that additional improvements would help in better relating geomechanical attributes to seismic activity, which is the motivation for the current 2015 study.

The primary objectives of this 2015 study are (i) improvements to FE models to include nearly all the mapped faults in the sub-model regions, (ii) inclusion of fault-offsets in the model, (iii) improved pore pressure mapping based on layer information in the reservoir model, (iv) addition of sub-model-3 to improve spatial coverage, and (v) integration with seismological model.

New 2015 sub-models were developed to include nearly all mapped faults; the offsets at each fault are also explicitly included as part of the FE mesh. Sub-model-1 (North-West region of the field) and sub-model-2 (South-West region) cover the same region of the field as in 2013 study. Sub-model-3 was developed to improve spatial coverage to allow better integration with seismological models. The 2015 sub-models include nearly all mapped faults, with approximately 150 faults in each sub-model. Pressure mapping procedure used to map pore pressure data from NAM/Shell's MoRes reservoir simulator to the FE mesh has been improved using layer information from MoRes. Material properties of the thin heterolithic layers within the reservoir were changed to those of the surrounding reservoir rock from original undrained stiff properties to better represent this material. There are no changes in the global model; this model was developed and validated against field subsidence and strain data in the 2013 study.

The new models were used to better understand subsurface behavior related to production induced compaction and fault reactivation. Several production scenarios were analyzed and compared on a relative basis based on the predicted dissipated energy. The slip and contact force data for all FE nodes on the fault surfaces are used as input to the seismological models.

The 2015 model results show the fault offset is a key factor for production induced fault slip. A fault with offset can develop slip due to differential compaction on two sides even if the dip and azimuth are not favorable for fault slip. This leads to more slip on significantly more faults compared to that in 2013 models without offsets. Initial seismological model results based on slip data predicted by 2015 models show good correlation with observed seismic activity rate.

The geomechanical models rely on input parameters such as fault friction coefficient, rock properties and initial stress conditions that have some degree of uncertainty. To address the impact of these uncertainties, sensitivity analyses with a range of input parameters were undertaken which yield a range of outcomes. The use of quasi-static geomechanical models for predicting seismicity attributes is an evolving field and additional improvements or alternative correlations may be identified in future.

However, current model results are used to compare various production scenarios on a relative basis or for correlations in seismological modeling, and the parameters are expected to be consistent between scenarios.

URC is continuing work on improving the integration between the geomechanical models and seismological models for hazard and risk analysis.

1. Introduction and Background

The Groningen Gas Field in Northern Netherlands is the largest natural gas field in Europe with production started in 1963 and is operated by Nederlandse Aardolie Maatschappij BV (NAM), a 50/50 ExxonMobil/Shell gas producing company. Small seismic events were first observed in Groningen region in 1986, but these were generally small with minimal damage. A government study in early 1990's concluded that tremors were linked to gas production. Multiple additional government studies have recently been conducted to estimate probabilities of seismic events at Groningen (van Eck et al., 2006; Dost et al., 2012, Muntendam-Bos and de Waal, 2013). Seismic events with magnitudes up to 3.6 that lead to property damage were observed recently. In response to these events, the Minister of Economic Affairs of the Netherlands initiated a number of studies on production induced earthquakes in the Groningen area in a letter to the Parliament of the Netherlands dated February 11, 2013. To oversee the sub-surface study work done by NAM and to provide independent assurance, the Minister set up and confirmed the Technical Guidance Committee Sub-surface, Technische Begeleidingscommissie Ondergrond (TBO).

ExxonMobil Upstream Research Company (EMURC) conducted a geomechanics study in 2013 to analyze the effect of gas production on fault reactivation and evaluated various future production scenarios; this study supported two of the studies undertaken by NAM according to the directive from the Minister, (i) study TBO5 addressing "research into the maximum strength of earthquakes associated with the Groningen gas field", and (ii) study TBO6 addressing "research into different production methods to reduce the number and magnitude of earthquakes".

The present URC study is a continuation of the 2013 study, and includes improvements in FE models such as inclusion of nearly all mapped faults, fault offsets, and improved pore pressure mapping procedure. Results from the 2015 geomechanical models are used for integration with seismological models for prediction of seismic hazard.

1.1. Methodology

The geomechanical modeling methodology is based on load-resistance framework, wherein reservoir pressure changes due to depletion lead to deviation of the stress state from initial conditions (*load*) that may consequently lead to fault slippage governed by the frictional strength of the fault (*resistance*).

A multi-scale modeling framework that combined a large scale "global" model to characterize field wide behavior, and finer scale "sub-models" to understand fault slippage is utilized to investigate subsurface behavior resulting from different production scenarios

This methodology is summarized in Figure 1.1, and additional details about the methodology are included in URC 2013 study report (Lele et al., 2015) and Sanz et al., 2015.

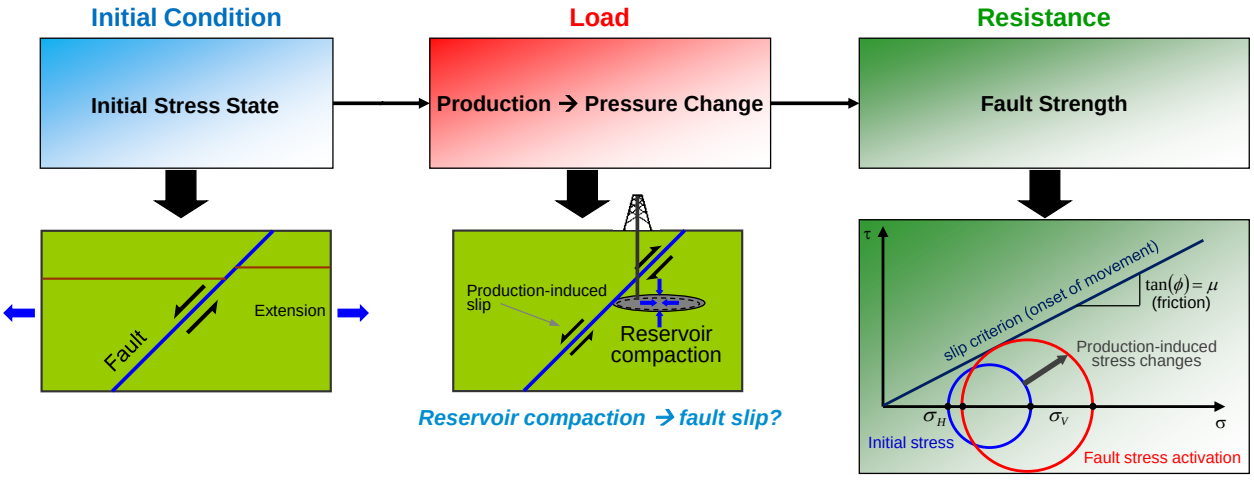

(a)

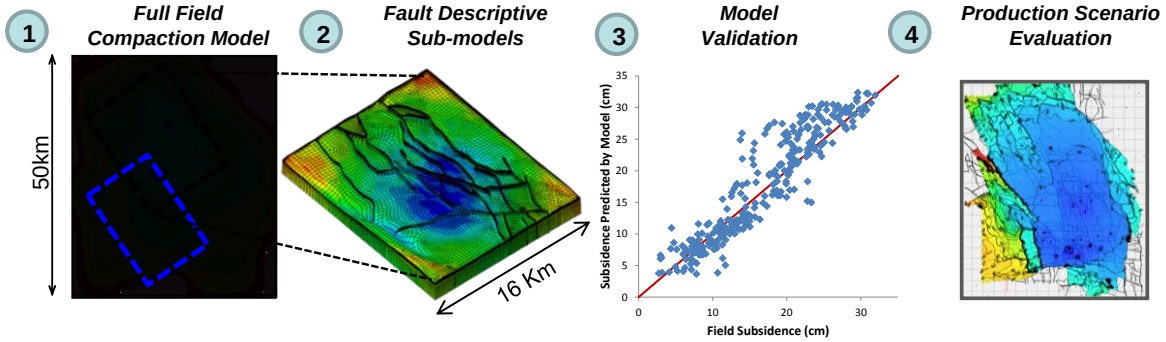

(b)

Fig. 1.1. (a) Load-resistance (pre-production in-situ stresses, production-induced stress changes and frictional strength of faults respectively) framework for fault stability and slippage modeling; (b) Geomechanical modeling workflow.

1.2. Assumptions and limitations

- FE analysis technique
  - Quasi-static analysis: The present study uses a quasi-static implicit time-integration analysis technique. Dynamic effects during seismic events cannot be modeled using this approach. Dynamic fault rupture process is also not modeled (e.g. Templeton et al., 2010; DeDontney, 2011). Hence, these analyses can predict the frictional dissipation energy due to fault slip, but cannot predict the seismic radiated energy or the seismic vs. aseismic components of predicted fault slip. Modeling of dynamic effects using explicit dynamic time-integration analysis over production time-scales (several years) and Groningen field length-scale is not feasible with current state of computational technology.
  - The mesh refinement used for the sub-models is limited by the current computational capability, and the results obtained may include some mesh-dependence. However, this is

not a significant limitation for the present study since results from the sub-models are used to (i) compare various production scenarios on a relative basis, and (ii) correlation with seismological model, and not for absolute prediction of seismicity directly.

- Fault Model
  - Fault friction coefficients cannot be determined from available test data, and hence sensitivity study with several friction coefficient values is conducted.
  - A rate-independent Coulomb friction model is used. Friction weakening or time-dependent friction has not been considered (e.g. Dieterich, 1978; Griffith et al., 2009).
  - Fault surface extensions or creation of new fault surfaces is not modeled.
  - Pore pressures inside the faults are not included. Distinct pore pressures on two sides of faults are mapped based on layer type on each side; the pore pressures inside faults are based on internal averaging by Abaqus.

- Geometry
  - The geological layer data from Petrel model provided by NAM is used to develop FE models. Minor differences in surface representations for horizons are expected due to differences in Petrel and FE grid.
  - Element size of 500m x 500m in horizontal planes is used for the full field global model. Element size of about 200m x 200m is used for the sub-models.
  - Meshing technique utilizes pseudo-zone material reassignment approach, with a uniform mesh created for the model domain that includes the faults, and geological material layers created later by assigning material properties based on location of the elements.
  - Fault surfaces are smoothened to ensure FE mesh with reasonable element size, quality and surface smoothness. Note that this smoothing did not significantly change overall fault geometry or dip angles. This has been verified by a comparison of FE mesh fault dip and azimuth with NAM/Shell data.
  - Faults geometry below the reservoir layer is not accurately known based on currently available seismic data. Therefore, faults are assumed to extend into the Carboniferous up to total vertical depth of 3.6 km with the same dip angle as in the reservoir layer.

- Material properties
  - Porosity values are up-scaled from Petrel data and mapped to FE mesh. The density, Young's modulus, Poisson's ratio, and Biot coefficient for the reservoir layers are dependent on porosity. A correlation between these properties and porosity is developed using test data (NAM, 2013b), and the material properties are defined to be dependent on the previously mapped porosity field in FE analysis.
  - These same porosity dependent material properties are also used for thin heterolithic layers within the reservoir. Additional details are included in section 2.6.
  - It is assumed that reservoir property variations are solely controlled by porosity, and that its stress-strain behavior is isotropic, and linear elastic.

- Errors in estimation of material properties are possible since the amount of available test data is limited.

- Initial stress state and reservoir pressure data
  - There is variability in available field data for initial stress state before production. Best estimate for horizontal stress gradients as provided by NAM are used.
  - The pore pressure data from MoRes reservoir simulator output is used as an input in geomechanical analysis. In regions near the boundaries of the rectangular FE model that are outside MoRes domain, static pore pressures based on constant water/gas pressure gradients were prescribed. Gradient of 1.166 bar/10m corresponding to water below depth of 2875m, and 0.18 bar/10m corresponding to gas above 2875m was used, with pore pressure of 350 bar at 2875m (NAM, 2013e). Note that all pore pressure degrees of freedom in FE analysis are constrained using pore pressure data from MoRes (or the static values outside MoRes domain); i.e. the FE analysis does not solve for fluid flow or any pore pressure values.
  - Reservoir pressure data, both initial values and those at selected time-intervals during production, are mapped from MoRes grid points to the FE mesh nodes using an algorithm based on weighted average of nearest neighbors with the weights proportional to the inverse of the square of distance.

1.3. Model inputs

The same material properties as those used in 2013 study are used, except the properties for the heterolithic layers, which are now assigned the same properties as the reservoir layer. Discussion about the modified properties for the heterolithic layers is included in section 2.6. A summary of the material properties is included below in Table 1.1, and Figures 1.2-1.5; additional details may be found in the URC 2013 study report (Lele et al., 2015).

Unit		Young's Modulus (GPa)	Poisson's Ratio	Density (kg/m^3)	Data Source
North Sea		2	0.3	2150	NAM
Chalk		10	0.25	2350	NAM
Rijnland		16	0.25	2350	NAM
Triassic		16	0.25	2350	NAM
Zechstein	Halite	30	0.35	2100	NAM
	Andydrite	70	0.25	2900	Literature
Ten Boer		40	0.2	2300	NAM
Slochteren	Heterolithic	Porosity-Dependent			Same properties as reservoir used
	Reservoir				Core Data
Carboniferous		40	0.2	2300	NAM

Table 1.1. Elastic material properties and densities for rock layers.

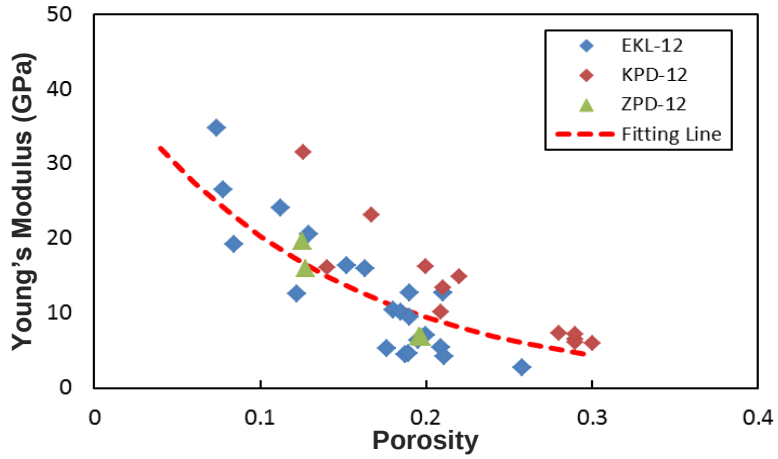

Fig. 1.2. Young's modulus vs. porosity of the reservoir rock.

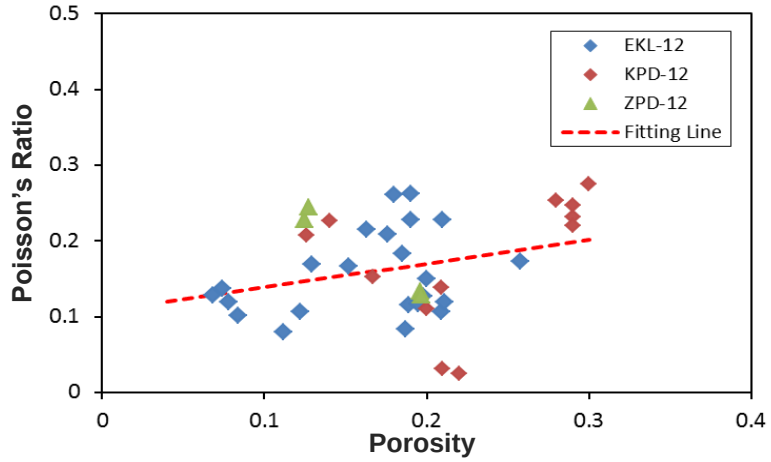

Fig. 1.3. Poisson's ratio vs. porosity of the reservoir rock.

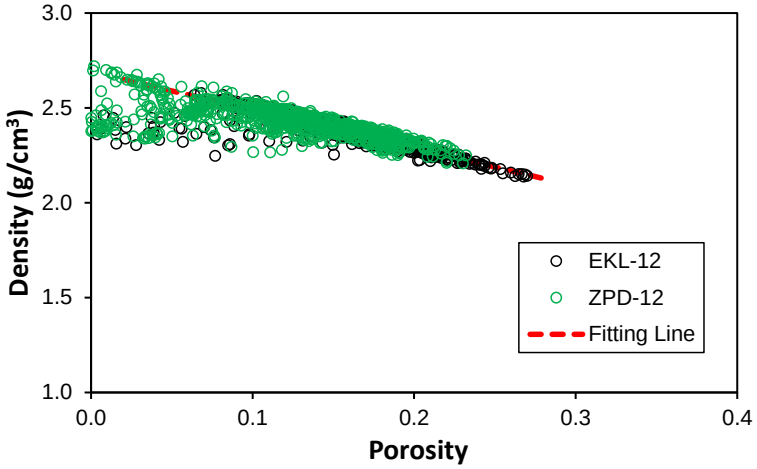

Fig. 1.4. Density vs. porosity of the reservoir rock.

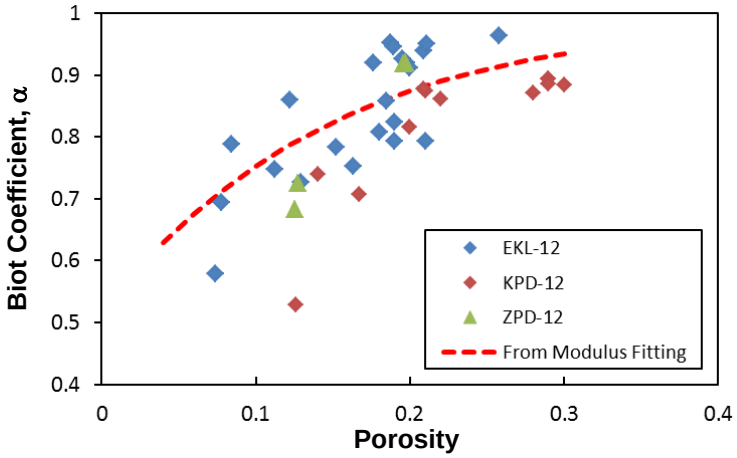

Fig 1.5. Biot coefficient vs. porosity for the reservoir rock.

The creep model used for Halite layers is based on Breunese et al, 2003 and NAM, 2013d. The total strain rate for this model is given by

$$\dot{\varepsilon}_{tot} = \dot{\varepsilon}_{dc} + \dot{\varepsilon}_{ps} = \underbrace{A_1 \sigma^n \exp\left(-\frac{Q_1}{RT}\right)}_{\text{dislocation creep}} + \underbrace{B \frac{\sigma}{Td^3} \exp\left(-\frac{Q_2}{RT}\right)}_{\text{pressure solution creep}}$$

where the first term represents dislocation creep and the second term represents pressure solution creep. The latter effect is dominant for production time scales (1964 – 2089). The dislocation creep term is ignored in this analysis. The parameters for this model are:

σ = deviatoric stress in MPa; Mises stress is used here

$B/(Td^3) = 14.6 \times 10^{-3}$ $MPa^{-1}day^{-1}$

$Q_2/R =$ 3007 K

T = 370 K

The initial stresses in the rock layers are defined using the following gradients (NAM, 2013e):

- Total vertical stress: 2.14 bar/10m
- Total maximum horizontal stress: 1.71 bar/10m
- Total minimum horizontal stress: 1.60 bar/10m

The maximum horizontal stress azimuth is 160° from North (NAM, 2013e; World stress map).

The pore pressures in FE model, including initial values and evolution with depletion associated with production history and forecast production scenarios, are based on predicted output from MoRes reservoir simulator (NAM, 2013f). The data at MoRes grid points are interpolated and mapped to the

nodes of the FE meshes for the global and sub-models. The pressure mapping procedure is improved compared to 2013 models to include separate mapping based on layer information. Additional details about this mapping are included in chapter 2.

1.4. Global model

The same global model as that used in 2013 study is used to capture overall field deformations, stress state and subsidence. This model does not include faults explicitly. Results from this model are used to prescribe displacement boundary conditions on the outer nodes of the sub-models, using the Abaqus sub-modeling approach.

1.5. Summary of 2013 study

The subsidence and reservoir strains predicted by the global model match well with field data without any calibration of material properties (Figures 1.6-1.8), i.e. directly using the material properties based on test data (for reservoir rock) summarized in section 1.3.

Figure 1.6 shows the contour plot of subsidence predicted by the model, and comparison with field data. An area that excludes 10km outer margins is used for field vs. model subsidence plot to reduce the effect of boundary conditions. A plot of errors in subsidence predictions is included in Figure 1.7. Note that the model predictions are most accurate in the regions with high observed seismicity.

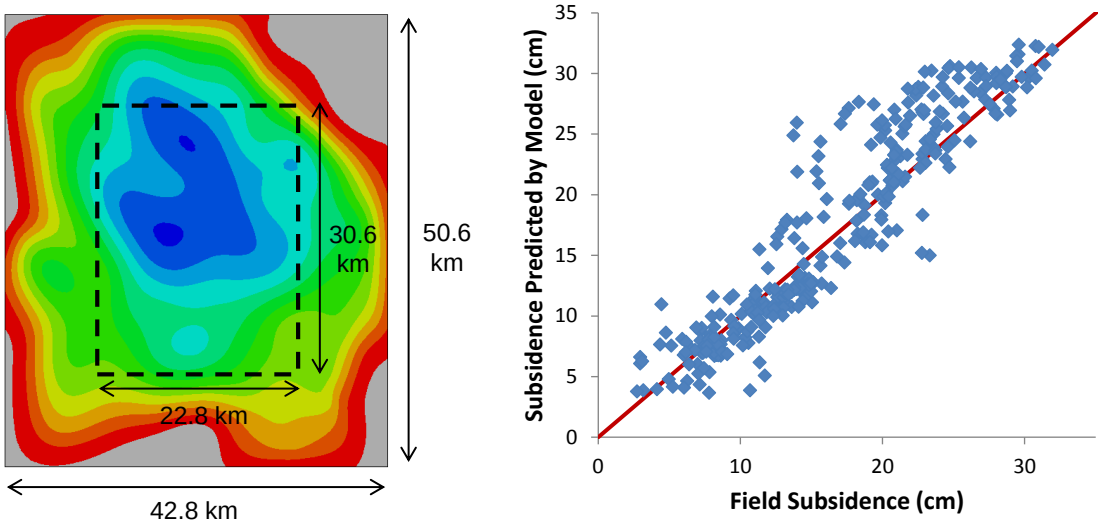

Fig. 1.6. Comparison of predicted vs. field subsidence in 2012 over the internal regions of the global model, excluding 10km bands near all boundaries.

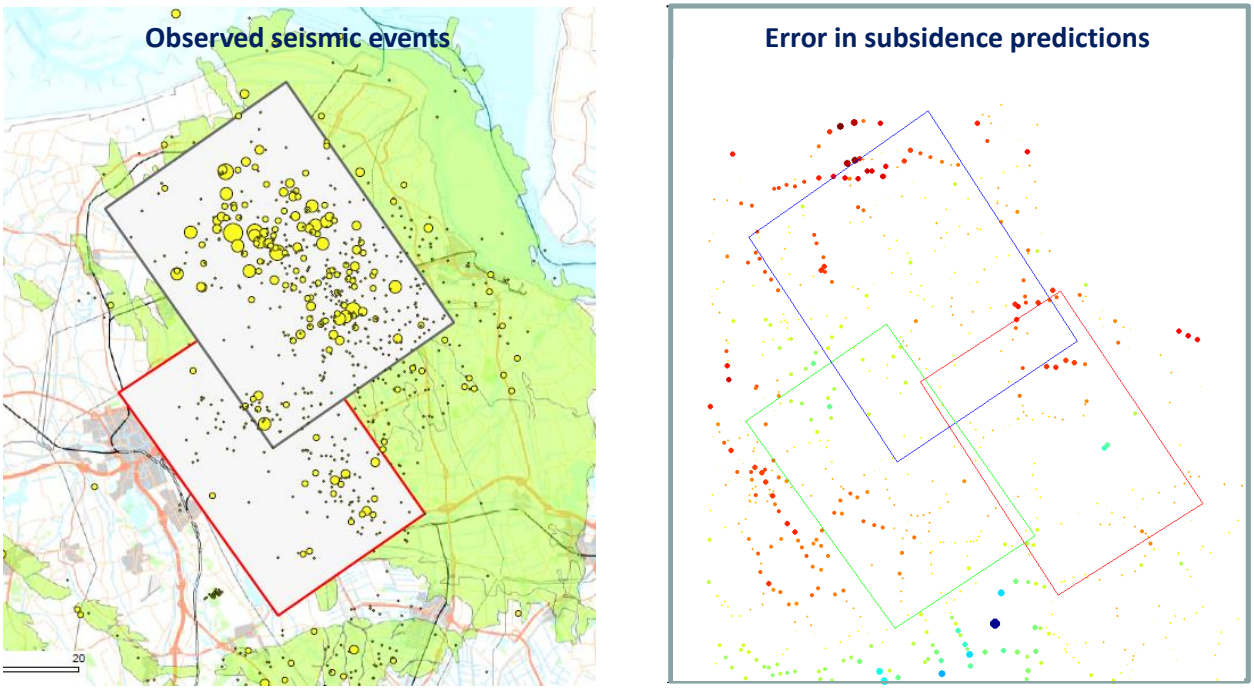

Fig. 1.7. Qualitative comparison of (a) Location map of observed seismic events and (b) Scatter plot of error in subsidence predictions in 2012; size of circles indicates magnitude of errors, blue-green colors indicate prediction lower than field data and orange-red colors indicate predictions higher than field data.

Reservoir strain data is available at three well locations. Comparison of model predictions with field strain data for one well location is included in Figure 1.8.

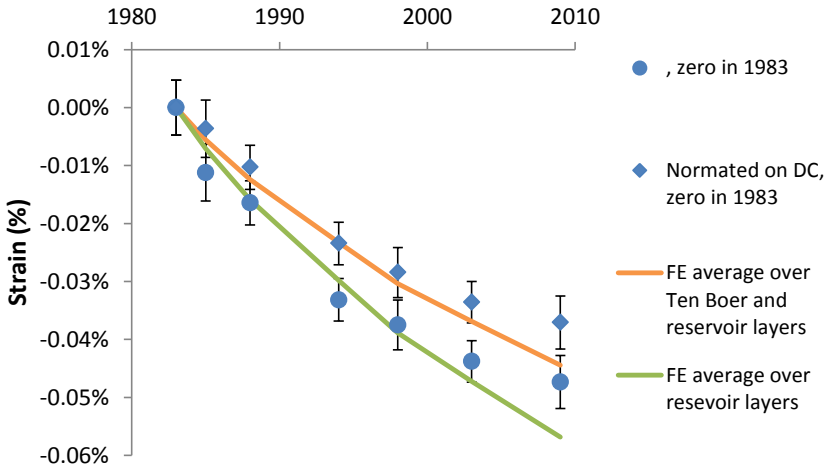

Fig. 1.8. Comparison of predicted average reservoir layer strain vs. field data (De Hond well location).

The 2013 Sub-models-1 and -2 were based on smoothed horizons across faults, i.e. without fault offsets. A cross-section of geological model in Petrel is compared with that of the FE model in Figure 1.9 to illustrate the horizon smoothing used in building FE mesh. The sub-model locations and FE meshes are shown in Figure 1.10.

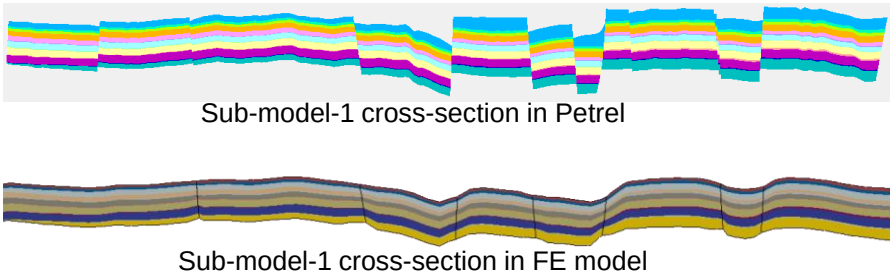

Fig. 1.9. Comparison of Petrel model cross-section with 2013 FE model (Abaqus) cross-section

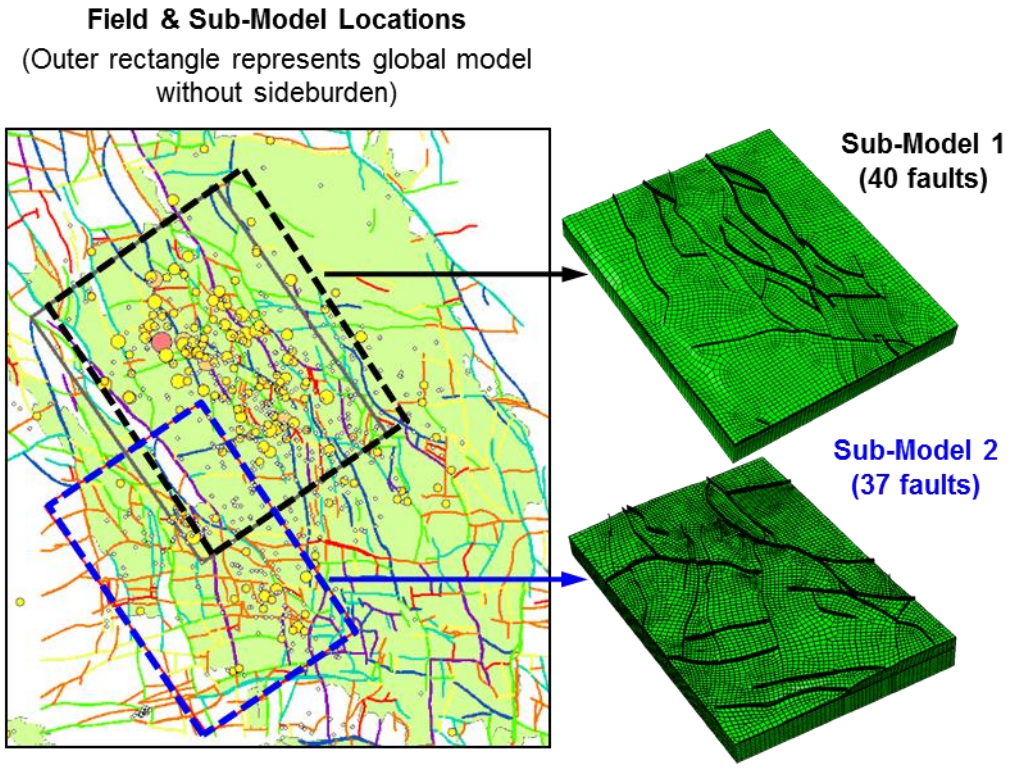

Fig. 1.10. Location and mesh details of 2013 sub-models

Predicted frictional dissipated energies from the two sub-models are correlated with observed seismic radiate energy in Figure 1.11. The dissipated energies from the two models correlate well with respective seismic energy using the same scaling factor for both sub-models.

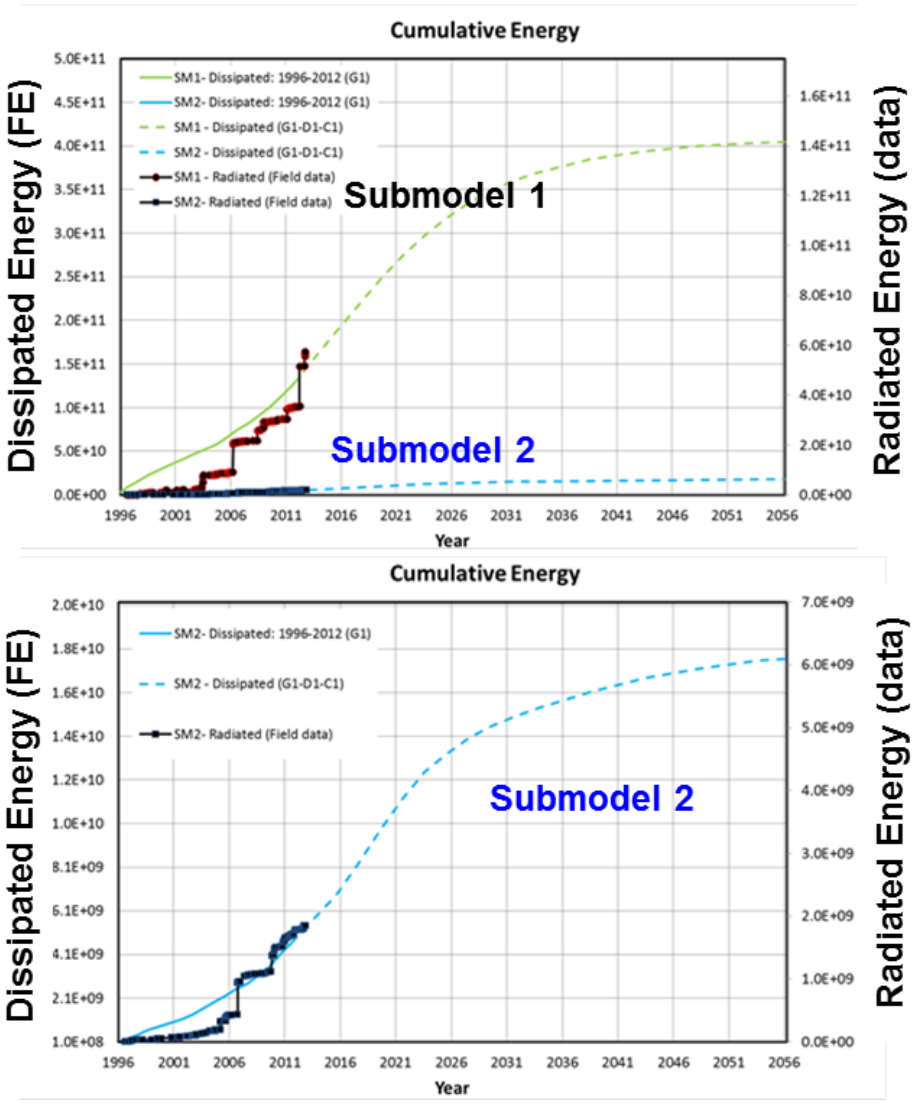

Fig. 1.11. Comparison of FE predicted dissipated energy with observed seismic radiated energy.

The 2013 models were used to analyze several production scenarios and rank those based on the predicted dissipated energy. The alternative production philosophy (A2) that lowered depletion of Northern reservoir while increasing depletion of the southern regions lowered the dissipated energy in sub-model 1 region, with only a slight increase in dissipated energy in sub-model 2 region. Since sub-model 1 region has observed considerably higher seismic activity compared to sub-model 2, this approach can be effective in reducing overall fault dissipated energy and therefore improving fault stability.

1.6. Outline of present work

The current 2015 URC study is a continuation of the 2013 work (Lele et al., 2015), with primary objectives of improvements in the geomechanical models such as inclusion of nearly all the mapped faults (approximately 140-150 in each sub-model, compared to approximately 40 in 2013), inclusion of fault-offsets and integration with seismological models.

The improvements in 2015 models compared to the 2013 models are discussed in Chapter 2. The behavior of 2015 FE models with fault offsets yield different results from the 2013 models for relative dissipated energies in the various sub-models and sensitivity to friction coefficients. These differences due to effect of fault offset on fault slip are analyzed in Chapter 3. Results from the FE analyses, the comparison of production scenarios and the effect of seasonal production, are presented in Chapter 4. Sensitivity studies for various friction coefficients, material properties and initial stresses are included in Chapter 5. Integration of the FE model results with seismological models is summarized in chapter 6. Additional details on the seismological model are included in a separate report (DeDontney et al., 2016). Chapter 7 includes a discussion on the conclusions of the present study and plans for future work.

2. FE Model Improvements

Leveraging work conducted in 2013, improved 3D finite element models were built that better represent complex geology and pressure fields from reservoir simulator:

- Models include almost all the faults mapped in Petrel
- Offsets across faults incorporated into models
- Improved pore pressure mapping procedure developed using layer information from MoRes grid; this procedure, combined with improved modeling of fault offsets, provides more accurate pressure field in geomechanical models
- More adequate mechanical properties for Heterolithic layers

2.1. Meshing technique

The meshes for sub-models in 2013 URC study were based on smoothed horizons, without fault offsets included explicitly. Simplified 2D analyses conducted by NAM/Shell (Van den Bogert, 2015) indicated that fault offsets can have a significant effect on the predicted fault slip onset, slip magnitude, and dissipated energy. Hence, objectives of URC 2015 study include improving the FE meshes to model the fault offsets, and addition of faults omitted in 2013 models so that nearly all of the faults mapped in the geological model are included. A new sub-model-3 was also developed to improve spatial coverage of the regions analyzed using sub-models. This allows prediction of slip behavior over most of the Groningen field domain, and provides a more complete spatial slip output for use in seismological models for hazard and risk analysis.

The three 2015 sub-models include 140-150 faults each; only a few small faults that were closer to other larger faults were omitted to simplify meshing and keep number of elements acceptable for use with current computation capability.

Generating meshes with elements conforming to each horizon for these complex models with ~150 faults, and with discontinuous horizons with offsets at each fault, is extremely time intensive and is not feasible within the timeframe of this study. Hence a simplified approach based on pseudo-zone material reassignment was developed. Meshes were created using only two horizons, one that defines the bottom of fault surfaces in the Carboniferous layer and one for top of the fault surfaces in Halite and/or Anhydrite layers. Note that there is large uncertainty regarding the bottom of faults in the geological models and the bottoms of fault surfaces extend to depth of 3600m, same as the approximation used in 2013 study. Additional underburden and overburden layers were added above and below this layer to reduce the effect of boundary conditions on fault slip.

Geological material layers were created after completion of the mesh, using material reassignment based on location of element centroids. A schematic representation of this approach, contrasted with the smoothed horizon approach used in 2013 study, is presented in Figure 2.1. This approach leads to slight errors in representation of the boundaries of geological layers, but greatly simplifies meshing and leads to significantly better mesh quality by avoiding bad aspect ratio elements at layer pinch-outs, and also reduced the total number of elements that are needed in the meshes. Both these factors, mesh quality and reduction in number of elements, are critical for allowing the analyses to complete without

convergence problems and within reasonable time duration; each case takes approximately one week total for model initialization, production history and forecast scenario analyses when running in parallel on 500 cpus.

The locations of these three sub-models relative to the Groningen field are shown in Figure 2.2. Additional details about FE meshes for each model are included in subsequent sections.

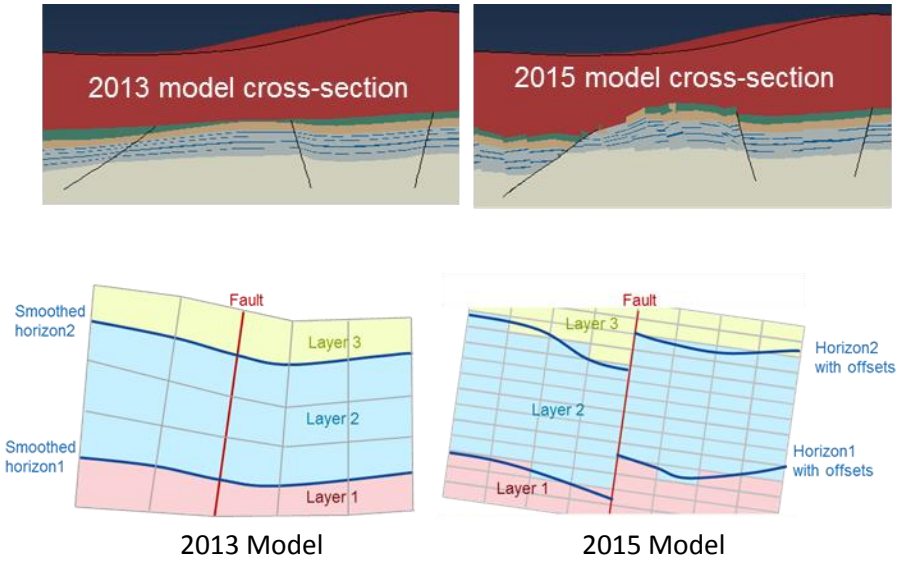

Fig. 2.1. Comparison of 2013 vs. 2015 meshing approaches: smoothed horizons with mesh conforming to the horizons in 2013 models and 2015 mesh where material properties are assigned later based on location of elements.

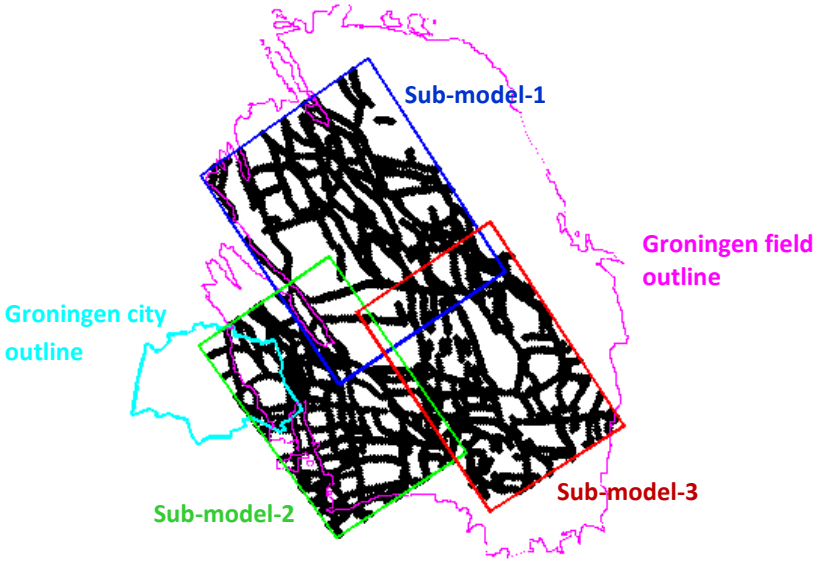

Fig. 2.2. Sub-models -1, -2 and -3 locations relative to the Groningen field and Groningen city outlines; faults included in the models are also highlighted.

2.2. Sub-model-1 mesh

Sub-model-1 covers an area of 16km x 20 km in the Northern part of the reservoir (see Figure 2.2). Most noticeably, this model domain includes the M1 fault, which is the fault with the maximum predicted slip magnitude and dissipated energy. The sub-model-1, illustrated in Figure 2.3 (a), is constructed with 588,692 elements, of which 511,442 (86.9%) are hexahedral brick elements and the remaining are triangular prism elements. The triangular prism elements are away from the faults to eliminate any effect on the solution convergence or accuracy.

The fault surfaces and resulting interaction of material layers on the two sides are modeled via contact pair definition approach in Abaqus. A contact pair can be a sub-set of fault surface due to meshing constraints. Because of the complex network nature of faults, the number of contact pairs defined is almost double the number of faults. For sub-model-1, there are 150 faults in this domain and 293 contact pairs are needed. Figure 2.3 (b) shows the network of faults and contact pairs; the underlying element layer in this sub-figure is the underburden representing Carboniferous formation.

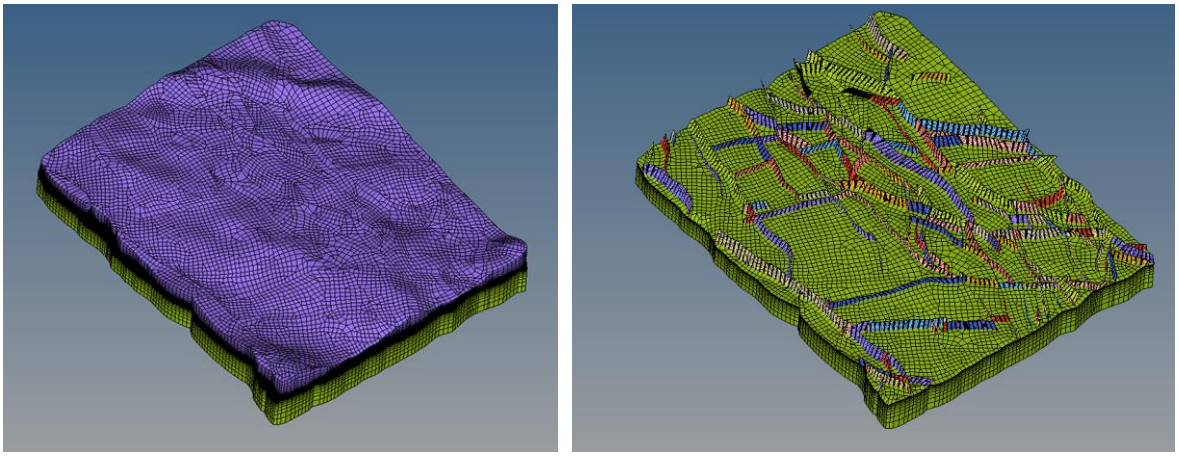

Fig. 2.3. (a) Sub-model-1 mesh, (b) fault contact surfaces highlighted

2.3. Sub-model-2 mesh

Sub-model-2 covers a region approximately 20 km x 12 km to the south-west of sub-model-1. The two models include a small overlap as seen in Figure 2.2. Part of Groningen City is included in the North-West corner of this sub-model. The faults near the South-West corner of sub-model-2 mark the boundary of reservoir. The fault offset is significant in this region, and can reach several hundred meters. There are 485,212 elements in sub-model-2, of which 422,776 elements are brick elements. The percentage of brick elements is 87.1%. The total numbers of faults is 141, and 263 contact pairs are required to define the contact surface interactions. The 3D rendering of sub-model 2 is illustrated in Figure 2.4 (a). The fault network and contact pairs are shown in Figure 2.4 (b).

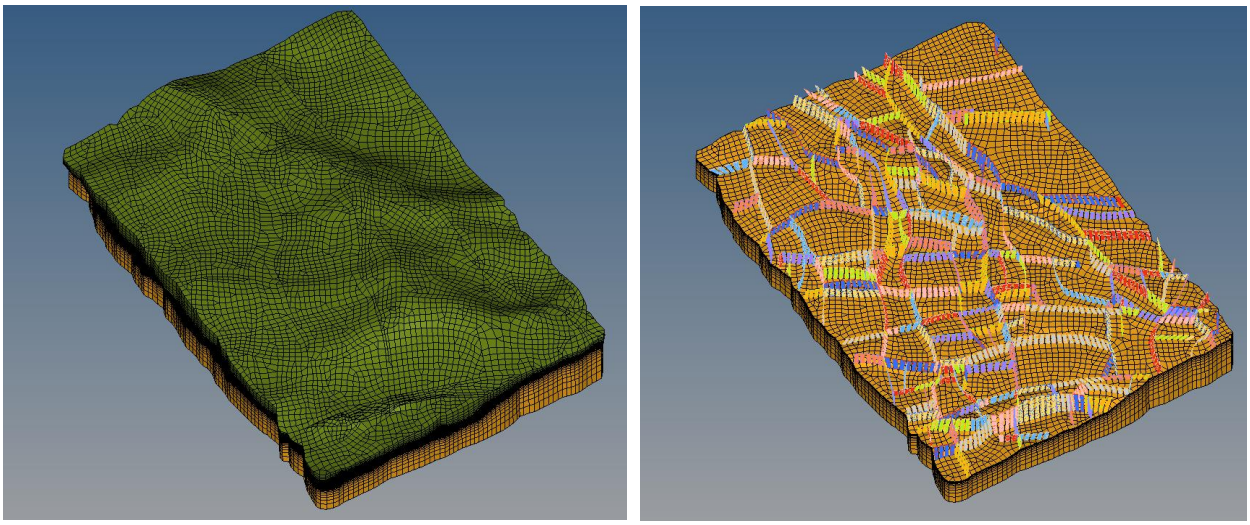

Fig. 2.4. (a) Sub-model-2 mesh, (b) fault contact surfaces highlighted.

2.4. Sub-model-3 mesh

Sub-model-3 is added in 2015 to extend areal coverage for the South-East area of the Groningen field to help in integration with seismological model. This model also covers a region approximately 20 km x 12 km. It was not considered in the work scope of study in 2013, since this area had experienced low seismic activity compared to other regions. The reservoir thickness in sub-model-3 region is lower compared to the other two sub-models. There are 468,958 elements in the mesh of this sub-model, of which 410,650 elements (87.6%) are brick elements. There are 125 faults, and 307 contact pairs are used to define the contact surfaces. Figure 2.5 (a) shows the 3D rendering of the FEA model, and Figure 2.5 (b) shows the fault network and contact pairs.

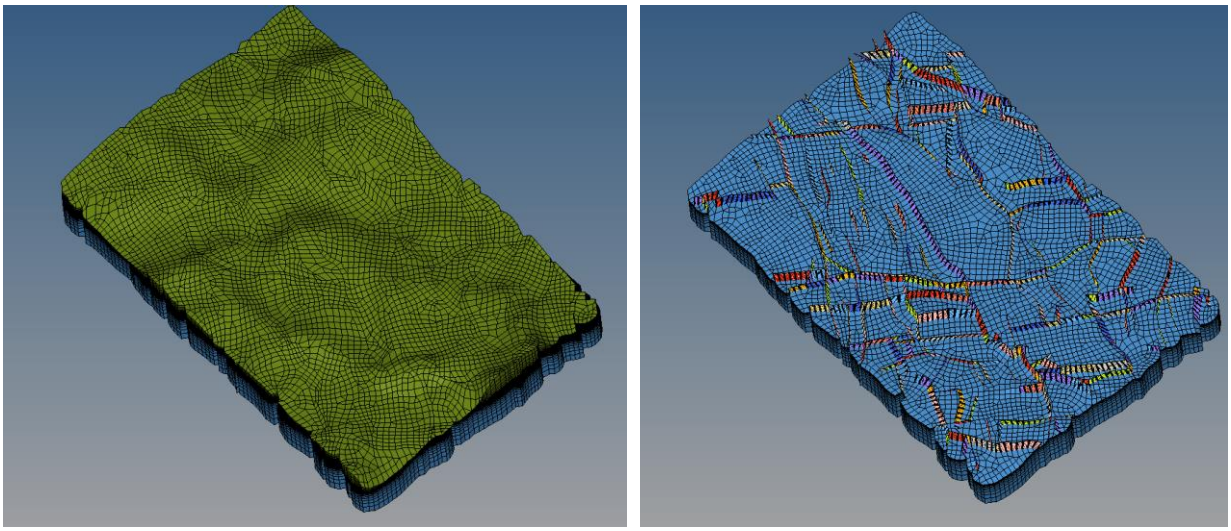

Fig. 2.5. (a) Sub-model-3 mesh, (b) fault contact surfaces highlighted.

2.5. Improved pressure mapping

In addition to improvements to meshes to include more faults and fault offsets, the approach used to map pore pressures from MoRes reservoir simulator data provided by NAM/Shell to Abaqus FE mesh was also improved using layer information from MoRes grid. This procedure, combined with improved modeling of fault offsets, provides more accurate pressure field in geomechanical models. A comparison of the pore pressure contour plot at the same cross-section location from the 2013 and 2015 models is shown in Figure 2.6.

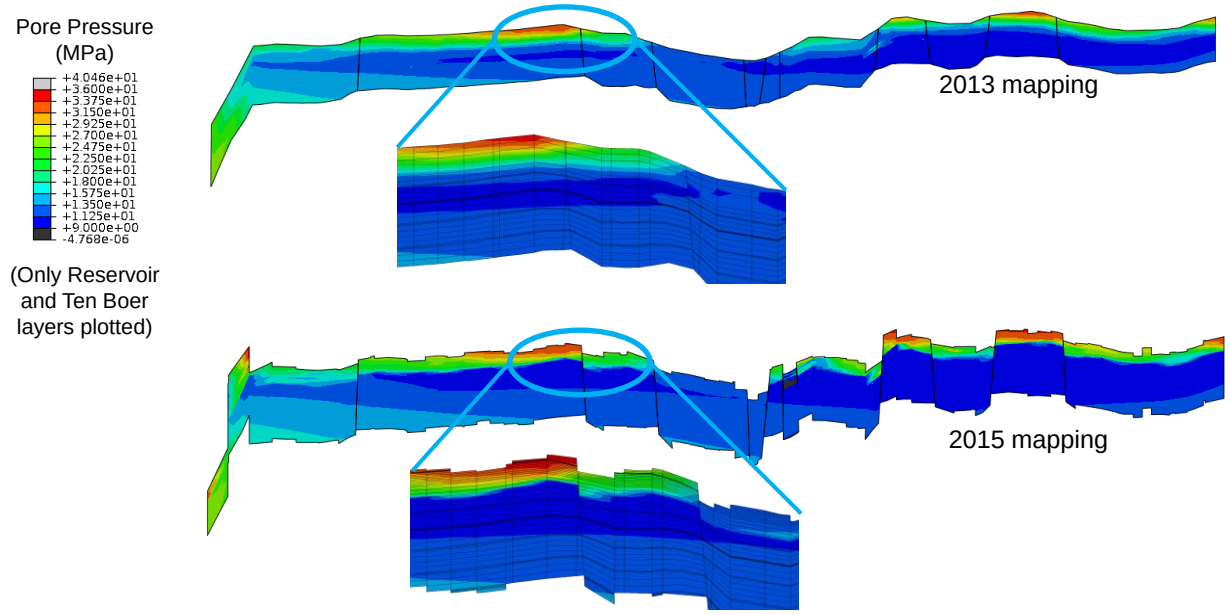

Fig. 2.6. Comparison of pore pressure mapping in 2013 and 2015 models at the same location; note that meshes are also different; more faults and fault offsets are included in 2015 model.

2.6. Heterolithic layer material properties

The material properties provided for the heterolithic layer in 2013 were the undrained properties, with Young's modulus of 36 GPa, or over 2x stiffer compared to the average reservoir rock. While properties for these thin layers did not affect the results in 2013 model without offsets, this stark contrast in stiffness led to numerical contact issues in the new 2015 models that include fault offsets. Due to the presence of offsets, the material properties on the two sides of the fault can be significantly different. And this large variation due to presence of these very thin and stiff heterolithic layers led to slip profiles that did not appear physically realistic. Moreover, there is no physical basis for the heterolithic layers to be so stiff based on examination of core samples, wherein these layers are very hard to pick out from the neighboring reservoir layers. Additionally, FE analysis with pore pressures requires drained material

properties. Due to these reasons these heterolithic layers were assigned the same properties as surrounding reservoir layers. A comparison of slip contour plots with original undrained properties for heterolithic layers, and with same porosity dependent properties as the reservoir is included in Figure 2.7. Note the patchy slip pattern along vertical direction across faults with former stiff properties, and smooth profile in the latter case.

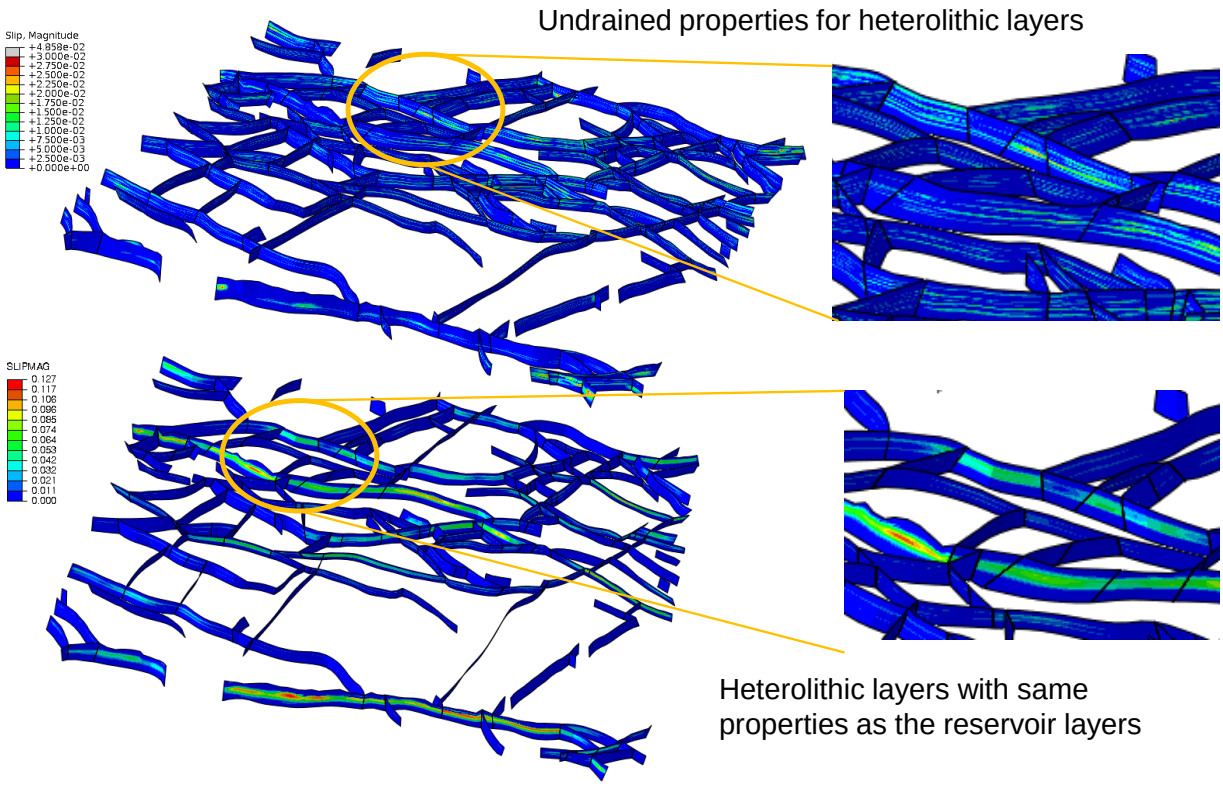

Fig. 2.7. Comparison of sub-model-1 slip magnitudes (m) for end of year 2014 for friction coefficient 0.48; with original undrained properties for heterolithic layers, and with properties that are same as the surrounding reservoir layers.

2.7. Sub-models verification

As discussed in section 1.5, the global models have been validated using field subsidence and reservoir strain data. Due to non-availability of slip data, the sub-modeling workflow is verified by comparing the stresses, displacements and pore pressures with the global model.

Figure 2.8 shows the comparison of initial stresses (1964) between the global and the three sub-models. The contour plots correspond to top of reservoir layer USS_2_RES. Comparison of stresses in 2014 is shown in Figure 2.9. Horizontal displacements comparison is presented in Figure 2.10. Overall there is good agreement between the stresses and displacements in the sub-models and the global model; there are some differences at fault locations since faults and offsets are not included in the global model.

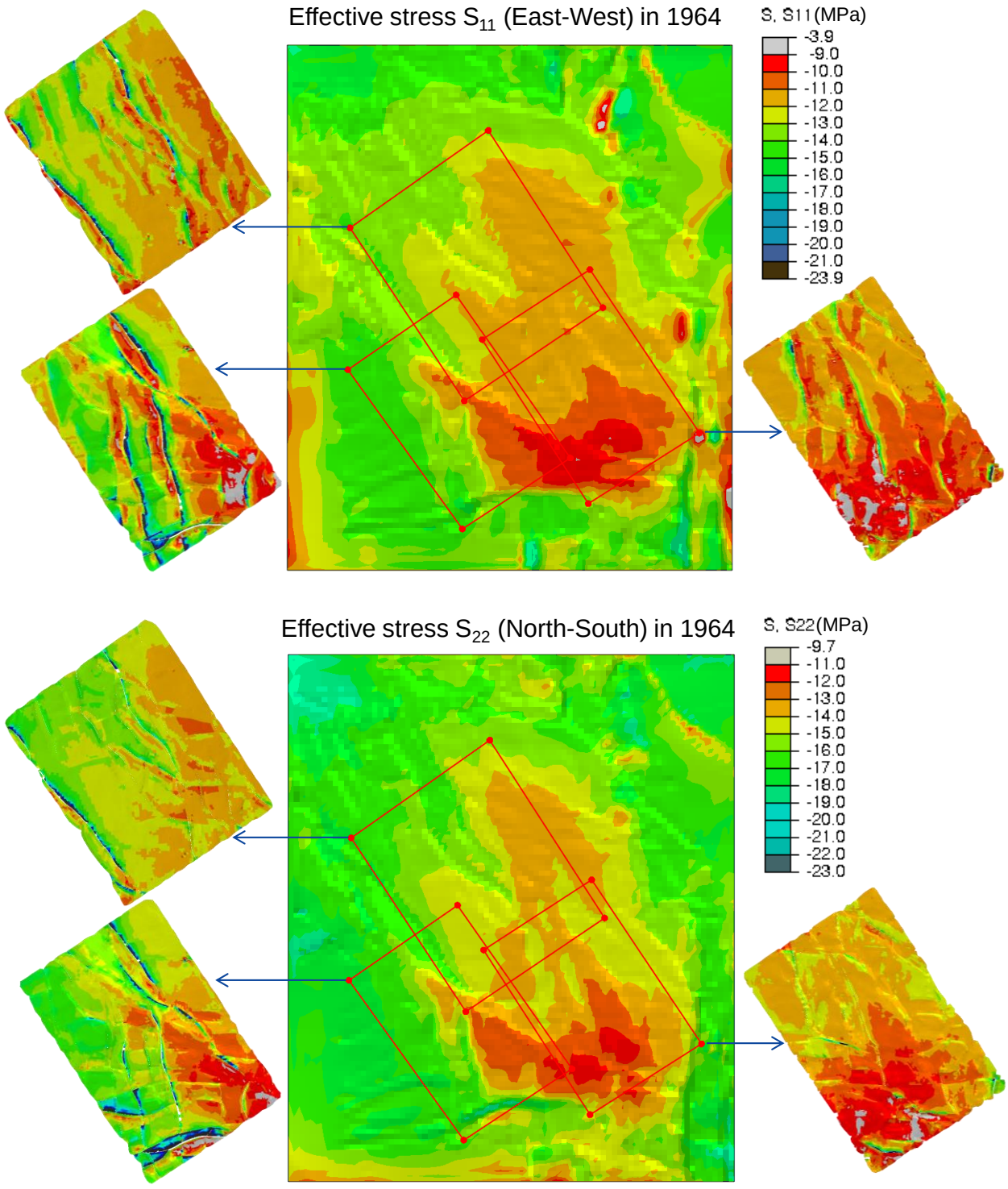

Fig. 2.8. Comparison of initial horizontal stress components (year 1964) for the three sub-models and the global model; contour plots for top of reservoir layer USS_2_RES. Note that global model has smoothed horizons across the faults, and fault offset in sub-models are responsible for additional stress perturbations.

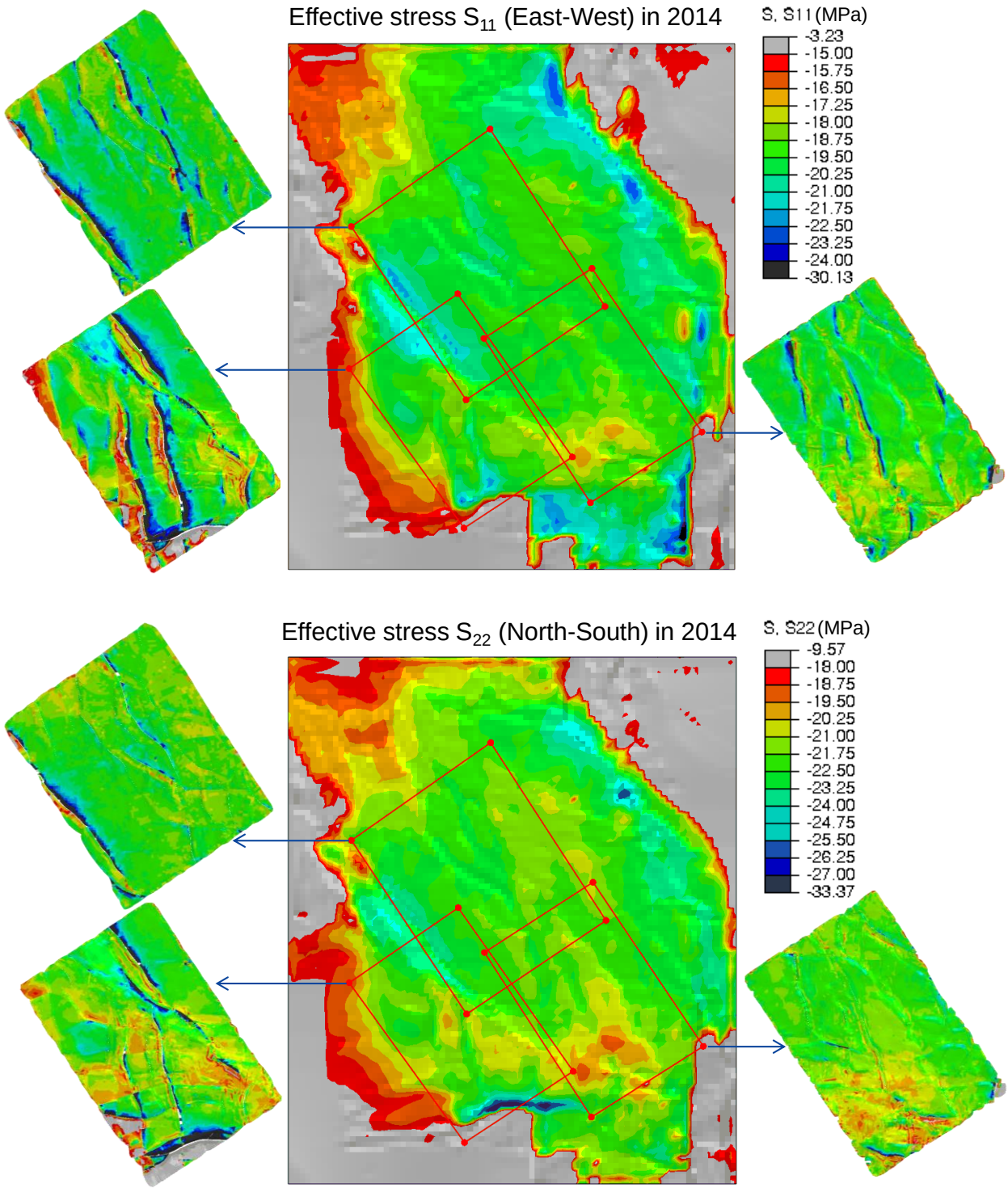

Fig. 2.9. Comparison of horizontal stress components in year 2014 for the three sub-models and the global model; contour plots for top of reservoir layer USS_2_RES.

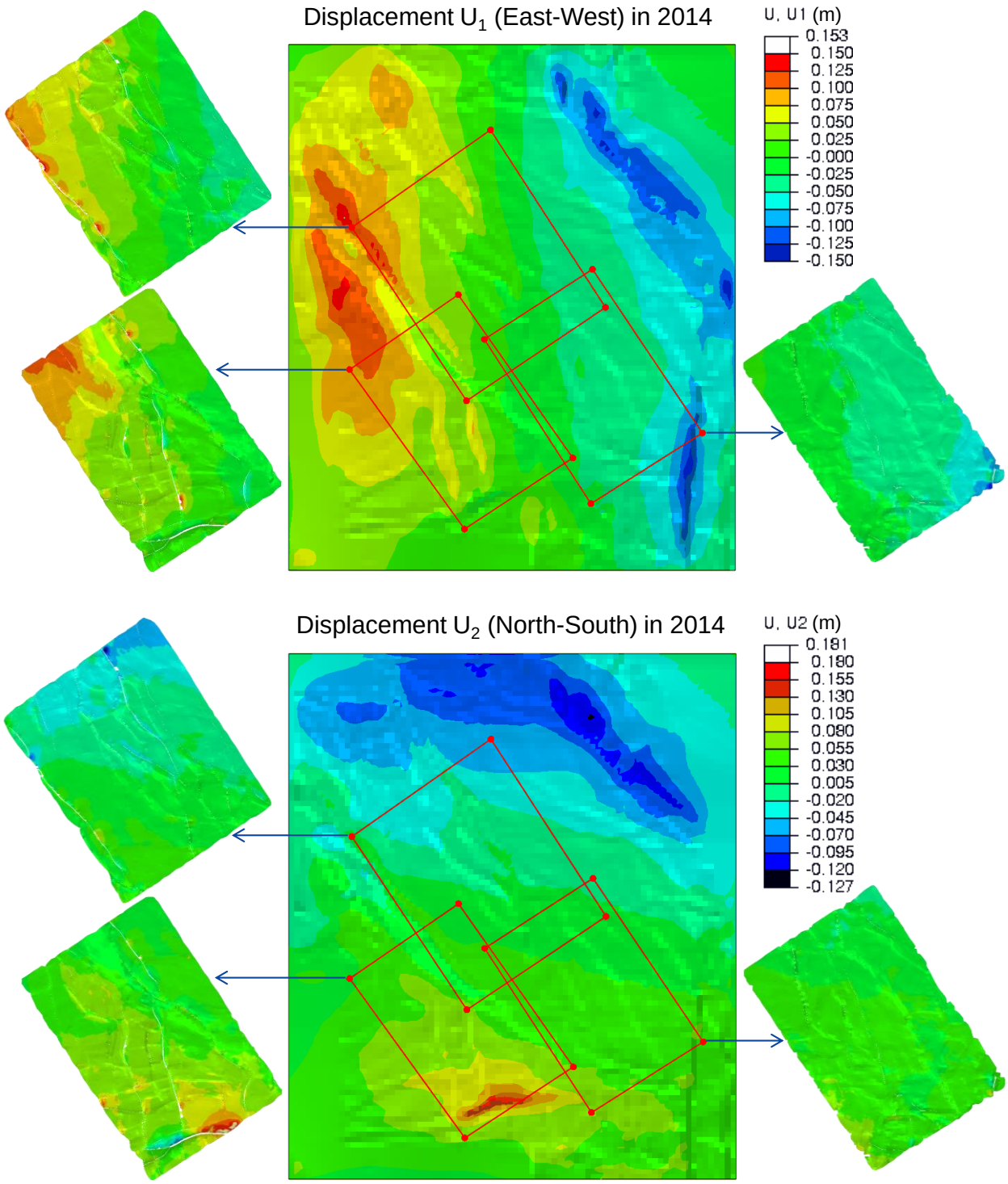

Fig. 2.10. Comparison of horizontal displacements in year 2014 for the three sub-models and the global model; contour plots for top of the reservoir layer USS_2_RES.

The pore pressures in both models are mapped from MoRes reservoir simulator data. Figure 2.11 shows the comparison of the pore pressures. Note that the 2015 sub-models include fault offsets that are not explicitly included in the global model, and the pressure mapping procedure in 2015 models is improved using layer information from the MoRes simulator. This leads to slightly smoother pore pressure contours in the sub-models for a reservoir layer. Overall match between the pore pressures in the sub-models and the global models is good.

This good agreement between sub-model and global model stress fields, displacements and mapped pore pressures serves as verification of correct sub-model initialization and the sub-modeling workflow.

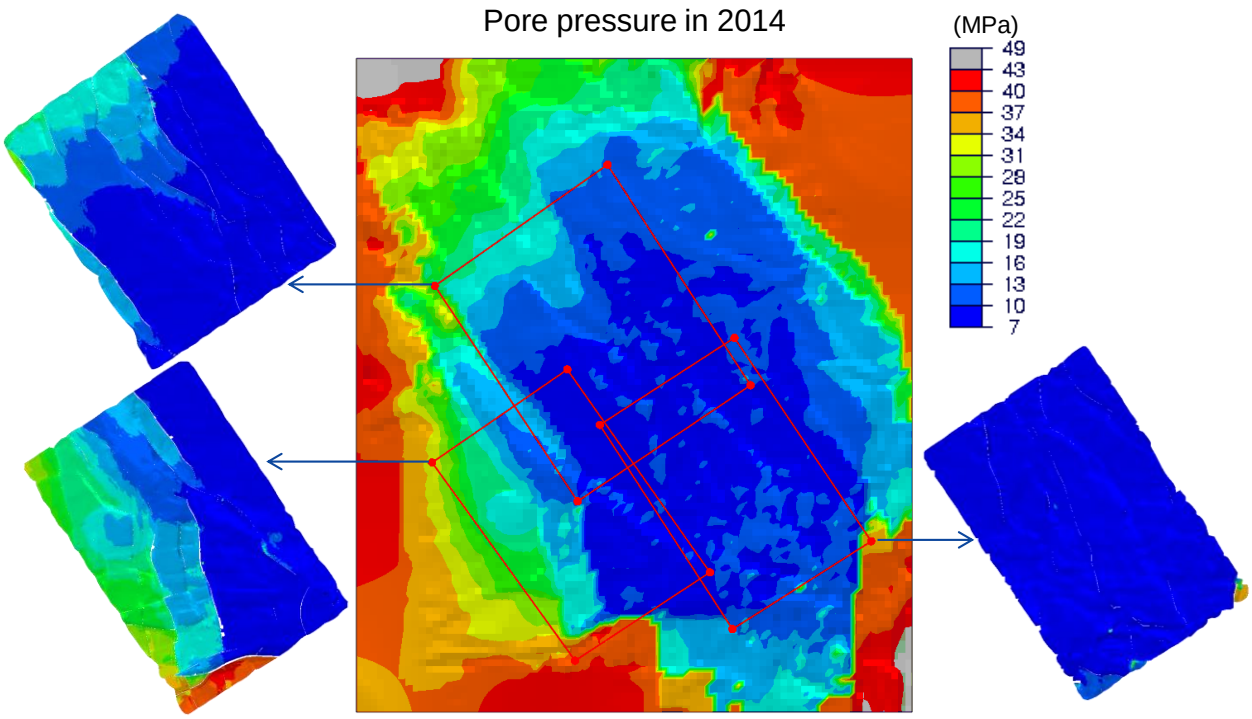

Fig. 2.11. Comparison of pore pressures in 2014 for the three sub-models and the global model; contour plots for top of the reservoir layer USS_2_RES.

3. Analysis of FE Model Behavior with Fault-Offsets

A primary objective of 2015 study was to include more faults and fault-offsets in the sub-models, since 2D studies by NAM/Shell indicated that offsets can have significant effect on fault slip. Results from the present 2015 3D geomechanical sub-models confirm this behavior. However, in addition to the slip and dissipated energies being higher compared to 2013 models without offsets, their trends are different when the sub-models are compared with each other. These trends and detailed analysis of the model behavior is presented in this chapter to understand the effect of offsets on the results of these models.

3.1. Effect of fault offsets

Inclusion of fault offsets can lead to significantly more slip compared to the models without offsets, as illustrated in Figure 3.1. In case (i) there is no slip due to compaction, since layers on both sides move by the same amount. In case (iv), the offset leads to large slip in two locations for the same amount of compaction. Cases (ii) and (iii) are intermediate cases where compaction may lead to small slip without offset.

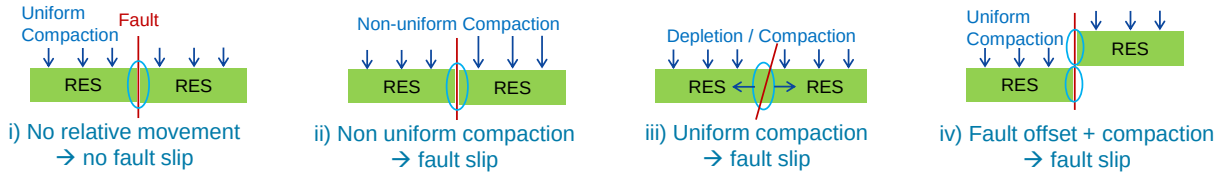

Fig. 3.1. Schematic representation of effect of offset on fault slip.

Due to this higher slip, possibly at more locations, dissipated energy predicted by the 2015 sub-models is expected to be higher compared to 2013 models. The energies for HM1 history match period up to 2012 for the two 2013 sub-models and the three 2015 sub-models are shown in Figure 3.2.

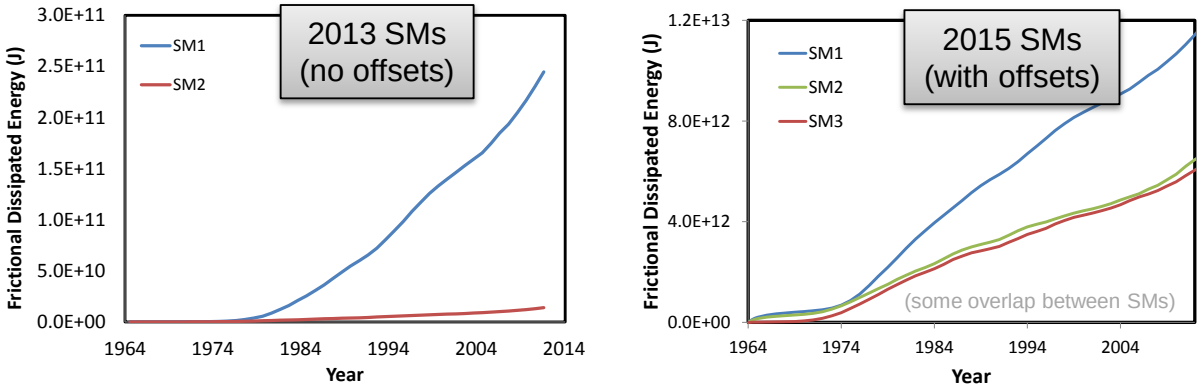

Fig. 3.2. Dissipated energy for HM1 history match period for 2013 and 2015 sub-models.

The dissipated energy for 2013 sub-model-2 was ~ 20x lower compared to that for 2013 sub-model-1, and, as mentioned in section 1.5, these energies could be correlated with seismic radiated energies for the corresponding regions using the same scaling factor for both models.

However, the energies for 2015 sub-model-2 and -3 are about half of that for sub-model-1. Because there is substantially less actual seismicity in sub-model-2 and -3 regions, a common scaling factor for correlating these energies to seismic radiated energy does not work. Note that sub-model regions include some overlap, leading to a small amount of energy being counted in more than one sub-model; however, this overlapping portion of energies is small, ~ 5-10% of the total, and will not significantly affect this relative comparison between models.

This discrepancy is likely due to higher slips driven by fault offsets as mentioned above. In 2013 models, fault slip developed only if the fault azimuth and dip lead to a stress field favorable for slipping. For example, a vertical fault as shown in Figure 3.1 would likely not develop slip in 2013 model, but will slip when offsets are included. A schematic representation of the associated dissipated energies for these two mechanisms is shown in Figure 3.3; the "blue" part shows energy due to stress-state based slip, and the "orange" part that due to offset-based slip. Note that this is schematic representation only – the model only predicts total dissipated energy and it is not possible to separate it into such two parts. Since all sub-models include faults with large offsets, the "orange" part of the energy can be much larger than the "blue" part and bring the overall energies for all three sub-models much closer to each other. This behavior is different from 2013 models, wherein the offsets were not included, and all slip was stress-state based, or corresponding to "blue" part only, which varied significantly between the different sub-models.

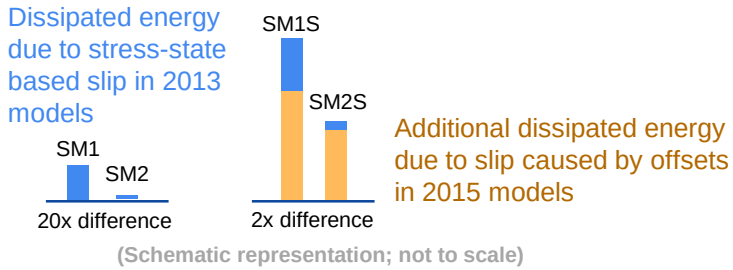

Fig. 3.3. Schematic representation of stress-state based and offset-based slip dissipated energy

The new sub-models, SM1S, SM2S and SM3S, include more faults compared to the 2013 sub-models, SM1 and SM2. In order to directly compare effect of offsets based on models with same number of faults, a "hybrid" model SM1H based on the 2013 model mesh refined in vertical direction and fault offsets included using material reassignment approach was constructed. Predictions from this model are compared with the 2013 SM1 model without offsets below. Note that the hybrid model is used only for this comparison here; all results included in the latter sections of this report are based on the new 2015 models with more faults.

Figure 3.4 shows comparison of the dissipated energy from SM1 and SM1H models, both with 40 faults, but without and with offsets respectively. The dissipated energy in the model with offsets is ~10x higher

than that without offsets. This result is consistent with above discussion about offsets leading to higher slip due to differential compaction.

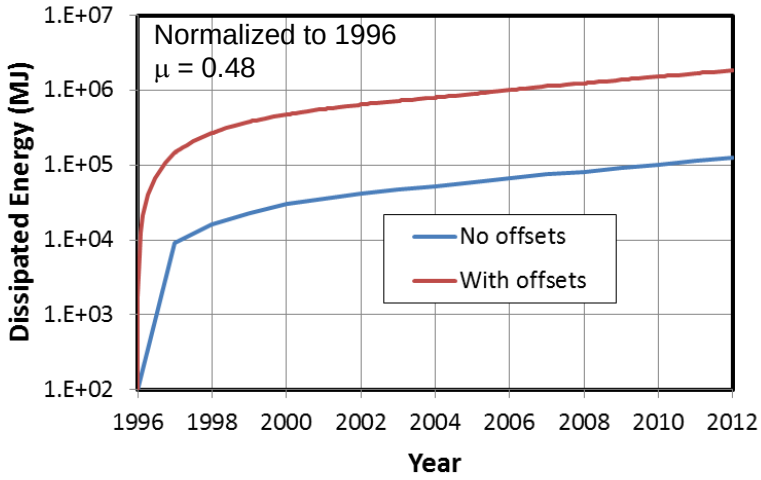

Fig. 3.4. Comparison of dissipated energy for 2013 SM1 model and "hybrid" SM1H model with same number of faults, but with offsets included using material reassignment approach.

The dip-slip and strike-slip components of the slips for the two models are shown in Figure 3.5. Note that dip-slip component is higher in the model with offsets, since differential compaction based slip at offsets is likely to have higher dip-slip component.

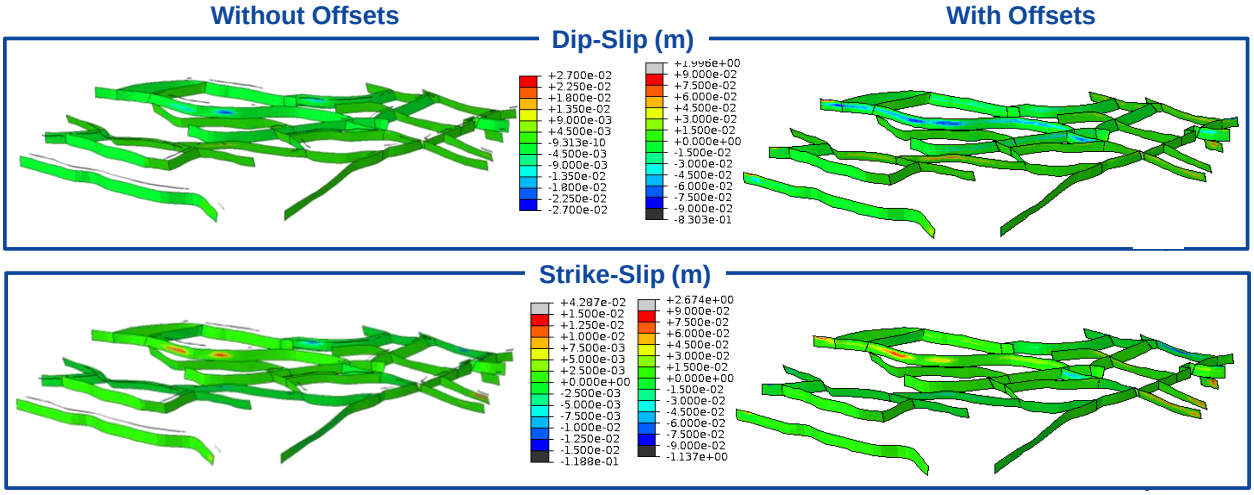

Fig. 3.5. Dip-slip and strike-slip components compared for models SM1 model without offset and SM1H model with offsets.

The components of dissipated energy associated with dip-slip and strike-slip components are compared in Figure 3.6. Consistent with higher dip-slip in the model with offsets, the dissipated energy component associated with dip-slip is also higher for that model.

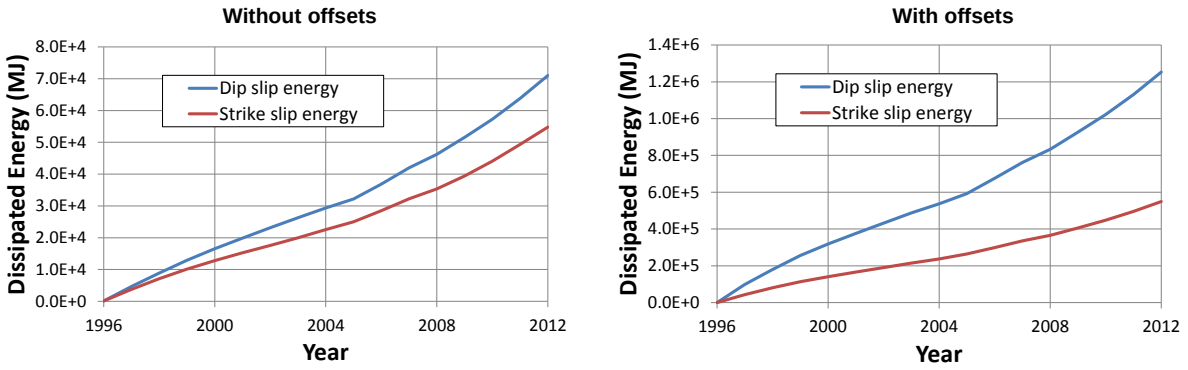

Fig. 3.6. Dissipated energy components associated with dip-slip and strike-slip compared for SM1 model without offset and SM1H model with offsets.

Again note that the hybrid model which has the same number of faults as the 2013 SM1 model is used only for above comparisons here; all subsequent results included in this report are based on the new 2015 models with more faults.

3.2. Statistical Analysis to compare effect of fault and reservoir parameters

As discussed in section 3.1, the dissipated energy for 2015 models with offsets and more faults is significantly higher compared to that for 2013 models without offsets. Additionally, the relative difference between the energies for the different sub-models is much lower in 2015 models compared to that in 2013 models. This is likely due to additional slip at offsets induced by differential compaction; however, the models are complex in terms of geometry (horizons, fault azimuth, dip, offsets), material properties, and reservoir attributes and compaction. A statistical analysis of effect of fault and reservoir parameters on the model slip is presented in this section to understand importance of these factors on FE model results.

Shell/NAM have provided fault dip, azimuth, offset and reservoir thickness data at several points along the faults. Approximately 15000 of these points are in the three sub-model regions. Slip magnitudes predicted by FE models are mapped to these points using an interpolation script developed in Matlab. This mapped dataset can be used for statistical analysis to understand the effect of fault and reservoir parameters on FE model slip. These slips mapped to Shell/NAM's fault data locations are shown in Figure 3.7.

Plots of FE slip magnitude vs. various individual parameters are shown in Figures 3.8 and 3.9. These plots show that dependence of slip on these parameters is complex and likely to depend on interaction of these parameters. Relative importance of the fault and reservoir parameters and possible interactions of these parameters is not obvious from these plots, and additional statistical regression analysis is necessary to reveal any possible trends.

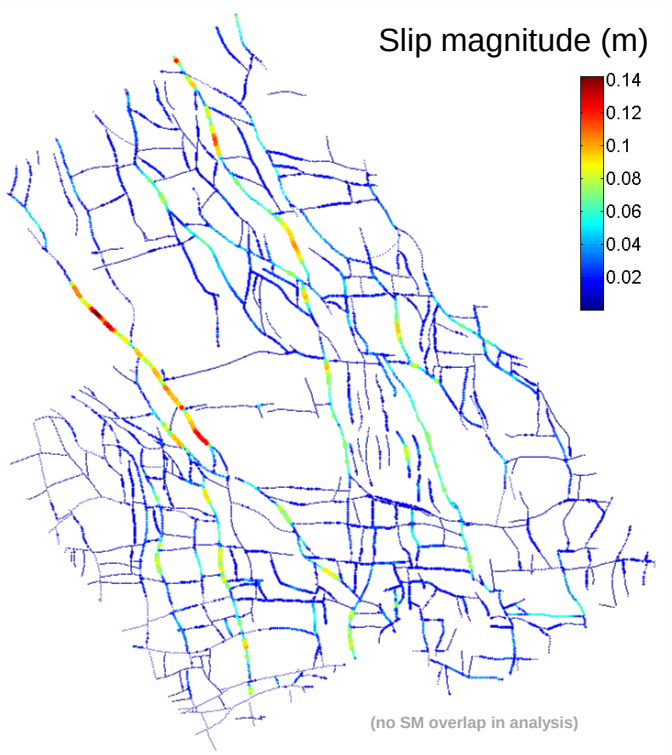

Fig. 3.7. Slip predicted by FE sub-models mapped to points with fault data provided by Shell/NAM; friction coefficient 0.48.

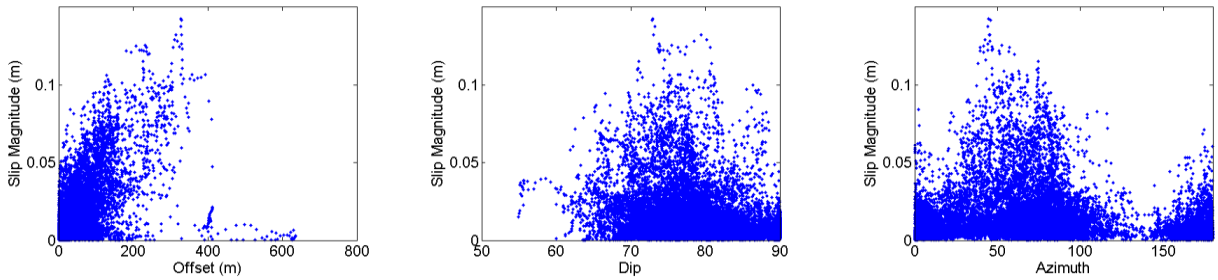

Fig. 3.8. FE slip magnitude vs. fault offset, dip and azimuth.

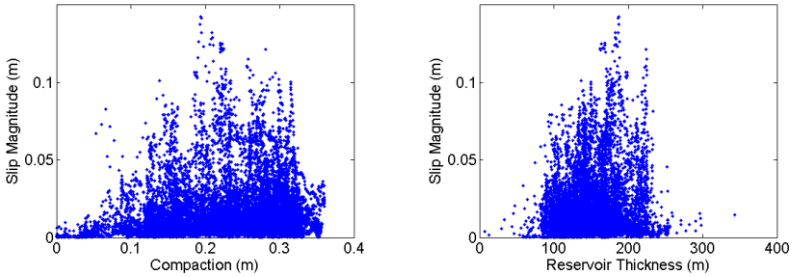

Fig. 3.9. FE slip magnitude vs. compaction and reservoir thickness.

Figures 3.10 and 3.11 show plots of fault and reservoir parameters and slips to show the spatial variation of these parameters and the slip. These plots indicate that offset and compaction are likely to be most important factors for predicted slip, and fault dip, azimuth and reservoir thickness do not appear to have good correlation with FE slip magnitude.

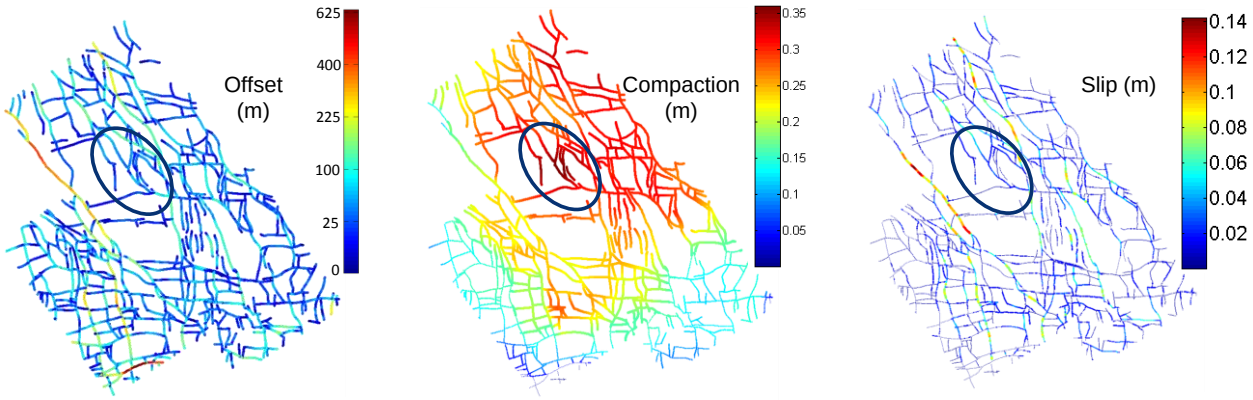

Fig. 3.10. Plots of fault offset, compaction and FE slip magnitude; the highlighted area has high compaction but low offsets and low resulting slip, which indicates that offset is likely to be most important factor for predicted slip.

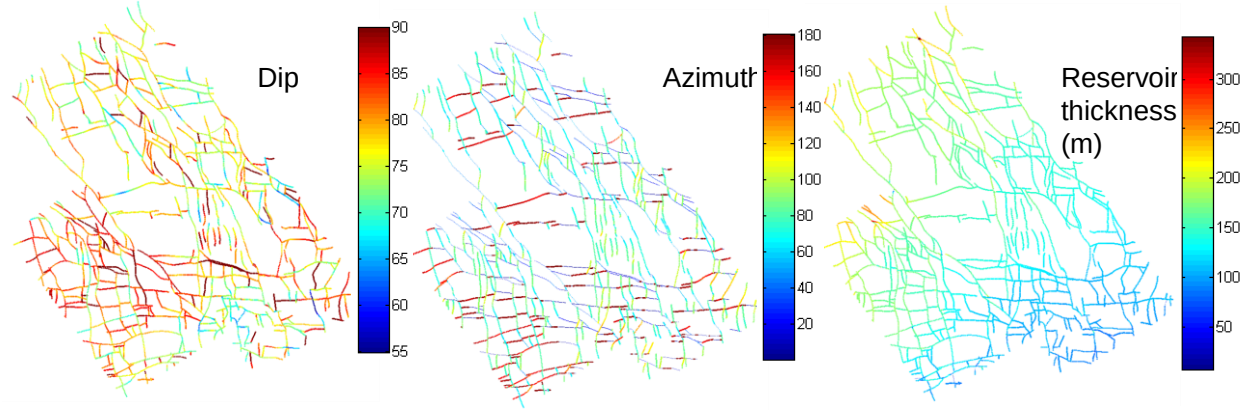

Fig. 3.11. Plots of fault dip, azimuth and reservoir thickness; these parameters do not appear to correlate well with FE slip magnitude shown in Figure 3.10.

In order to better understand the effect of these parameters, statistical regression analysis was conducted to fit the FE slip as a function of the following main parameters: offset, compaction, reservoir thickness, fault dip and azimuth; second order terms of these parameters and first order interaction terms were also included. The resulting model fit and regression equation are as follows:

Model Summary

S	R-sq	R-sq(adj)	R-sq(pred)
11.1261	60.81%	60.76%	60.64%

Regression Equation

```
MaxSlip (mm) = 65.6 - 1.936 Dip + 0.0301 Azimuth - 0.0329 ResThk + 0.5624 Offset
 + 252.4 Compaction + 0.01322 Dip*Dip - 0.000367 Azimuth*Azimuth - 0.000586 ResThk*ResThk
 - 0.000006 Offset*Offset - 272.0 Compaction*Compaction + 0.000642 Dip*Azimuth
```

```
 + 0.001513 Dip*ResThk - 0.005889 Dip*Offset - 3.080 Dip*Compaction
 - 0.000075 Azimuth*ResThk - 0.000243 Azimuth*Offset - 0.0068 Azimuth*Compaction
 - 0.001042 ResThk*Offset + 0.5503 ResThk*Compaction + 1.6022 Offset*Compaction
```

Analysis of Variance (ANOVA) can be used to identify parameters that are not significant.

Analysis of Variance (ANOVA)

Source	DF	Adj SS	Adj MS	F-Value	**P-Value**
Regression	20	2845179	142259	1149.19	0.000
Dip	1	5013	5013	40.50	0.000
Azimuth	1	146	146	1.18	**0.277**
ResThk	1	43	43	0.35	**0.555**
Offset	1	35963	35963	290.52	0.000
Compaction	1	14319	14319	115.67	0.000
Dip*Dip	1	6036	6036	48.76	0.000
Azimuth*Azimuth	1	15245	15245	123.15	0.000
ResThk*ResThk	1	6295	6295	50.85	0.000
Offset*Offset	1	24	24	0.19	**0.660**
Compaction*Compaction	1	22045	22045	178.08	0.000
Dip*Azimuth	1	525	525	4.24	0.040
Dip*ResThk	1	797	797	6.44	0.011
Dip*Offset	1	27155	27155	219.36	0.000
Dip*Compaction	1	17067	17067	137.87	0.000
Azimuth*ResThk	1	157	157	1.27	**0.260**
Azimuth*Offset	1	3497	3497	28.25	0.000
Azimuth*Compaction	1	6	6	0.05	**0.820**
ResThk*Offset	1	32548	32548	262.92	0.000
ResThk*Compaction	1	10158	10158	82.06	0.000
Offset*Compaction	1	226749	226749	1831.71	0.000
Error	14811	1833470	124		
Total	14831	4678649			

The parameters with P-values greater than ~ 0.05, highlighted in red above, do not have significant effect on the slip in FE models. Note that among the main parameters, azimuth and reservoir thickness are not significant factors for FE model slip.

The slip magnitudes vs. the main parameter plots, with effect of all other parameters statistically removed, are shown in Figure 3.12. Note that slip is most sensitive to fault offset.

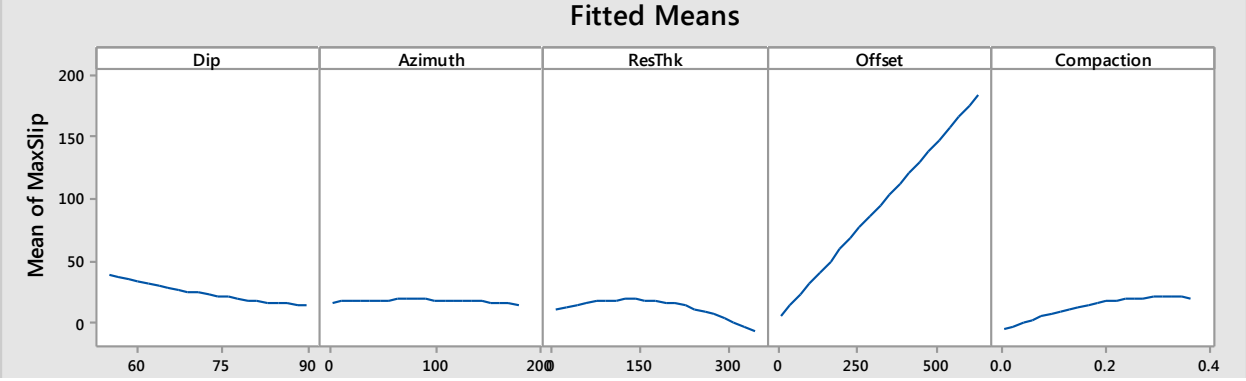

Fig. 3.12. Slip magnitude (mm) vs. main parameters; effect of other parameters statistically removed

The plots of slip vs. the interaction terms are shown in Figure 3.13. These plots are similar to above main parameter plots, but interaction with one parameter is retained and only the effect of remaining parameters is removed. Each plot show two lines, blue and dashed-red, corresponding to extreme values of the interaction parameter. Higher differences between these two lines are indicative of significance of the corresponding interaction term. These plots indicate that interaction terms of offset with other parameters are significant.

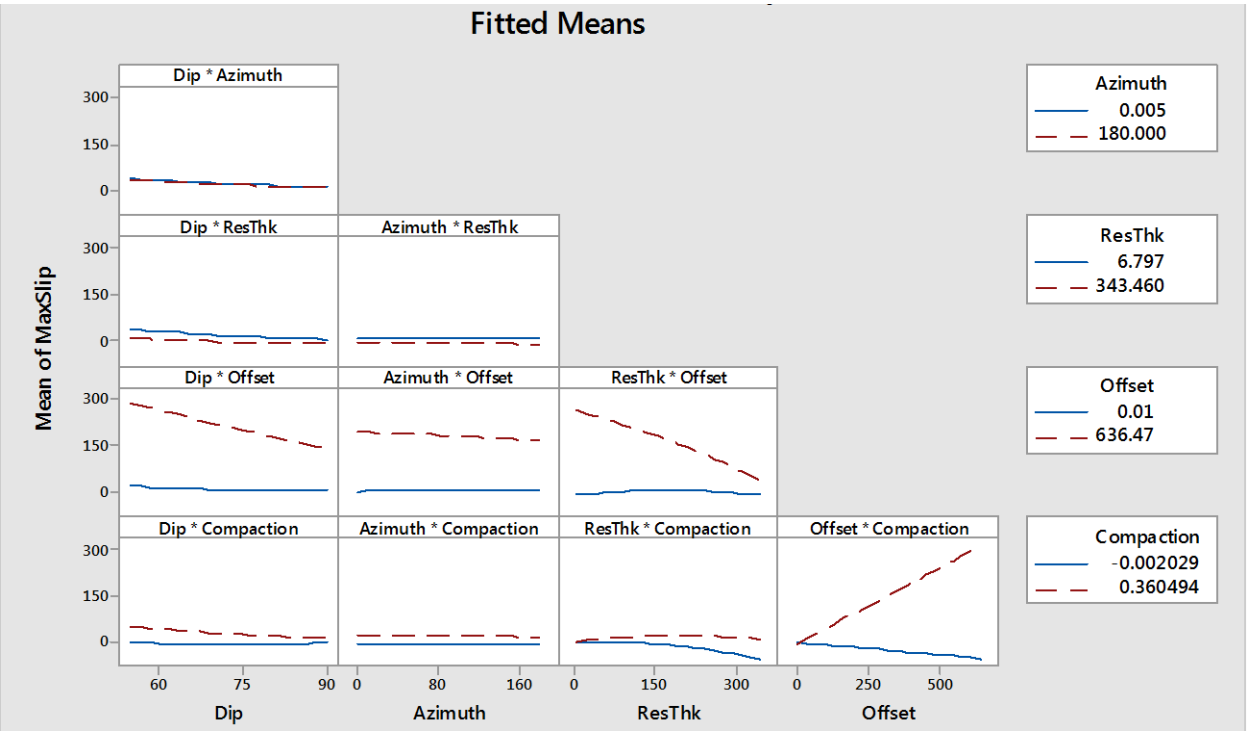

Fig. 3.13. Slip magnitude (mm) vs. first order interaction terms

3.3. Fault profiles at selected fault locations

Six different fault locations included in the sub-models were picked to investigate slips predicted by FE models in more detail. The selection was done to cover multiple fault characteristics such as offset, dip, strike, compaction and reservoir thickness. Figure 3.14 shows the locations of the selected faults and their characteristics. For example, fault B51 has one of the largest offset and compaction; M1 is similar to B51 but has different dip and strike; F213 has the smallest offset but the largest compaction and F122 has the largest offset but the smallest compaction.

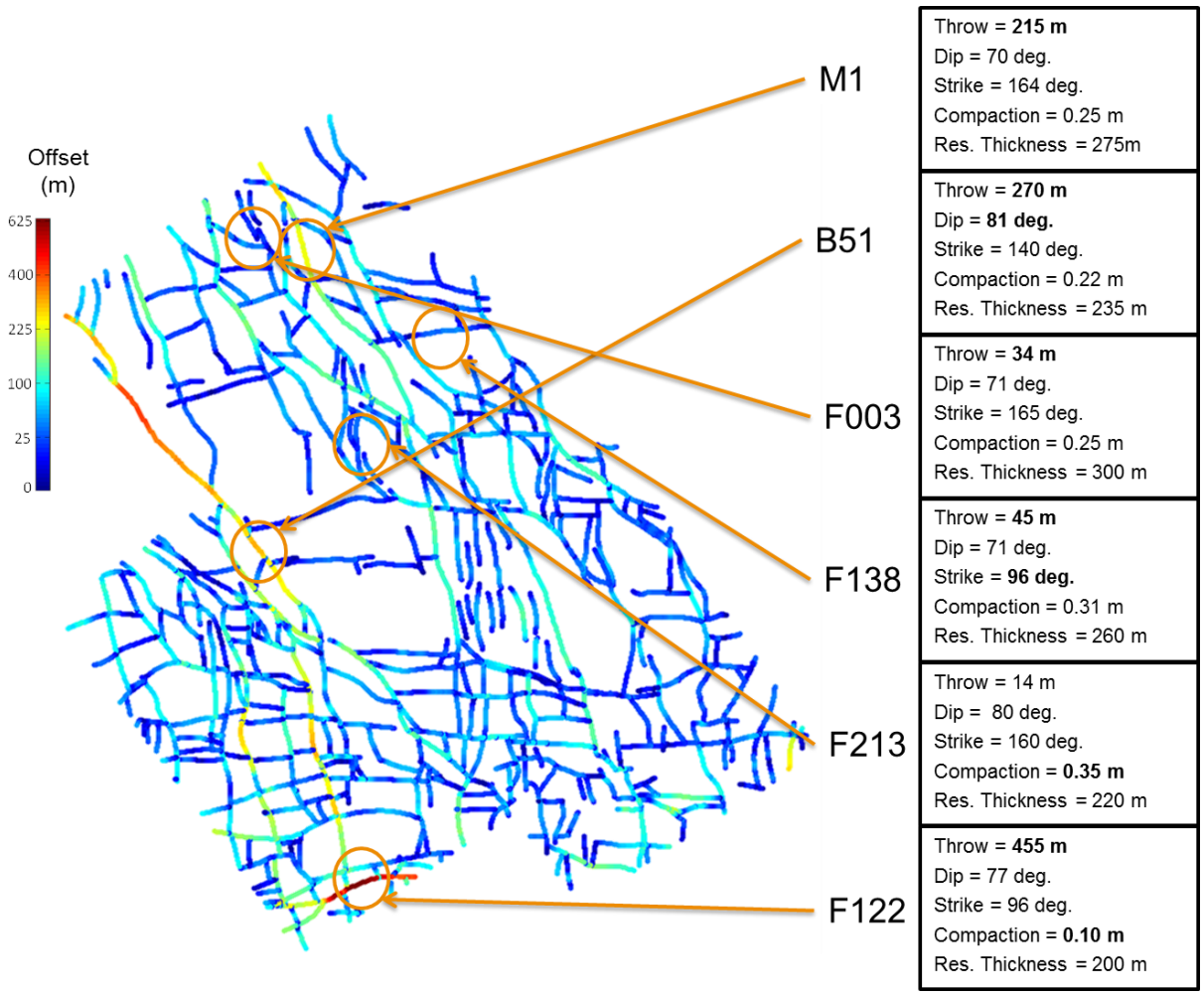

Fig. 3.14. Six fault locations selected for detailed investigation and their characteristics.

M1 Fault has one of the largest offsets, compaction and reservoir thickness. Also, it has a favorable fault dip and strike for developing slip. Figure 3.15 shows fault slip and pore pressure for fault M1 at one location along a vertical path for different years. Note that the pore pressure chart has positive and negative values – this is done to clearly depict pressure changes on the two sides of the fault. Actual depletion values on both sides are positive, but those on one side are plotted on negative side to facilitate visualization of pressure change on both sides of the fault. Additionally, horizontal dashed lines are included in the chart to indicate the boundaries of different rock layers.

In a similar manner, Figure 3.16 shows shear, normal pressure and mobilized friction (μ_{mob}) for fault M1 corresponding to different years. Note that there is an increase in shear and normal pressure due to depletion and μ_{mob} is equal to 0.48 at locations where the fault is slipping, as expected. Also note that the length of the slip area along this path-line increases with increasing depletion with time.

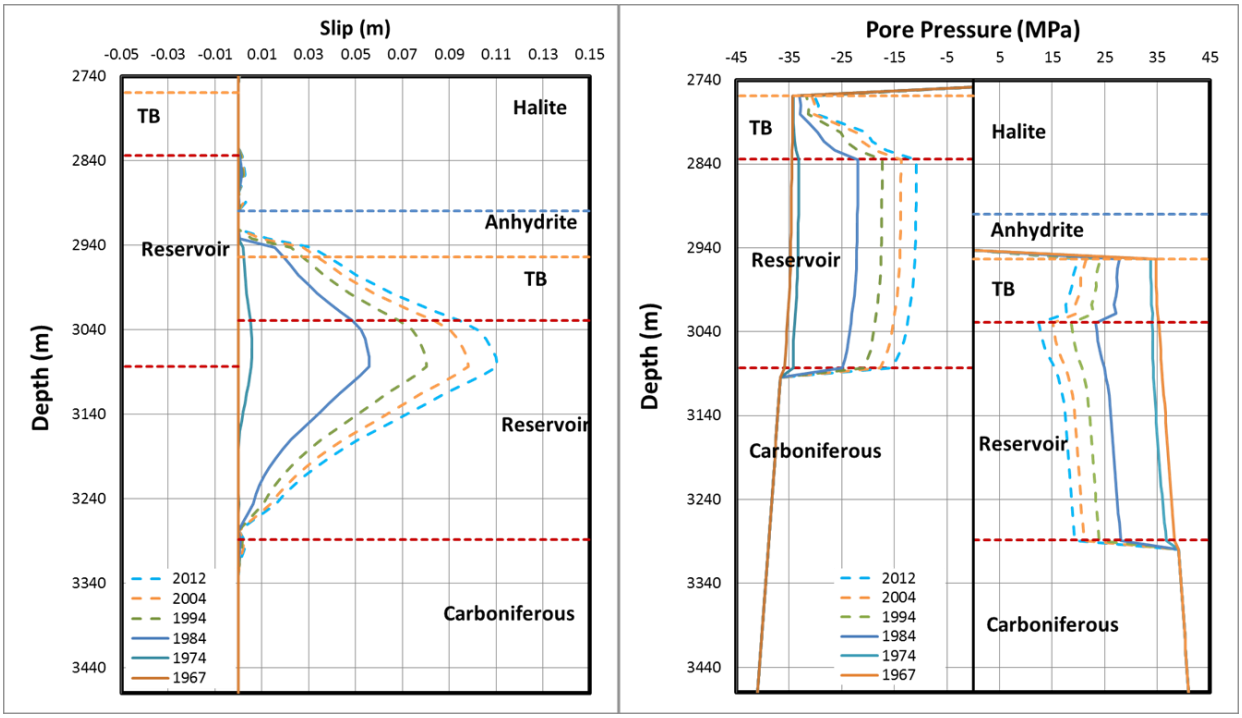

Fig. 3.15. M1 fault; fault slip and pore pressure along a vertical path.

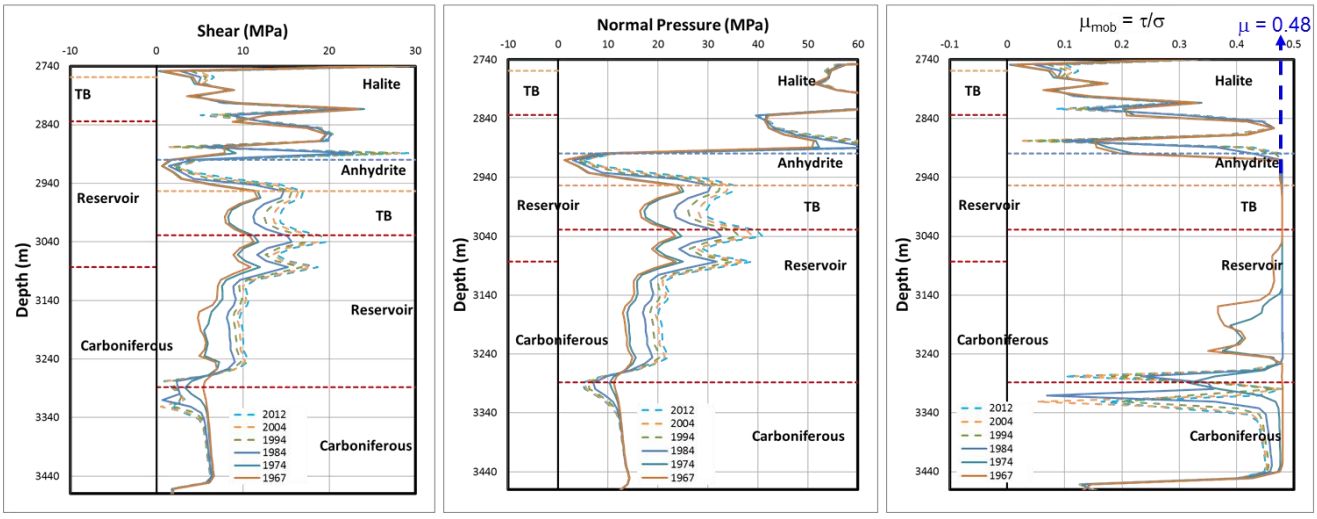

Fig. 3.16. M1 fault; shear, normal pressure and mobilized friction μ_{mob} along a vertical path.

A similar fault with larger offset, less compaction but larger reservoir thickness is B51. Its orientation is not as favorable for slip as M1, since its dip and strike are 81 degrees and 140 degrees, respectively. Figures 3.17 and 3.18 show fault slip, pore pressure, shear, normal pressure and mobilized friction for fault B51 corresponding to different years.

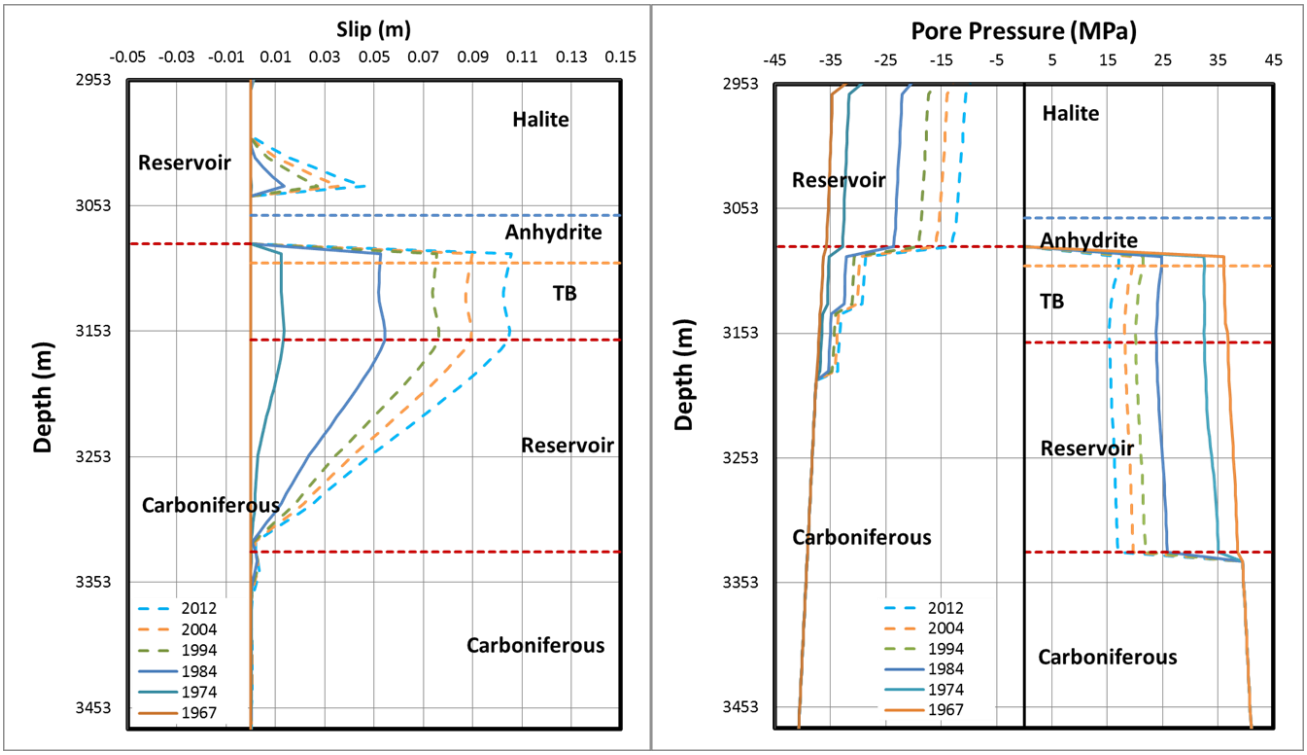

Fig. 3.17. B51 fault; fault slip and pore pressure.

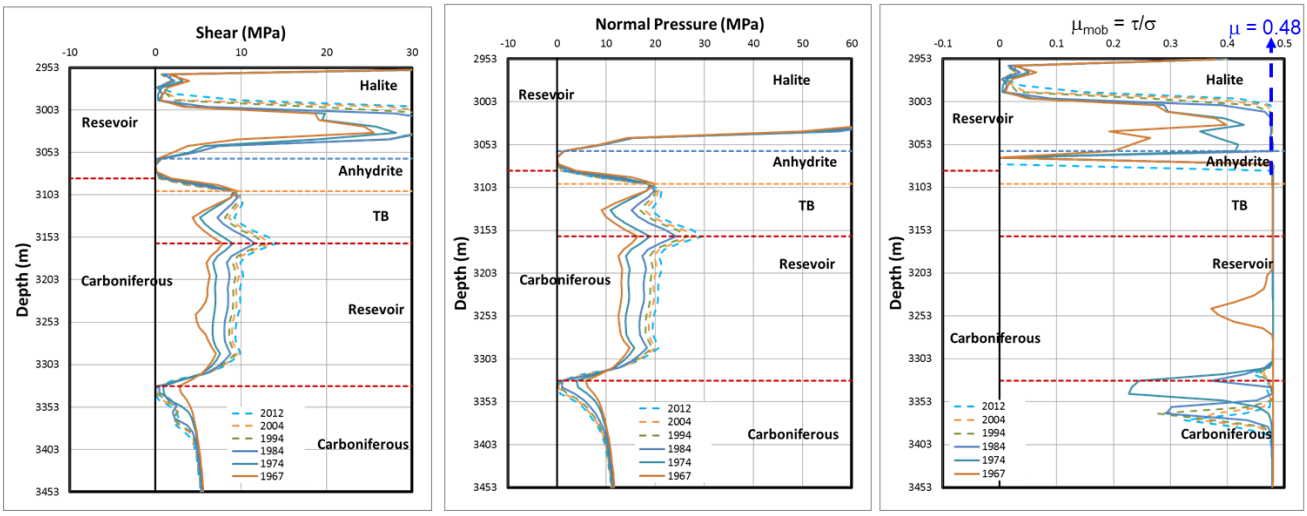

Fig. 3.18. B51 fault; shear, normal pressure and mobilized friction μ_{mob}.

Similar to fault M1, B51 has significant amount of slip. Even though some characteristics are different the main contributor for slip is the offset, which is large for both of these faults.

The following 3 faults: F003, F138 and F213, have very small offset but similar compaction and reservoir thickness as those for M1 and B51. The amount of depletion on these faults is comparable to the

previous faults, but almost no slip is observed, except at the interface between the reservoir and other type of rock, as shown in Figures 3.19, 3.20 and 3.21.

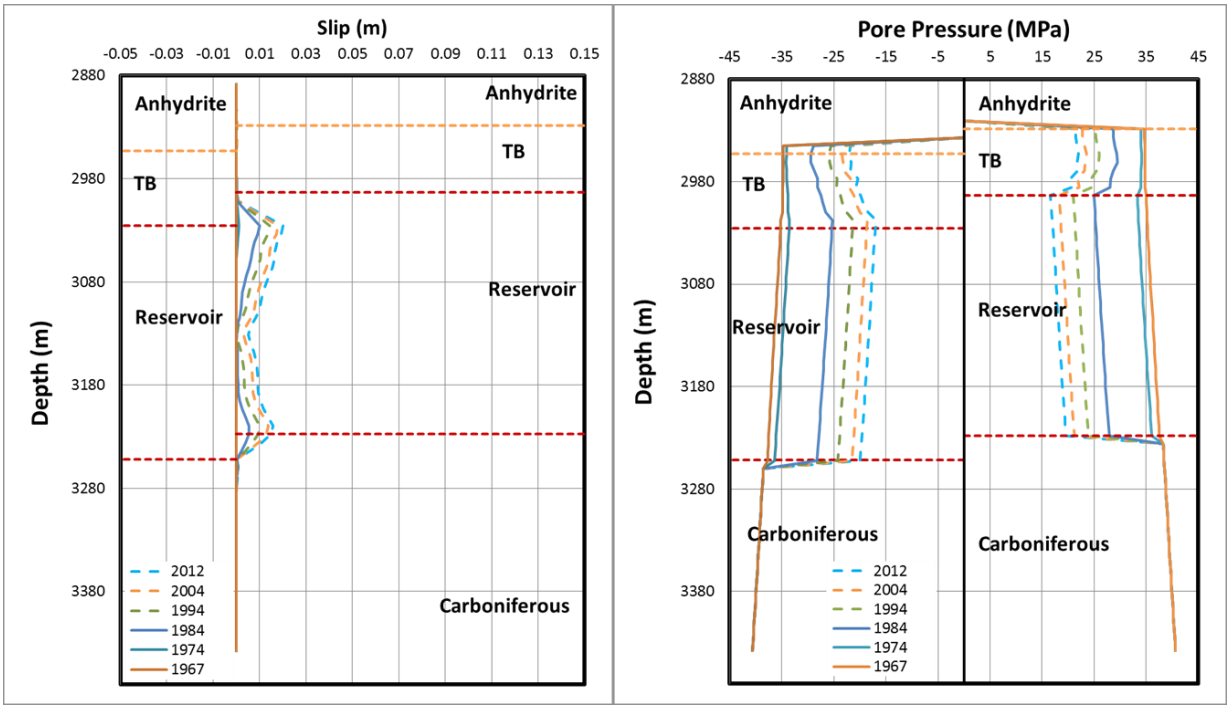

Fig. 3.19. F003 fault; fault slip and pore pressure.

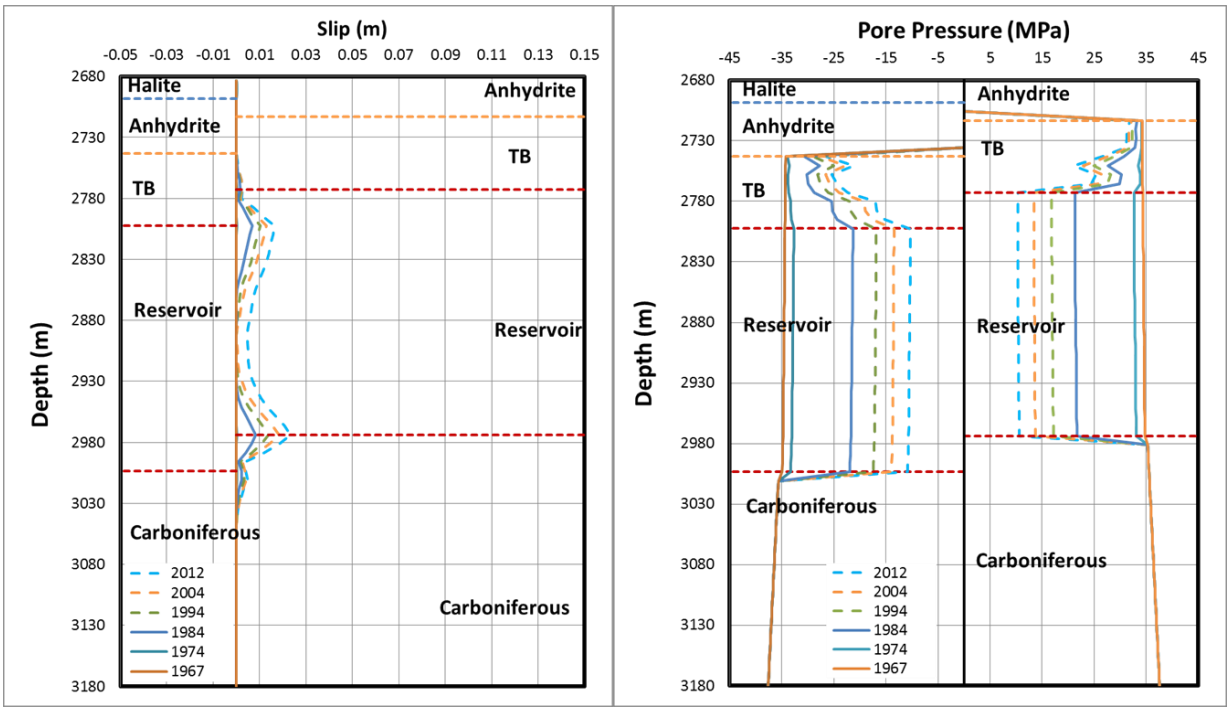

Fig. 3.20. F138 fault; fault slip and pore pressure.

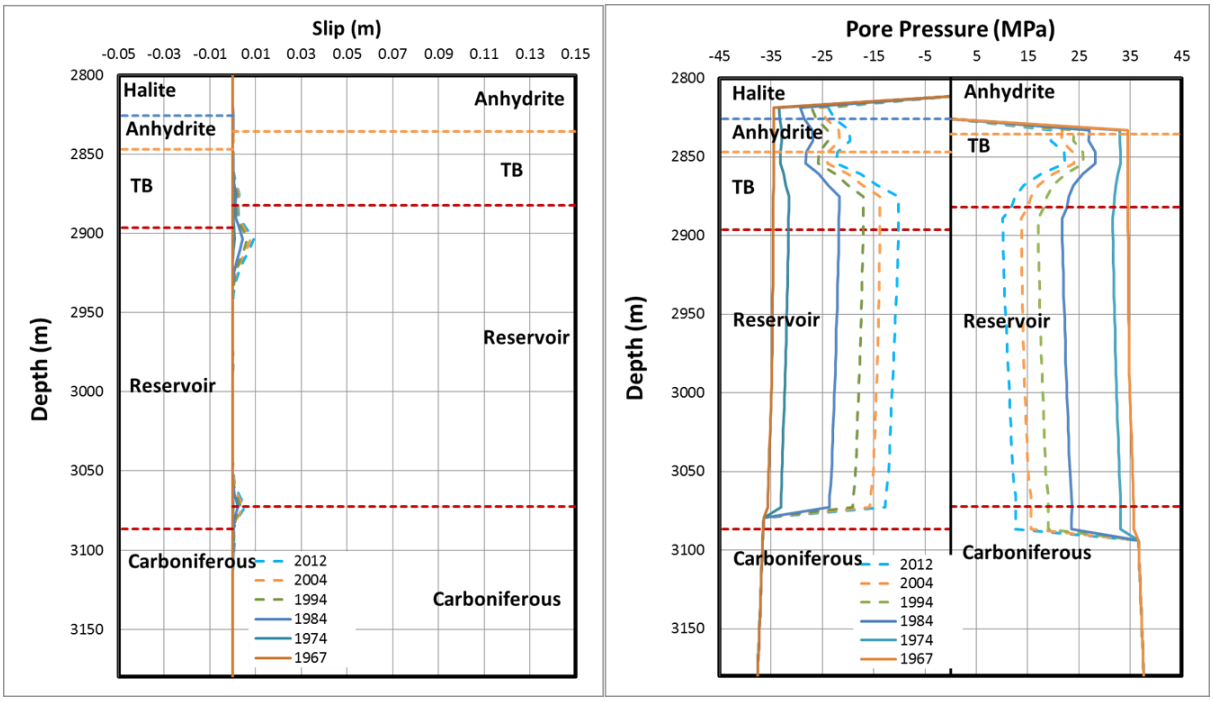

Fig. 3.21. F213 fault; fault slip and pore pressure.

Finally, Fault 122 has the largest offset of ~455m but very little compaction, only 10 cm. Because of its large offset a lot of slip was expected, but this fault is at the edge of the Groningen field and it has depletion on only one side. In turn, no slip is observed in this fault. Figure 3.22 shows fault slip and pore pressure for this fault.

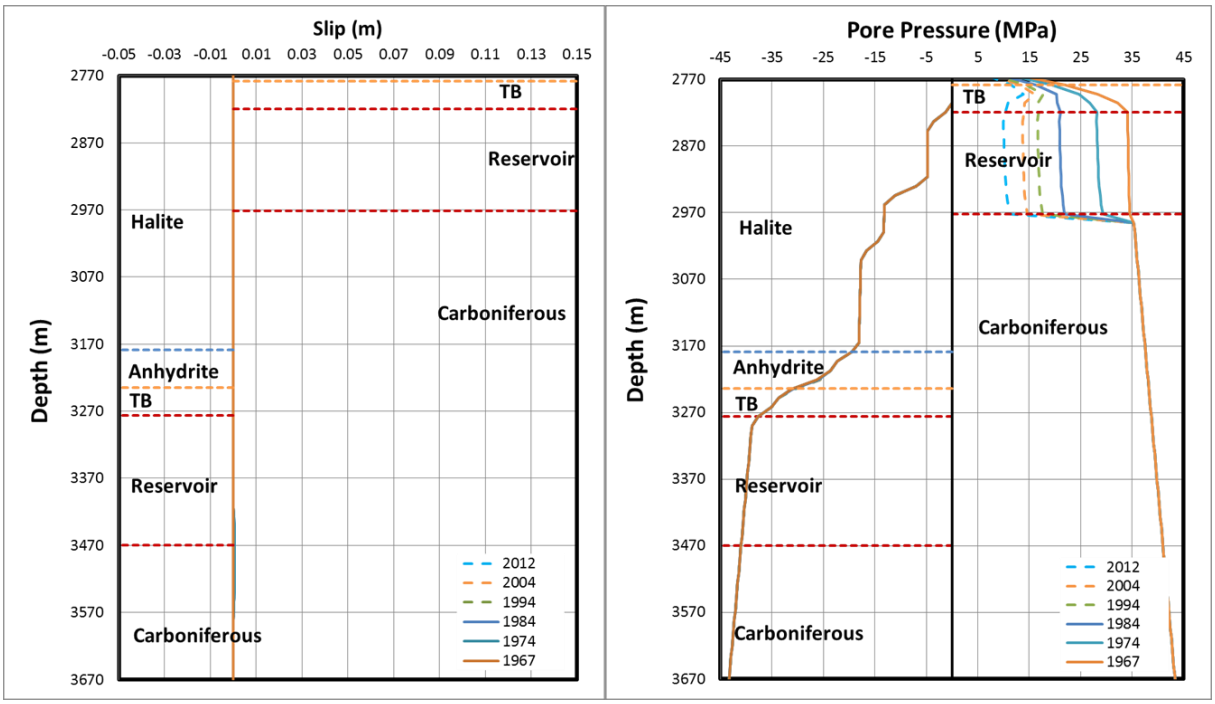

Fig. 3.22. F213 fault; fault slip and pore pressure.

In summary, it has been found that if a fault has been depleted on both sides, the amount of slip is approximately proportional to the amount of offset. It is also important to mention that for faults M1 and B51, where the most significant amount of slip has been found, the fault movement is confined to the reservoir layer. Slip is arrested once carboniferous is in contact with carboniferous.

3.4. Fault contribution to seismic moment

As time progresses and the reservoir is depleted, faults start moving and the cumulative seismic moment increases. Note that not all faults get reactivated at the same time, but new faults start contributing to the total moment as depletion increases. The geomechanical model results show that by 1981, 10 faults contribute 70% of the total moment; and by 2014, 20 faults (see Figure 3.23).

The major contributors to seismic moment are faults B51, M1, M2 and M18. Figure 3.24 shows the contribution of 60 faults out of 255 contact pairs for sub-model-1 (excluding a few small contact pairs tied due to convergence issues) for the year 2014. These 60 faults contribute 85% of the total moment in 2014.

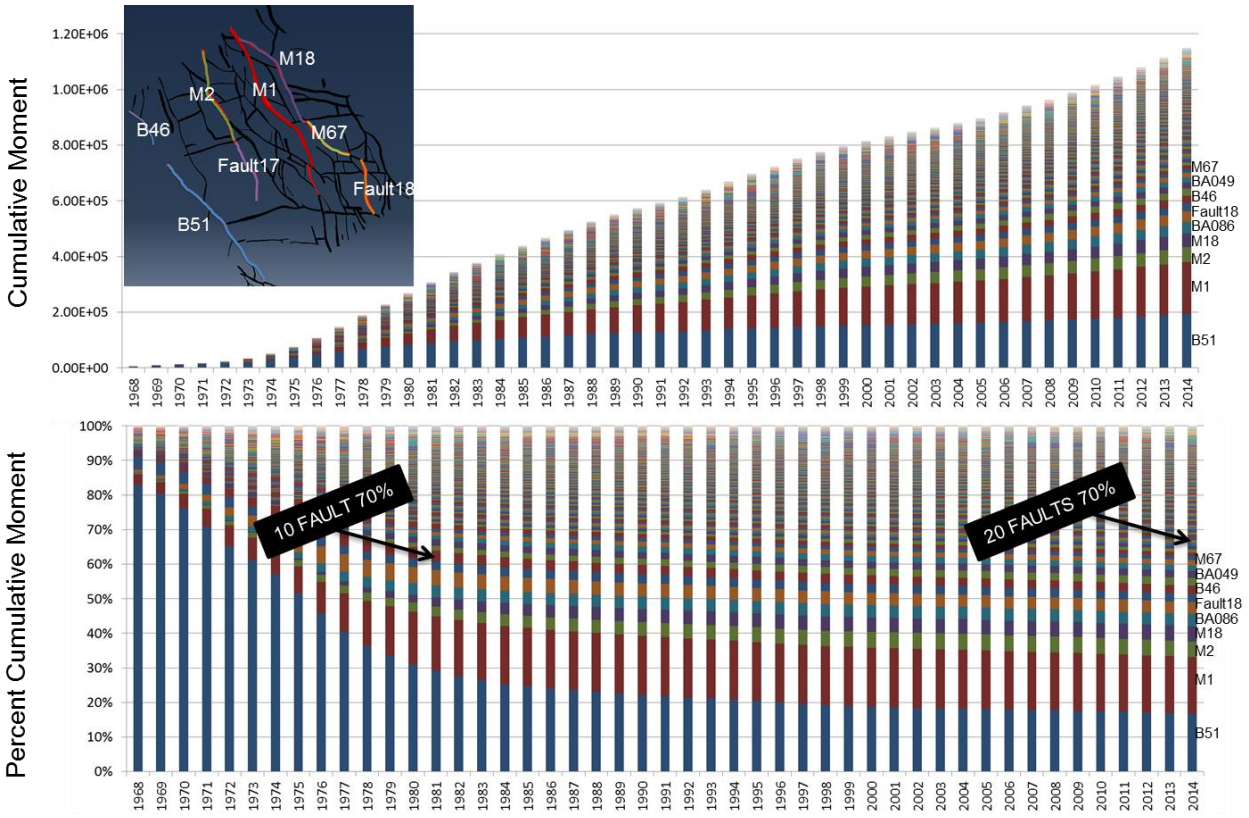

Fig. 3.23. Fault contribution to seismic moment from 1968 to 2014.

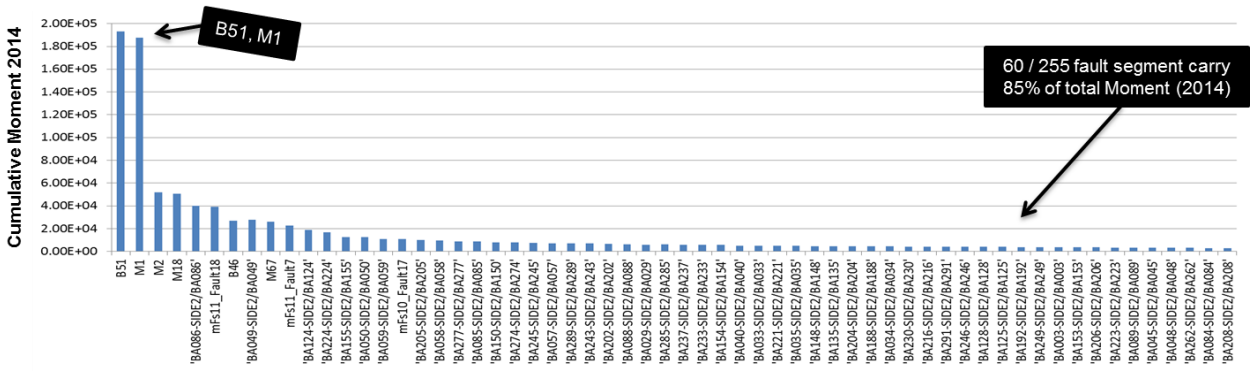

Fig. 3.24. Individual fault contribution to cumulative seismic moment, year 2014.

4. Model Results

This chapter presents results from the FE analyses: the comparison of production scenarios based on dissipated energy, the effect of seasonal production and analysis of stresses near Groningen city. Additionally, slip values and contact force data predicted by these models at each FE node location for each fault surface were output and used in the seismological models for hazard and risk analysis.

4.1. Evaluation of production scenarios

The plots of dissipated energy vs. time for base case no-curtailment production scenario, 2013-G1C1D1, the three early 2015 scenarios with 20, 33, 39.4 Bcm caps, and four new scenarios with 21, 27 and 33 Bcm caps are included in Figure 4.1. Version 33Bcm_LOPPZ of the 33 Bcm cap case assumes that production from Loppersum area may be increased after completion of building strengthening program.

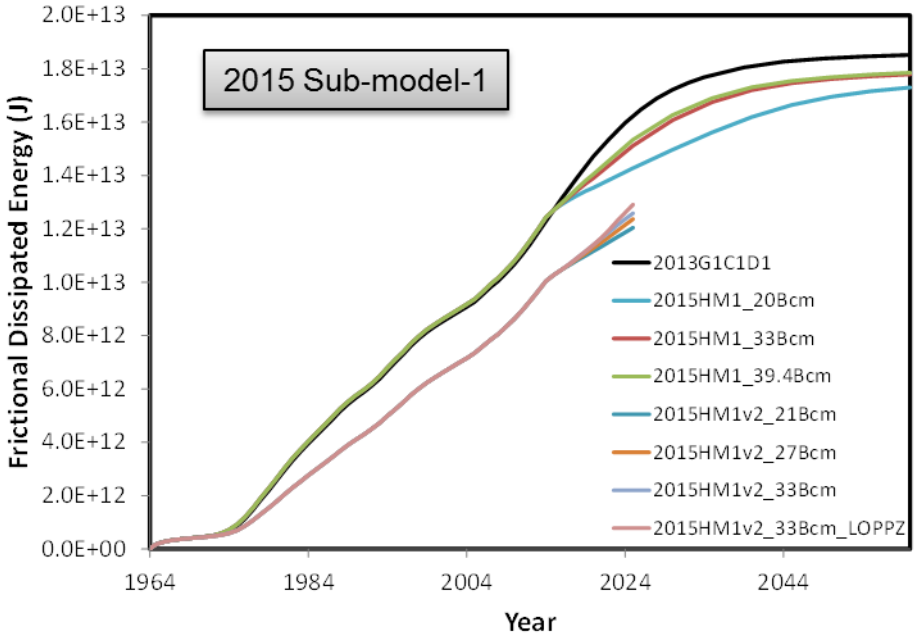

Fig. 4.1. Comparison of dissipated energy vs. time for various production scenarios for sub-model-1; base case friction coefficient μ=0.48.

Note that the 2015 production history match v2 is different from previous history matches; it combined two previous matches for best aquifer pressure and best subsidence; since the aquifer is in the northwest corner of the field, this leads to larger differences for sub-models-1 and -2, but will have small effect on sub-model-3. Similar plots for sub-models-2 and -3 are included in Figures 4.2. and 4.3.

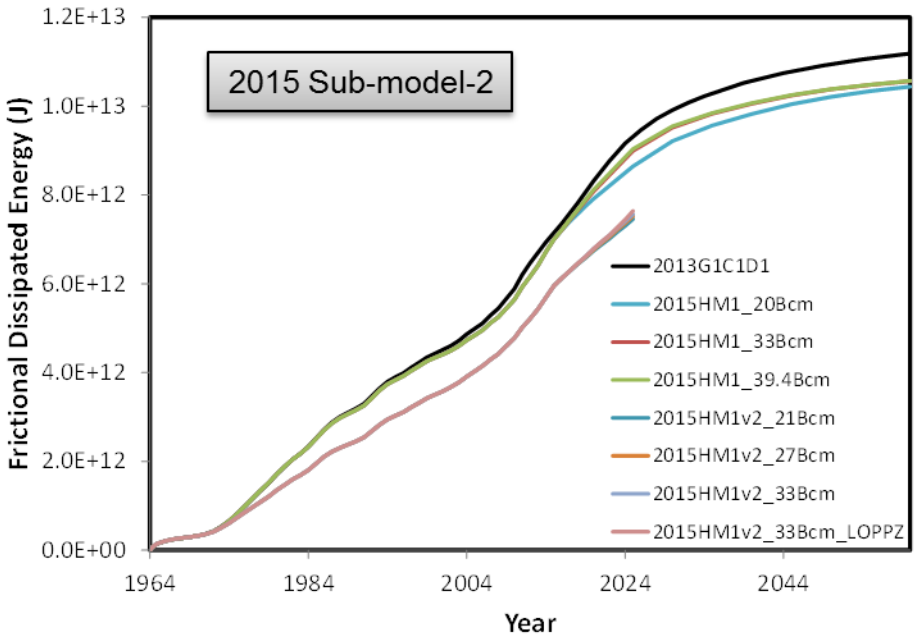

Fig. 4.2. Comparison of dissipated energy vs. time for various production scenarios for sub-model-2; base case friction coefficient μ=0.48.

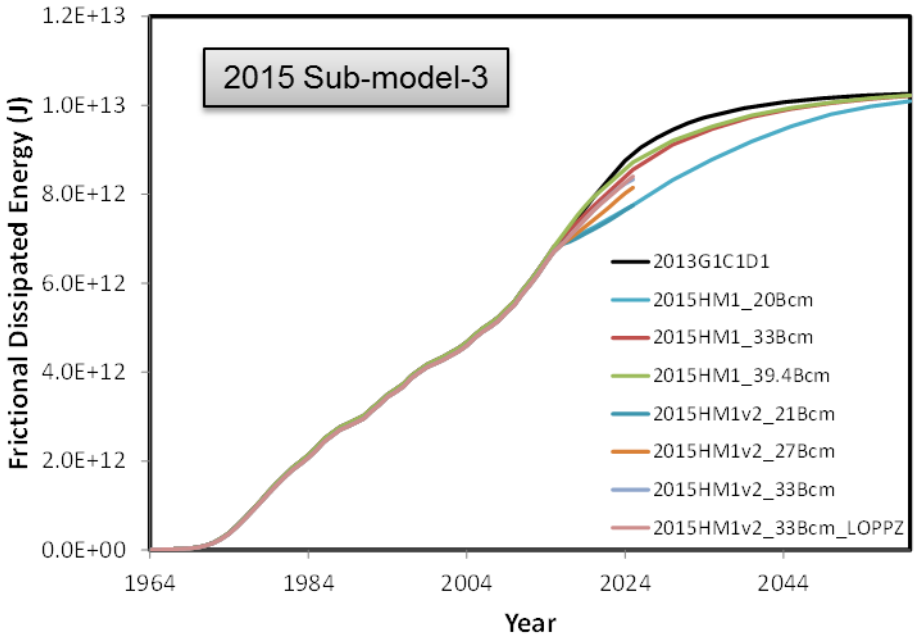

Fig. 4.3. Comparison of dissipated energy vs. time for various production scenarios for sub-model-3; base case friction coefficient μ=0.48.

The plots of dissipated energy per 5 year period for sub-models-1 and -2 are included in Figure 4.4. Note that the energy per 5 year period initially increases around 1980-1990, and then falls around ~2005, increases again around 2010, before decreasing due to production curtailment. This trend is qualitatively similar to overall field production volumes. This is likely due to the effect of offset on slip discussed in chapter 3. Higher production will lead to higher compaction and correspondingly higher slip at faults with offset, which will result in higher dissipated energy.

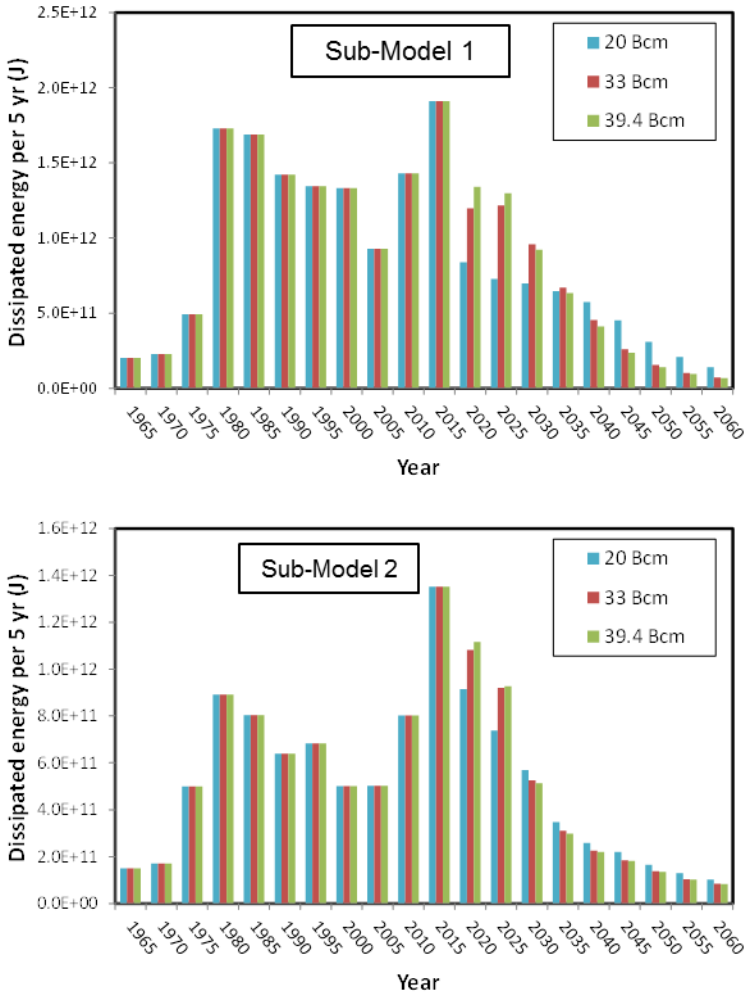

Fig. 4.4. Dissipated energy per 5 year period for sub-model-1 and -2; friction coefficient μ=0.48.

The plots of dissipated energy vs. the cumulative volume assigned to the sub-model region (based on well locations) are presented in Figure 4.5. Note that allocation of cumulative volumes is approximate due to limited availability of this data, and these results are approximate.

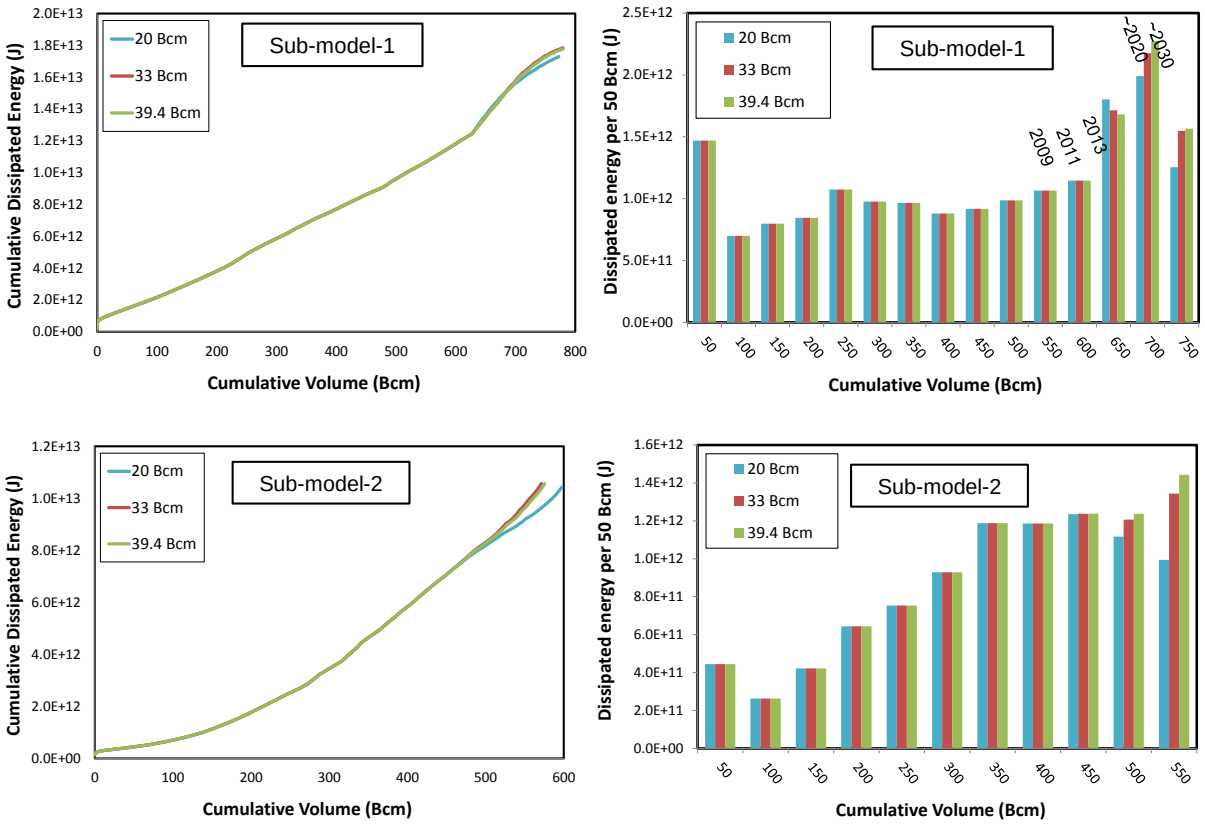

Fig. 4.5. Cumulative dissipated energy and the dissipated energy per 50 Bcm production vs. cumulative volumes allocated to each sub-model region; friction coefficient μ=0.48.

Note that changes in trends of the dissipated energy per 50 Bcm vs. the cumulative volume plot for sub-model-1 (top right chart above) around year 2014 are due to reduction in production from the Loppersum region contained in sub-model-1 from 2014. During 2009-2013 it takes ~2 yrs to produce 100 Bcm from sub-model-1, whereas during 2014-2030 it takes 7 to 10 yrs to produce 100 Bcm due to this regional curtailment. The dissipated energy is not directly proportional to these sub-model-1 production volumes since it can be affected by the overall stress state in the field.

4.2. Effect of seasonal production

Pore pressure changes due to daily production rate fluctuations are expected to be limited to a small lateral extent; they are not expected to significantly impact the stress state on faults and seismicity. Such small changes cannot be captured in the current geomechanical models to mesh element size. However, the oscillations on longer, month-to-month time scales due to seasonal production are felt throughout the field, and can be captured by the geomechanics model. Current geomechanical analyses utilize one year time increments during the production history (up to 2014), and 1-5 year increments for production forecast periods. To analyze the effect of variable production rates within a

year, a sensitivity analysis was conducted with one-month time increments for the year 2012 pressure data. Pore pressure changes from the reservoir simulator are imposed on a monthly basis in the sensitivity analysis and compared with corresponding results with one time increment for the entire year of 2012.

Figure 4.6 shows the dissipated energy for two cases with one-month increments and one-year increment. For both sub-models, the dissipated energy for the one-month increment case shows some non-linearity vs. time and differs from the case with one-year increment. However, note that the energies at the end of the year are nearly identical for both cases. Figure 4.6 also shows the incremental energy per month from the two cases; for the case with one-year increment, the change in energy over the year is equally divided for the 12 months. For the monthly increment case, there is more dissipated energy in the months with more production volumes.

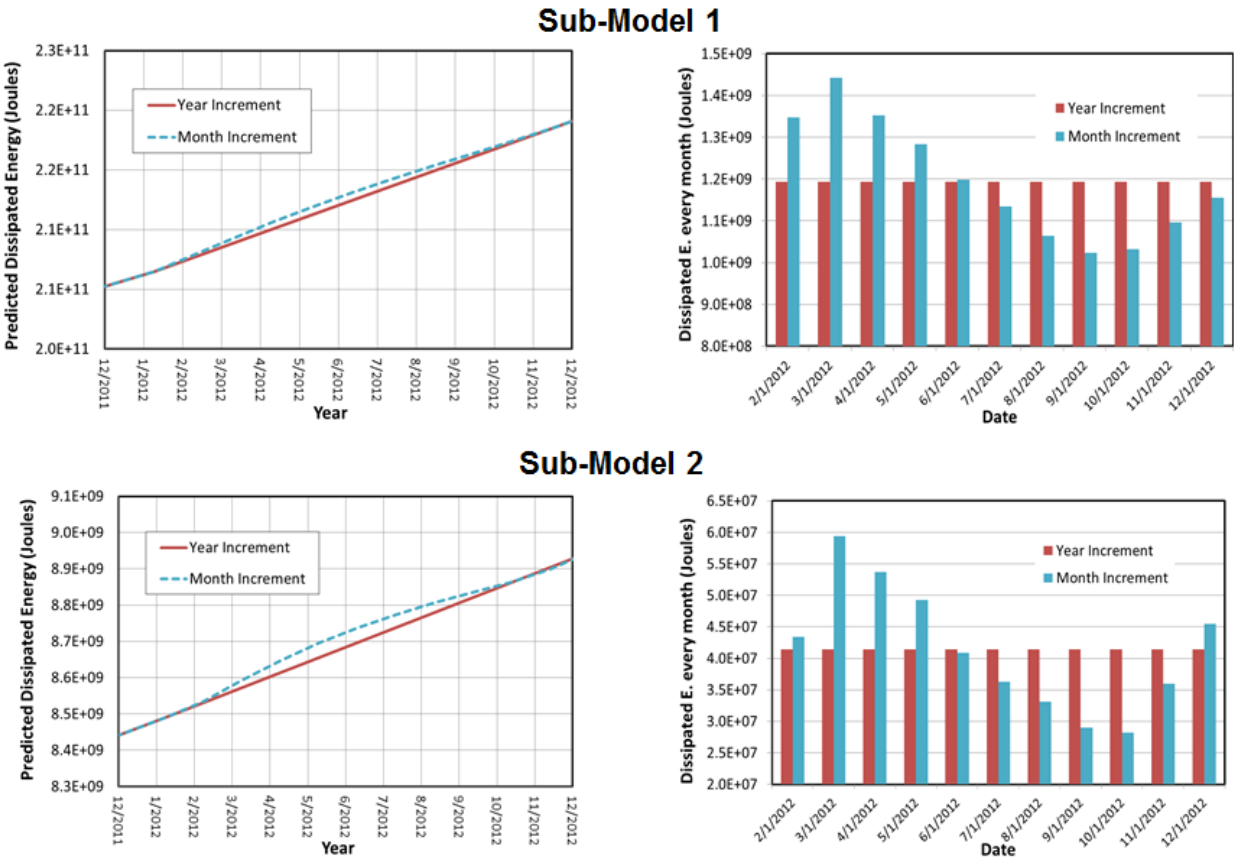

Figure 4.6: Comparison of dissipated energy for year 2012 for analyses with one-month and one-year time increments (2013 sub-models-1 and -2 are used for these analyses).

This result, with same dissipated energies at the end of the year for both cases, is expected given the physics that are captured in the quasi-static geomechanics model, and validates the numerical method being invariant of the time increment chosen for the simulation. The reservoir rocks are modeled as a linear elastic material with Drucker-Prager plasticity model, and no hardening. The stresses do not result in plastic deformation in most of the model domain, so the material response is linear elastic and

there is no rate dependence. The only rate dependence in the geomechanical model is the behavior of the salt that overlies the reservoir. The salt is modeled using creep material model provided by NAM, but the effect of this creep on the one-year time scale is negligible. The constitutive relationship that governs the fault sliding (Coulomb frictional sliding with no cohesion) also does not include rate dependence. Frictional sliding is a history dependent process so areas that experience loading and unloading can show an effect, but based on these results, this effect is negligible.

These analyses were conducted using the 2013 sub-models. However, these trends are not expected to change for the 2015 models with more faults and offsets included.

5. Sensitivity Studies

5.1. Friction coefficient sensitivity study

Friction coefficient of the faults cannot be measured accurately in field and/or lab tests, and hence this parameter introduces significant uncertainty in model inputs. Moreover, this parameter had large effect on predicted fault slip and dissipated energy in 2013 models. Hence, a sensitivity study with different friction coefficient values is conducted to understand its effect on the 2015 models with offsets.

The dissipated energy vs. time for various friction coefficient values for sub-model-1 is shown in Figure 5.1. The dissipated energy is normalized to two reference years in the two plots respectively, at the start of production in 1964, and year 1996 representing the first year with a complete earthquake catalog.

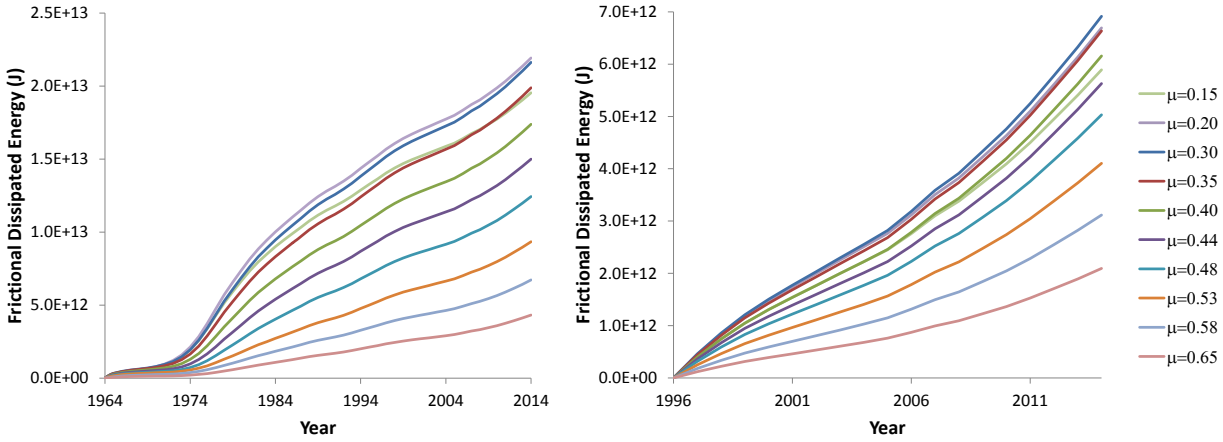

Fig. 5.1. Dissipated energy vs. time, normalized to 1964 and 1996 respectively, for sub-model-1.

Plot of the energy in 2014 vs. the friction coefficient values for sub-model-1 is included in Figure 5.2. Corresponding results from 2013 models are included for comparison. Note that dissipated energy in the 2015 models with faults is significantly less dependent on friction coefficient compared to that in 2013 model. The energy for μ=0.65 is only around 4-5x lower compared to that for μ=0.30 for 2015 model, whereas that ratio was over 200x for 2013 models. This behavior is due to high slip at offsets in 2015 models (see chapter 3), and the fact that this slip can develop even for higher coefficient of friction, whereas the 2013 models had much lower slip for higher coefficients friction due to absence of fault offsets. The maximum dissipated energy for both 2013 and 2015 models is for friction coefficient of approximately 0.20.

The contour plots of slip magnitudes for sub-model-1 for the base case friction coefficient μ=0.48, and for 0.30 and 0.65 are included in Figure 5.3.

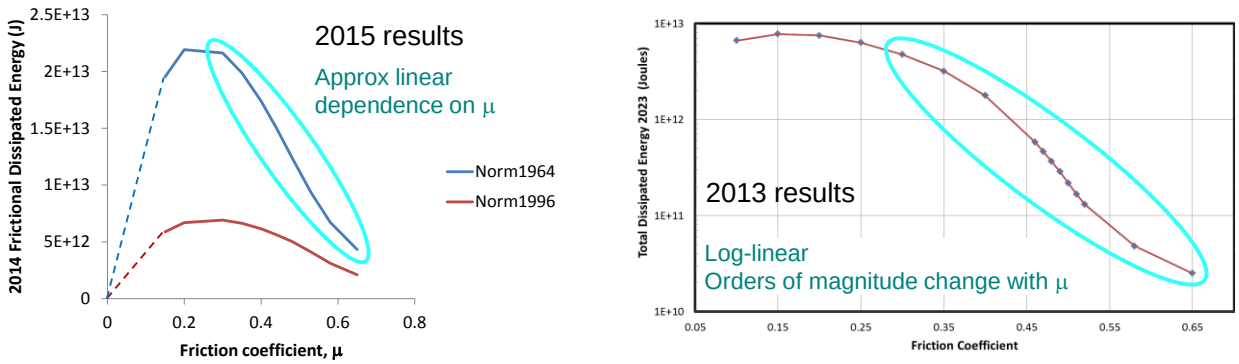

Fig. 5.2. Dissipated energy vs. friction coefficient for 2015 sub-model-1 and 2013 sub-model-1; note that analysis with friction coefficient of zero was not run, but energy for that case will be zero due to no contact shear stress.

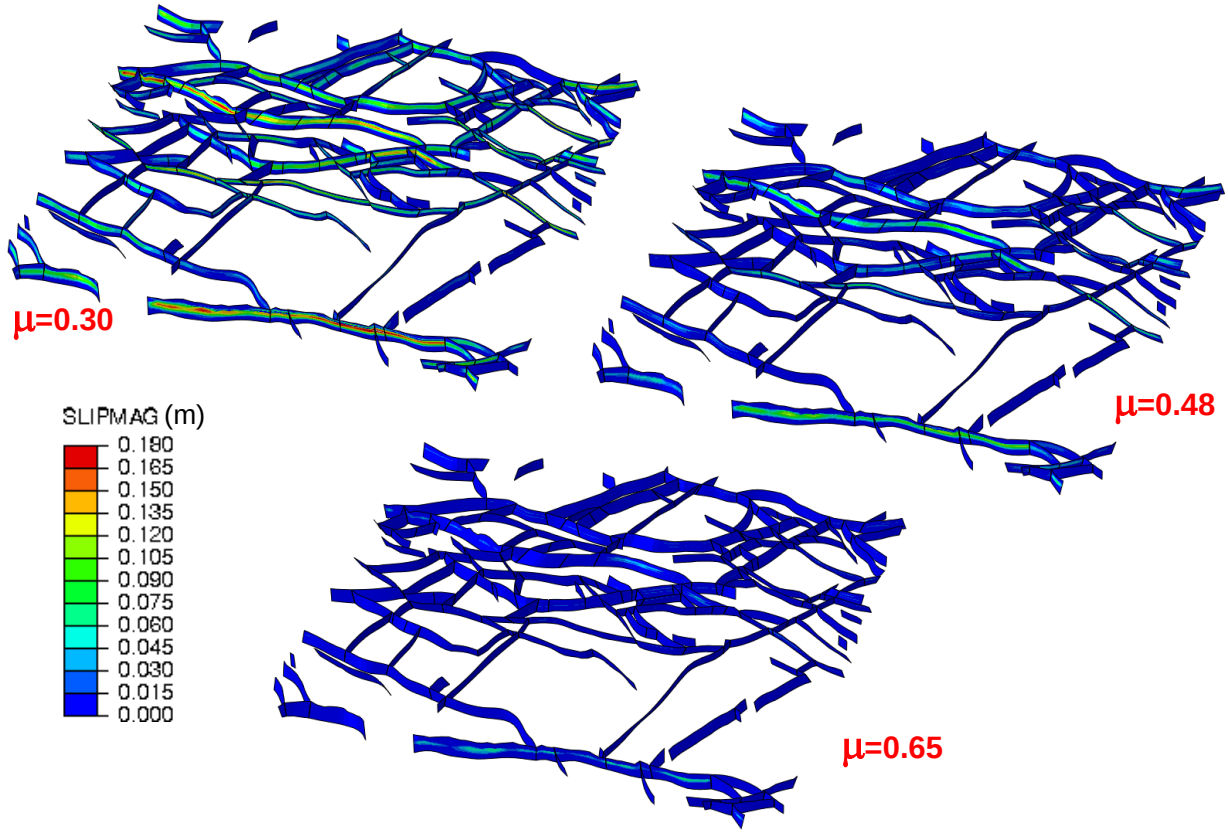

Fig. 5.3. Contour plots of slip magnitude for 2015 sub-model-1; μ=0.30, 0.48 and 0.65.

The trends for sub-model-2 and -3 are similar to those for sub-model-1. Dissipated energy vs. time plots for these models are shown in Figures 5.4 and 5.5 respectively. Similar to sub-model-1, results normalized to reference years 1964 and 1996 are included. Plots of dissipated energy vs. friction coefficient for these two models are included in Figure 5.6.

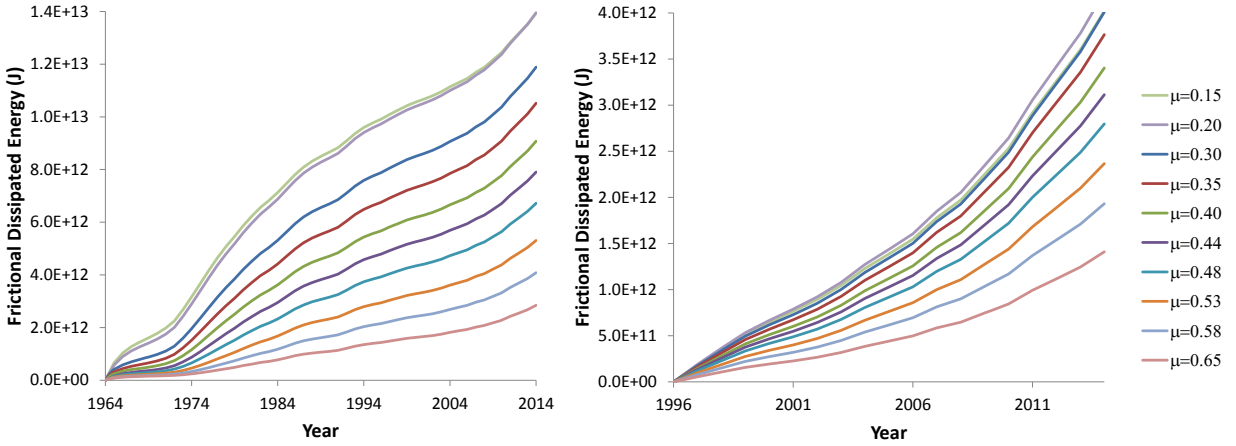

Fig. 5.4. Dissipated energy vs. time, normalized to 1964 and 1996 respectively, for sub-model-2.

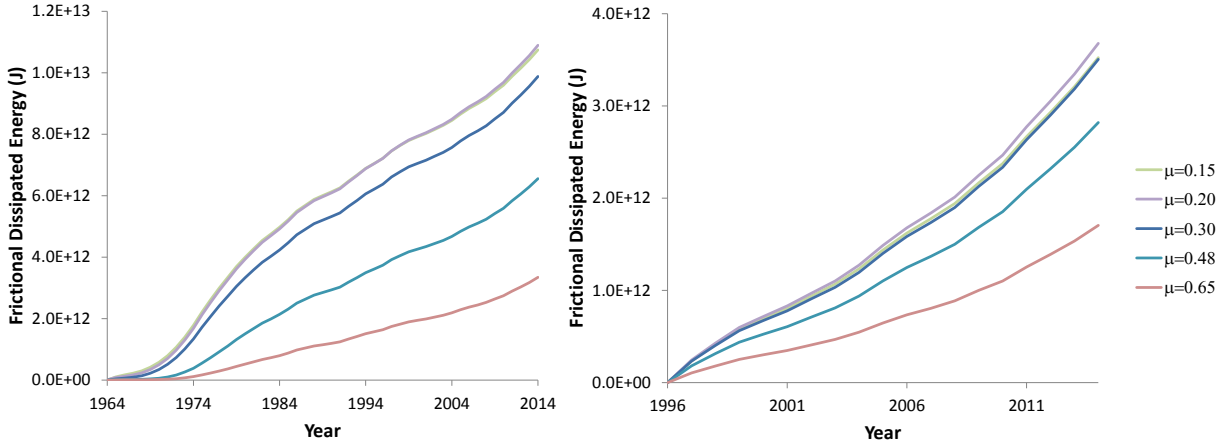

Fig. 5.5. Dissipated energy vs. time, normalized to 1964 and 1996 respectively, for sub-model-3.

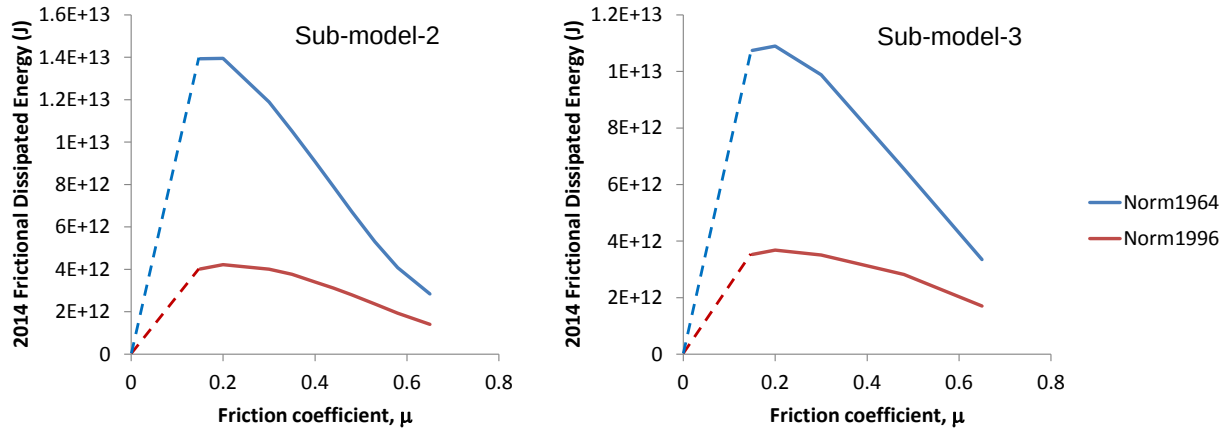

Fig. 5.6. Dissipated energy in 2014 normalized to 1964 and 1996 vs. friction coefficient for sub-model-2 and -3 respectively; note that analysis with friction coefficient of zero was not run, but energy for that case will be zero due to no contact shear stress.

As previously discussed, 2015 models are less sensitive to friction coefficient compared to 2013 models due to inclusion of offsets in 2015 models. The offsets for faults included in sub-model-3 are smaller on average compared to those in the other two sub-model regions. The effect of this is seen in the dependence of slip initiation on friction coefficient. Figure 5.7 shows the dissipated energy vs. time plots for the initial years of the field production, 1964 to 1975. The dissipated energy in sub-model-1 and -2 for all friction coefficients rises from the start of production due to immediate development of slip on faults with large offsets. However, a slightly more gradual increase in dissipated energy is seen in sub-model-3 for higher friction coefficients.

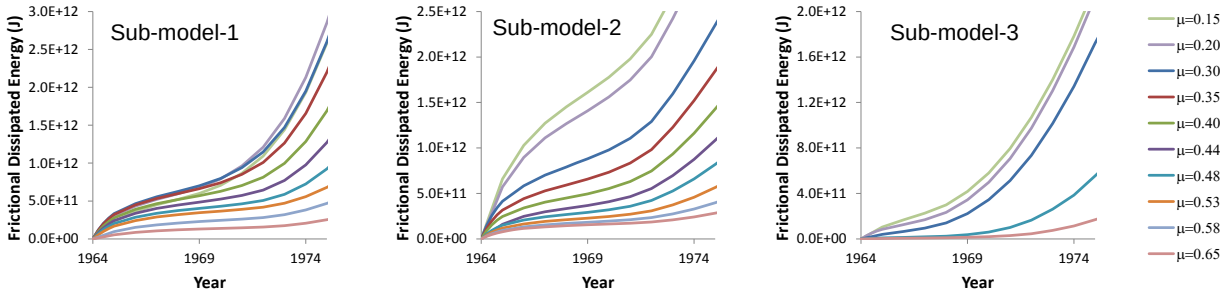

Fig. 5.7. Dissipated energy vs. time for initial years of field production, 1964-1975 for sub-model-1, -2 and -3 respectively; note the slightly later slip (or dissipated energy) initiation for higher coefficients for sub-model-3 that has on average lower fault offsets.

5.2. Initial stress sensitivity studies

A sensitivity analysis for the initial horizontal stresses is presented in this section. As done with the base case, after initialization, salt-creep steps are run to achieve an isotropic stress state in halite layers before starting the production history analysis.

The following gradients for stresses are used when increased by 10%:

- Vertical stress: 2.14 bar/10m (unchanged)
- Maximum horizontal stress: 1.88 bar/10m (increased 10% from base case value of 1.71)
- Minimum horizontal stress: 1.76 bar/10m (increased 10% from base case value of 1.60)

The following gradients for stresses are used when decreased by 10%:

- Vertical stress: 2.14 bar/10m (unchanged)
- Maximum horizontal stress: 1.53 bar/10m (decreased 10% from base case value of 1.71)
- Minimum horizontal stress: 1.44 bar/10m (decreased 10% from base case value of 1.60)

The predicted evolution of frictional dissipated energy for sub-model 1 for these two cases and the base case can be observed in Figure 5.8. The predicted dissipated energy is a scalar quantity that provides a representative measure of fault activity for a given area of interest. Increase in the initial stress gradients by 10% leads to a significant reduction in the predicted dissipated energy. Similarly, a decrease in the initial stress gradient leads to large increment on dissipated energy.

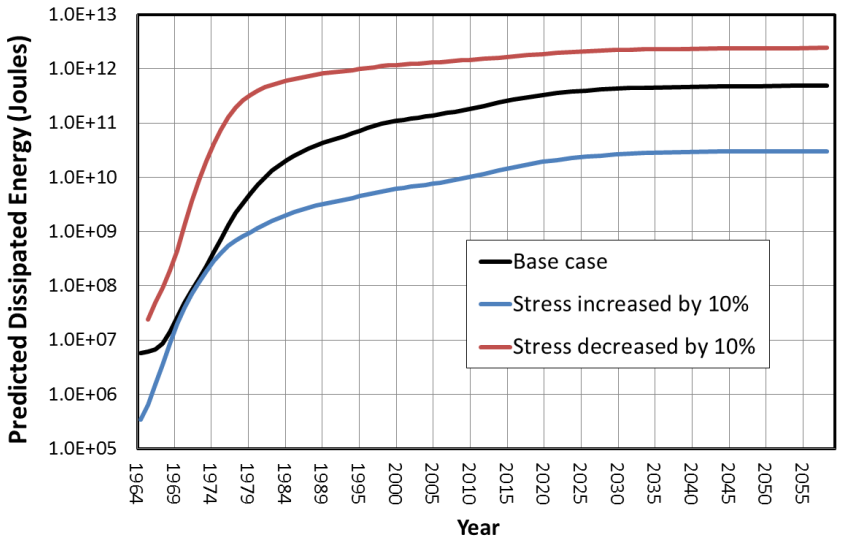

Fig. 5.8. Evolution of predicted dissipated energy for base case G1-C1-D1 with friction coefficient μ=0.48, and the other two cases considered: (i) initial stress gradients increased by 10% and (ii) initial stress gradients decreased by 10%.

As reported in 2013 sensitivity analysis, changing initial stress gradients has a negligible effect on subsidence because compaction, as well as surface subsidence, is caused by depletion and not initial stress values. Depletion applied to the model directly correlates to the change on effective stress which causes deformation.

5.3. Material properties sensitivity studies

The purpose of this sensitivity analysis is to vary mechanical properties and observe the impact in results such as subsidence and dissipated energy. The mechanical properties, Poisson's Ratio (v) and Young's Modulus (E) are modified while keeping compressibility equal to the original (base case). The material property values for the reservoir layers are based on limited test data, and the test data include considerable variability (see dots on Figure 5.9). Hence, these material parameters are not known accurately and the best fit to the test data is used as base case in present analysis. Figure 5.9 shows the values used for this analysis; they are all dependent on porosity. The blue line is the original (base case), while the green and orange represent 33% and 60% increase in Poisson's ratio, respectively. Young modulus is adjusted to keep the uniaxial compressibility (cbu) equal to the base case (lower values are computed compared to base case; see Figure 5.10).

Any variation of mechanical properties requires to re-run the analysis models from scratch. That means that the Global Model (un-faulted) and sub-model-1 have to be run thru geostatic, salt creep, and production scenarios for each case.

Note that only material properties for the reservoir layers are changed in this sensitivity study. The properties for other layers have very small effect on subsidence and fault slip/energy since all depletion associated with production and consequent deformation takes place in the reservoir layers.

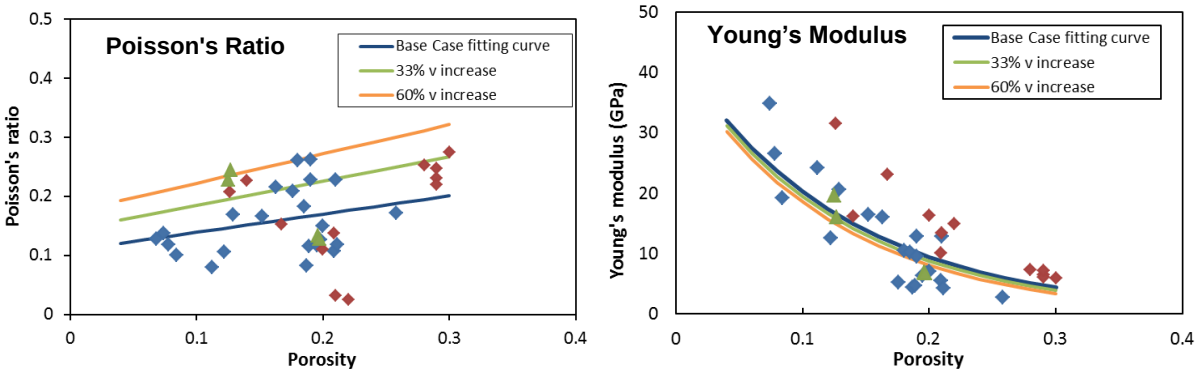

Fig. 5.9. Poisson's ratio and Young's modulus vs. porosity: base case, 33% and 60% higher values for v used in this sensitivity study.

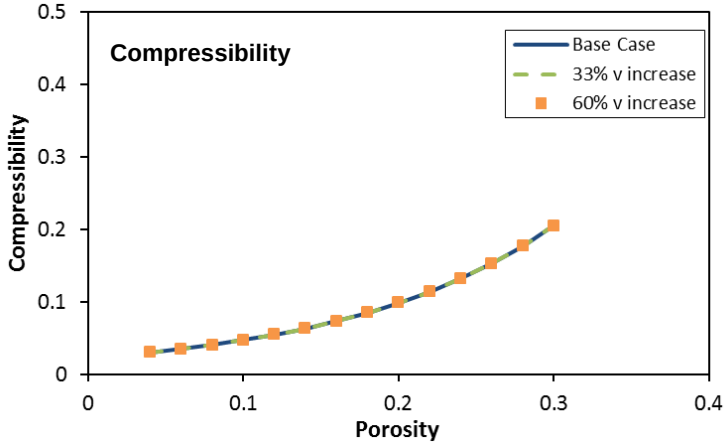

Fig. 5.10. Compressibility vs. porosity: base case, 33% and 60% higher values for v used in this sensitivity study.

The results of this sensitivity analysis show very little variation in terms of subsidence but significant variation in dissipated energy (see Figure 5.11). Subsidence appears to decrease with an increase of Poisson's ratio, and the decrease is less than ~3 cm for the most part as shown in Figure 5.11 (a). Figure 5.11 (b) shows a comparison of subsidence observed in the field vs subsidence predicted by the model. A normalized minimum square distance has been computed for each case, showing almost no difference among the studied cases. In contrast, the dissipated energy varies significantly from each case. Figure 5.11 (c) shows the cumulative dissipated energy thru time in logarithmic scale. Observe that the base case has orders of magnitude larger dissipated energy when compared to the other two cases. Higher Poisson's ratio corresponds to less dissipated energy. Different rock properties can produce similar subsidence bowl but very different fault behavior.

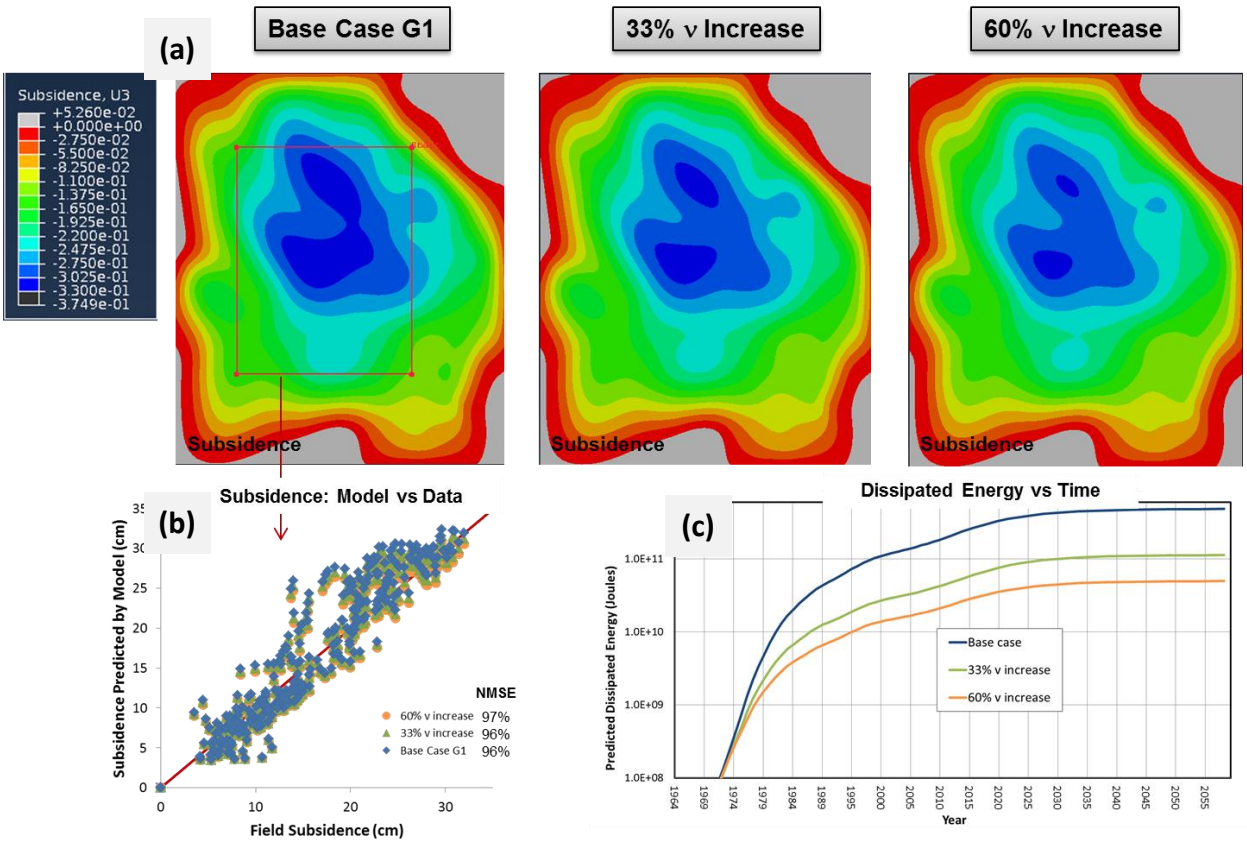

Fig. 5.11. (a) Surface subsidence (m) for year 2012 contour plots; (b) comparison of predicted surface subsidence vs. field data; (c) evolution of predicted dissipated energy in logarithmic scale; for base case, 33% and 60% Poisson's ratio increased.

5.3.1. Mobilized friction angle

In this section, contours for mobilized friction angle are presented (Figure 5.12). Three different locations of the reservoir are chosen from the global model (Figure 5.12 (d)). Rectangles drawn inside the plots show the locations of sub-model-1 and -2. The values represent the angle of a tangent line that touches Mohr's circle (Figure 5.12 (a)). In other words, if the material has a friction angle (strength) lower or equal to this mobilized friction angle in addition to a weak plane with a favorable orientation, then material would fail to generate slip. The circle is built using values of maximum (σ_1) and minimum (σ_3) principal stress. A favorable orientation refers to a rotation of the plane that coincides with the point where the tangent line touches the circle.

Values of mobilized friction angle are higher in sub-model-1 region. Therefore, more strength is necessary to keep favorable oriented faults stable compared to sub-model-2 area. It can also be observed that at the bottom of the reservoir the mobilized friction angle is low, and therefore more stable.

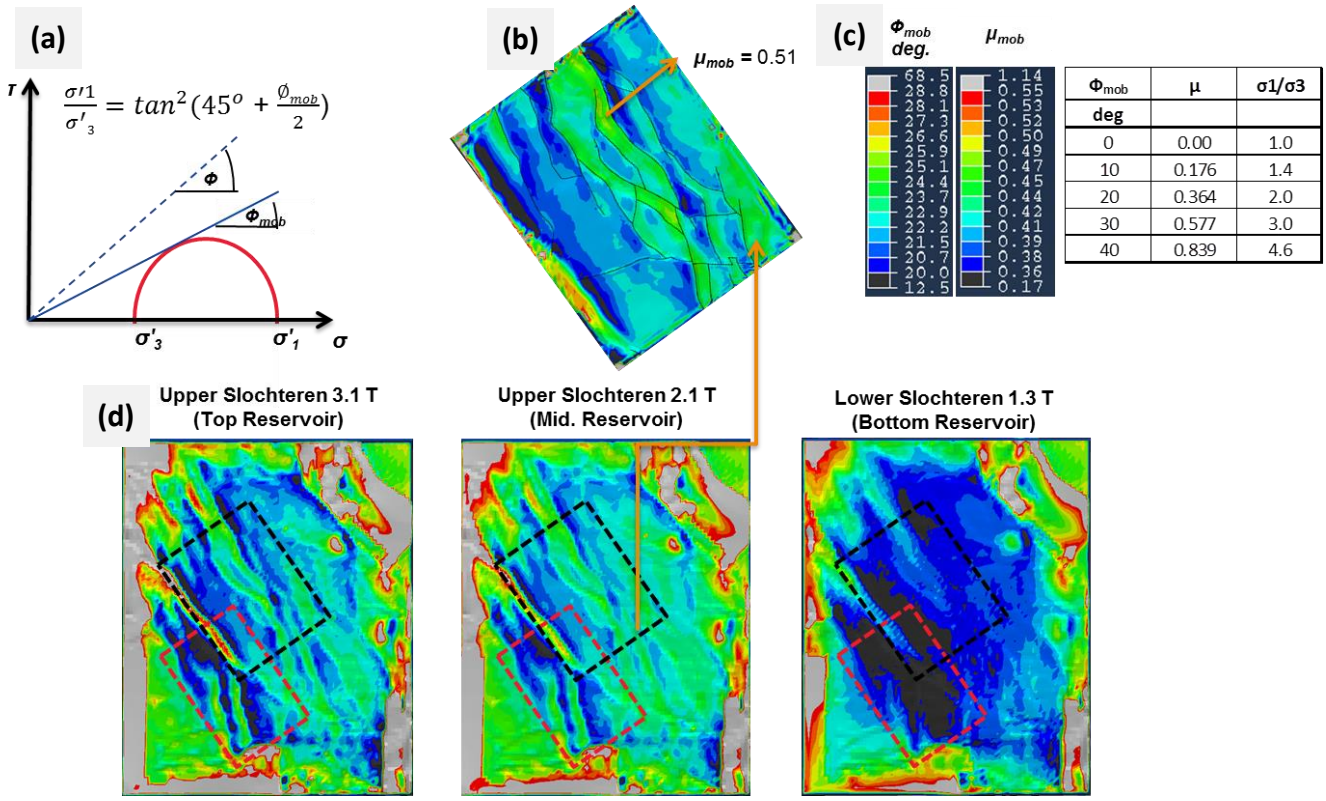

Φ_{mob}	μ	σ1/σ3
deg		
0	0.00	1.0
10	0.176	1.4
20	0.364	2.0
30	0.577	3.0
40	0.839	4.6

Fig. 5.12. (a) Mohr's circle and mobilized friction angle representation; (b) sub-model 1 comparison with global model; (c) mobilized friction angle contour values and corresponding friction value; (d) mobilized friction angle for 3 different reservoir locations (top, middle and bottom).

5.3.2. Stress path

Depletion of a reservoir leads to compaction and deformation, which in turn changes total stress acting on the reservoir. The ratio at which the pore pressure changes along with the horizontal total stress is known as "stress path". Figure 5.13 shows the stress path of Groningen reservoir for base case, 33% and 60% Poisson's ratio increase. It is interesting to observe that the stress path is uniform around the whole reservoir, 0.65-0.7 for base case, 0.55-0.60 for 33% v increase and 0.50-0.55 for 60% v increase.

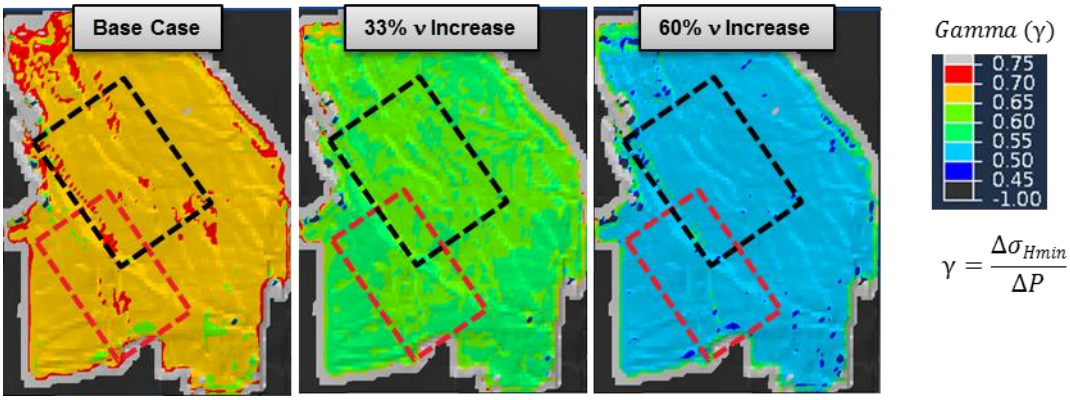

Fig. 5.13. Stress path for base case, 33% and 60% Poisson's increase.

Figure 5.14 (a) shows a stress path contour for base case to observe more clearly the variation of values from 0.65-0.70. Figure 5.14 (b) shows the stress path vs Biot coefficient for a reservoir where it's lateral extent to thickness ratio is greater than 10:1. Each colored line represents a different constant Poisson's ratio. The blank translucent rectangle shows all the possible values of stress path for Groningen's reservoir material properties for a case with a simplified uniaxial deformation. The red and black dash lines correspond to values of the stress path above which depletion would ultimately lead to movement of pre-existing normal faults for coefficient of friction 0.48 and 0.7, respectively. Just a corner of the black rectangle has overpassed the red line. In a uniaxial deformation assumption, just some faults of the Groningen field have stress changes favorable for slip. The red translucent rectangle corresponds to stress path values computed in the 3D geomechanical model. This shows that all faults in the Groningen field have favorable stress changes for slip. Therefore, if a pre-existing fault has a favorable orientation, production induced re-activation should occur; assuming fault strength of $\mu < 0.70$.

As observed previously, 33% and 60% increase in Poisson's ratio gives lower values of stress path. That means that it requires less strength (lower coefficient of friction values) to maintain favorable oriented faults stable.

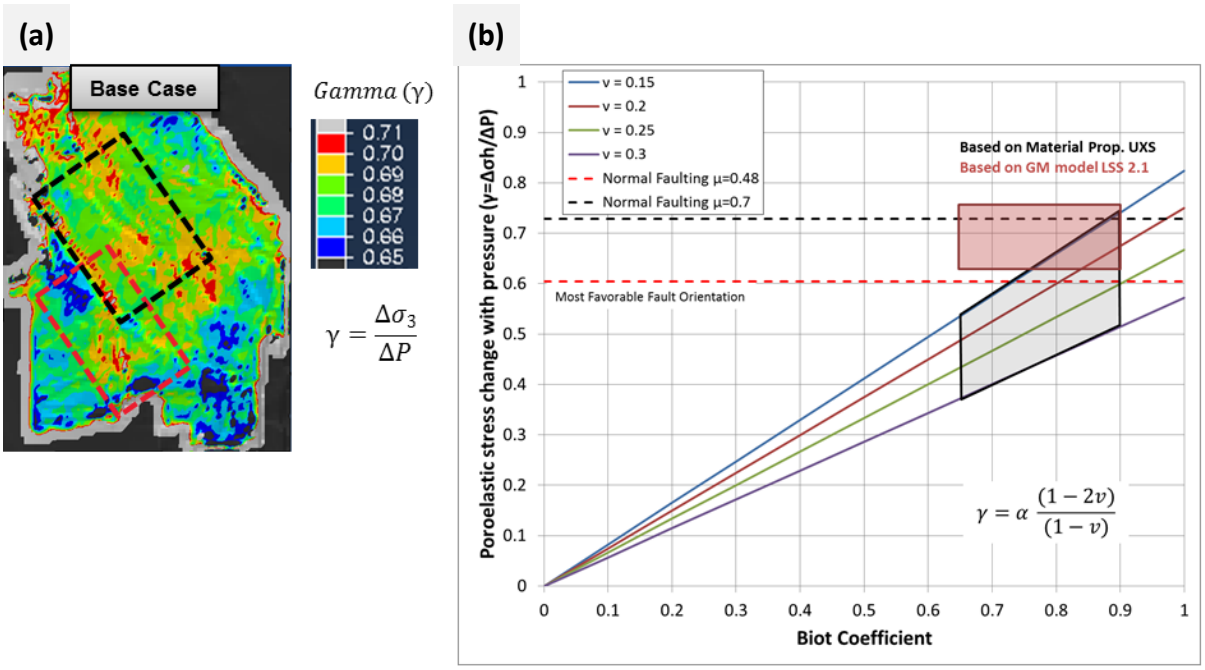

Fig. 5.14. (a) Stress path for base case; (b) Stress path vs Biot Coefficient for different constant Poisson's ratio values. All lines assume a reservoir where its lateral extent to thickness ratio is greater than 10:1 (uniaxial compaction). Black rectangle encompasses all possible values based on Groningen reservoir material properties (base case) with the uniaxial compaction assumption. Red rectangle represents all values obtained from the geomechanical model (base case).

6. Overview of Integration with Seismological Models

In the 2013 study, the same scaling factor could be used for both sub-model-1 and -2 to relate the observed seismic energy release to the predicted dissipated frictional energy. The present approach to correlate a modelled geomechanical quantity to earthquake activity differs from the methodology employed in 2013 which attempted to forecast the amount of energy that would be released in a given area.

In the present study, the focus of the geomechanical and seismological model integration is to develop an earthquake activity map that forecasts the total number of earthquakes expected to occur in a given year and where they are likely to occur. The activity is strictly related to the number of earthquakes and does not account for the earthquake magnitude. Similar to the approach recently taken by Shell (November 2015 HRA) we investigate the relationship between a modeled geomechanical quantity (fault slip/energy or compaction) and the observed number of earthquakes, rather than the observed earthquake moment/energy. The distribution of possible event magnitudes and seismic energy released is assessed using a Gutenberg-Richter model discussed in a separate report (DeDontney, 2016). Figure 6.1 shows the comparison of the spatial distribution of the geomechanical model moment and observations of moment release and number of events.

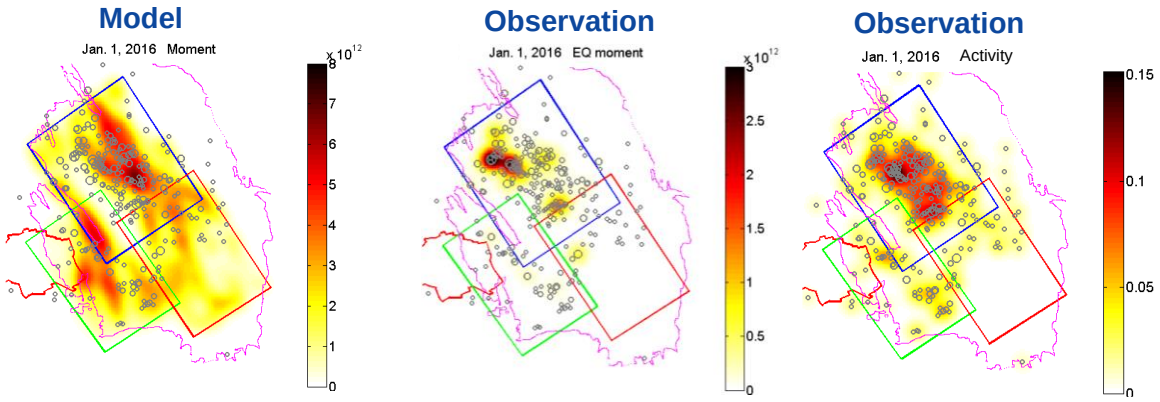

Fig. 6.1. Comparison of 2015 geomechanical modeled moment release and observations of moment release and number of events. There is a poor correlation between the model and the observations of moment but a better (although non-linear) correlation with activity. All figures use a Gaussian kernel of 1 km standard deviation to distribute the model results/observations over a spatial area.

The motivation for a model comparison with activity comes from the physics that are being captured/neglected by the geomechanical model. The quasi-static geomechanical model cannot capture the true heterogeneity and the processes that take place during an earthquake so it is not reasonable to expect it to properly reflect the time release of energy in the subsurface (i.e. predict location and magnitude of earthquakes). However, the model well represents where faults are being stressed and the magnitude of that force is captured by the slip evolution. An earthquake is more likely to nucleate in an area that is highly stressed so the geomechanical model is a good proxy for the availability of earthquake nucleation sites. For a complete discussion of the motivation and development of activity models see DeDontney, 2016.

Shell has developed an activity map based on compaction, so in addition to the fault based activity model we also consider an activity model based on the compaction derived from the global model. Reservoir compaction is simply the change in reservoir thickness at an x-y location in the reservoir and is the result of the pore pressure reduction and the porosity dependent material properties that vary throughout the reservoir.

Whether compaction or fault based slip is considered, maximum likelihood estimation (MLE) was used to build a Poisson process model and determine the best-fit model parameters. This technique assumes a form for the activity, $\lambda = f(x, \dot{x})$, where x is compaction or moment, and incorporates the predicted activity value at each point in space and time where an earthquake was observed. Various forms for $f(x, \dot{x})$ were considered including polynomial and exponential fits. In addition to the functional form, a choice about a reference year must be made for both compaction of fault slip based approaches.

6.1. Slip moment based seismological model

The sub-models allow slip to evolve in response to the specific reservoir conditions and fault orientation at that point in space. Due to the overlap of the sub-models, each model is cropped to prevent data duplication in the merged dataset. We can either use the slip moment (slip*shear modulus) as the geomechanical input or we can use the dissipated fault energy (slip*shear stress). Qualitatively there is little difference between the slip and energy metrics because they are very well correlated over time.

Seismic moment, M, is determined via the equation $M = GAd$ where G is the shear modulus, A is the area and d is the slip displacement. A map of moment release per unit area is made by assuming a shear modulus and distributing each node's moment (each node has a slip and area associated with it) over an area using a Gaussian kernel. The spatial distribution is performed to (1) account for small/subseismic faults not included, (2) account for the uncertainty in earthquake location, and (3) obtain a point source representation (vs. line source) as required by the PSHA implementation. An example result is shown in Figure 6.1a, and the choice of kernel length scale will result in a map with more or less localization.

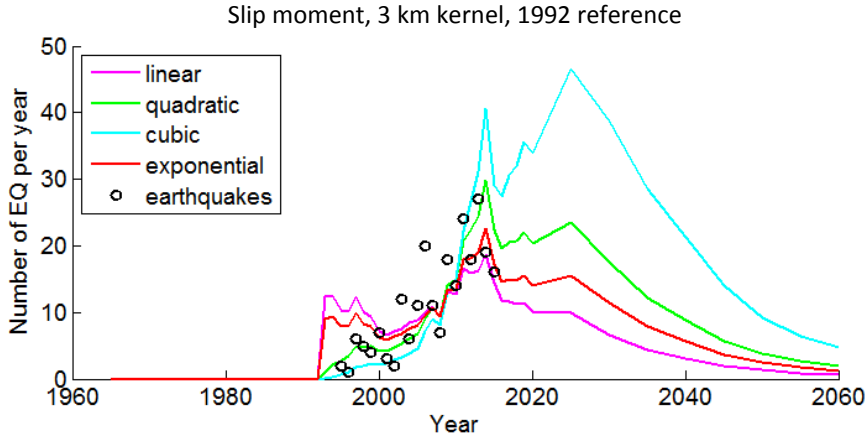

Fig. 6.2. Comparison of the model predicted activity to the observed earthquake activity for a variety of slip moment based activity models. Forecast based on the 33 Bcm production scenario.

Once maps of moment distribution in space and time are made a MLE is performed and Figure 6.2 shows the fit of the model to the total number of earthquakes. The spatial distribution of activity is shown in Figure 6.3 for the case of the quadratic model. There is good correlation between the observations and the predicted activity and many of the earthquakes occur in the reddest portions of the map. There are however some earthquakes that occurred in areas where very low activity is predicted.

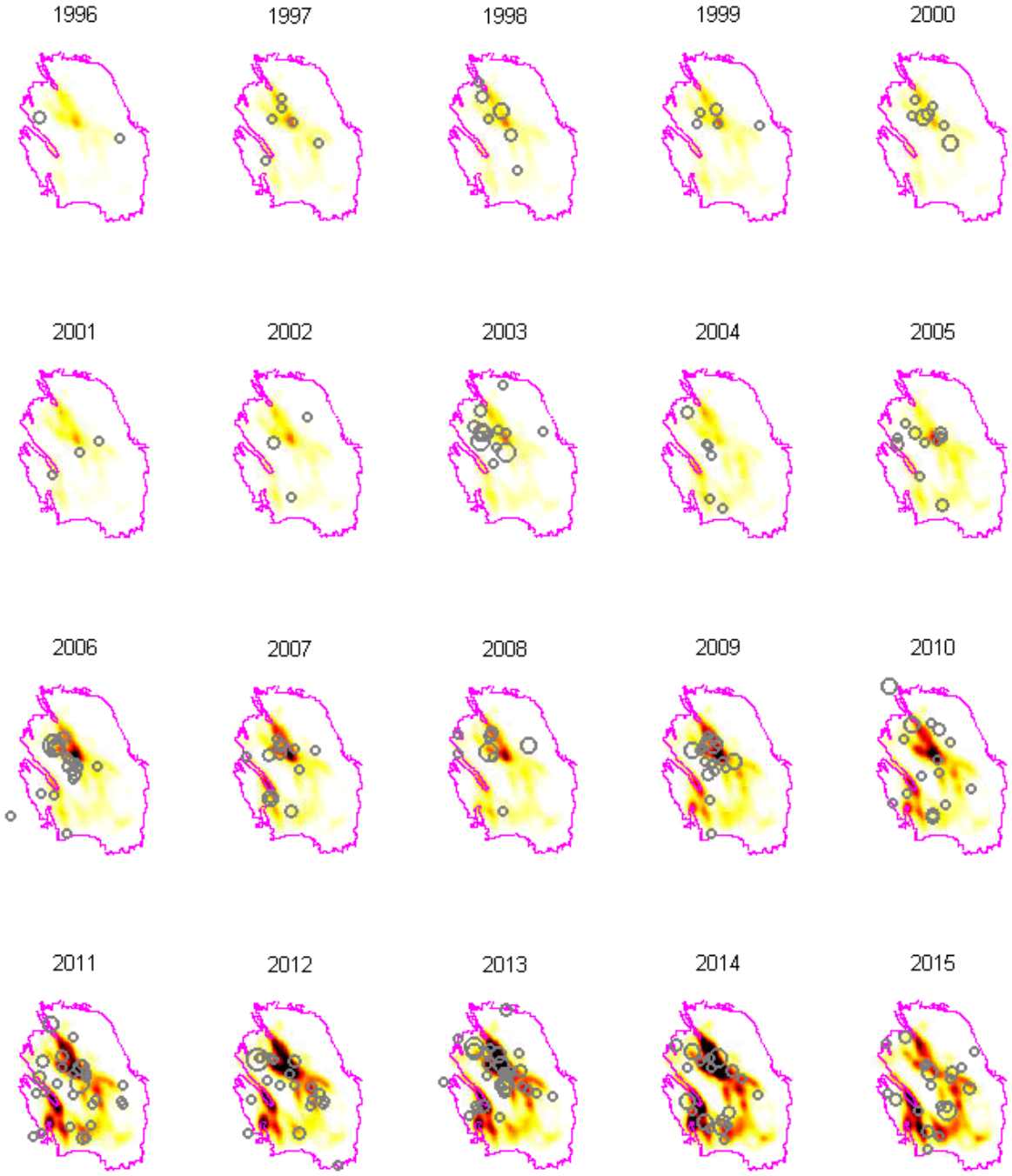

Fig. 6.3. Spatial distribution of activity compared with historically observed earthquakes for the quadratic fit to a 3km kernel (3σ = 3 km) with slip referenced to Jan 1 of 1992.

6.2. Compaction-based seismological model

The same process is used to determine a compaction based activity model. A comparison of Figures 6.2 and 6.4 shows that both types of input geomechanical data are capable of producing a decent fit to the historical seismicity. The exponential fit does not result in a good fit for the moment based models but does result in a good fit for the compaction based models. The fault based cubic activity model results in a forecast of higher activity rate than any of the compaction based activity models.

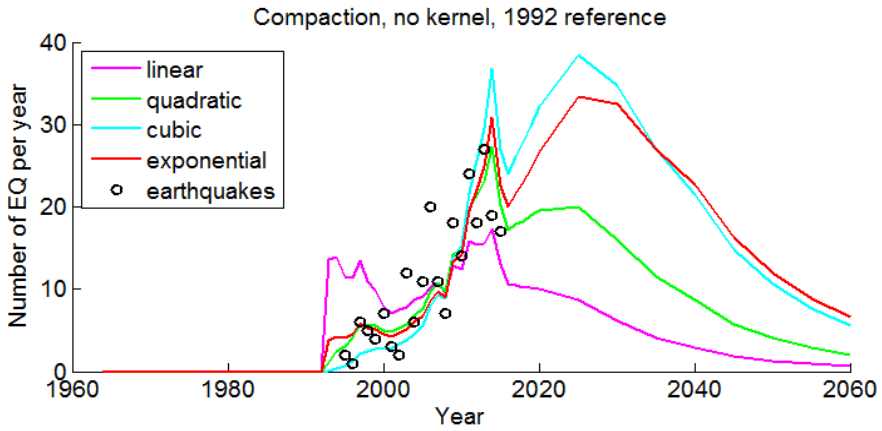

Fig. 6.4. Comparison of the model predicted activity to the observed earthquake activity for a variety of compaction based activity models. Forecast is based on the 33 Bcm production scenario.

A large difference between the fault based vs. the compaction based model is the relative localization of the input data. Fault slip is highly localized but compaction is a very diffuse quantity. The result is that compaction based activity models are more diffuse so there is generally a reasonable level of activity everywhere (Figure 6.5). The result is that there are fewer instances of earthquakes occurring in areas of very low predicted activity, but observed earthquakes also do not occur in the reddest portions of the map.

6.3. Future and on-going work for model integration

Future work should be done to determine the validity of the use of one form of activity model over another. Shell proposes that there is a physical motivation for using an exponential fit but there are many avenues of research to pursue that could lead to a motivation for a different activity model.

A variety of metrics are currently under consideration to determine which activity model best represents the data but the different metrics do not consistently favor one model over all others. It is possible that the best activity model is dependent on both compaction and fault based moment. Work should evolve to consider a joint parameter inversion and assess which model is the best.

Fig. 6.5. Spatial distribution of activity compared with historically observed earthquakes for the exponential fit to the compaction based activity model with compaction referenced to Jan 1 of 1992.

7. Discussion and Conclusions

New 2015 sub-models were developed to include nearly all mapped faults; the offsets at each fault are also explicitly included as part of the FE mesh. Sub-models-1 and -2 cover the same region of the field as in 2013 study. Additional sub-model-3 was developed to improve spatial coverage to allow better integration with seismological models. The 2015 sub-models include nearly all mapped faults within their domain, with approximately 150 faults in each sub-model. Pressure mapping procedure used to map pore pressure data from NAM/Shell's MoRes reservoir simulator to the FE mesh has been improved using layer information from MoRes. Material properties of the thin heterolithic layers within the reservoir were changed to those of the surrounding reservoir rock from original undrained stiff properties to better represent this material. There are no changes in the global model; this model was developed and validated against field subsidence and strain data in 2013 study.

The new models were used to better understand subsurface behavior related to production induced compaction and fault reactivation. Several production scenarios were analyzed and compared on a relative basis based on the predicted dissipated energy. The slip and contact force data for all FE nodes on the fault surfaces were output for use as input to the seismological models.

The model results show the fault offset is a key controlling factor for production induced fault slip. A fault with offset can develop slip due to differential compaction on two sides even if the dip and azimuth are not favorable for fault slip. This leads to more slip on significantly more faults compared to that in 2013 models without offsets.

Sensitivity studies were also performed to understand impact of various modeling uncertainties such as friction coefficient, material properties and initial stress. Results from sensitivity studies are used for either relative comparison or correlations in seismological modeling, and not on an absolute basis.

7.1. Future work

URC is continuing work on improving the integration between the geomechanical models and seismological models for hazard and risk analysis, and continues looking into alternative quasi-static metrics to develop improved correlations with seismicity. The geomechanical models will also be used to evaluate any additional production scenarios as necessary.

Acknowledgements

ExxonMobil Upstream Research Company (URC) would like to acknowledge support for this study from ExxonMobil International Limited (EMIL) and Nederlandse Aardolie Maatschappij B.V. (NAM). The authors would also like to acknowledge the guidance received from Erika Biediger (URC), Bruce A. Dale (ExxonMobil Production Company), and William E. Kline (URC) throughout the course of this study. Thanks to Jan Van Elk (NAM), Dirk Doornhof (NAM), Rob van Eijs (NAM), Clemens Visser (NAM), and Peter van den Bogert (Shell) for the data provided and insightful comments.

References

- Bogert, P.A.J. van den, van Eijs, R.M.H.E (2013), *Groningen fault stability assessment*, Confidential report, Shell Global Solutions International B.V., Rijswijk, the Netherlands.
- Bogert, P.A.J. van den (2015), *Impact of various modelling options on the onset of fault slip and fault slip response using 2-dimensional Finite-Element Modelling*, Report SR.15.11455, Shell Global Solutions International B.V., Rijswijk, the Netherlands.
- Breunese, J.N., van Eijs, R.M.H.E., de Meer, S., Kroon, I.C. (2003), *Observation and prediction of the relation between salt creep and land subsidence in solution mining. The Barradeel case*, Solution Mining Research Institute Fall 2003 Conference, Chester, UK.
- Chan A.W., Zoback M.D. (2007) *The Role of Hydrocarbon Production on Land Subsidence and Fault Reactivation in the Louisiana Coastal Zone*, Journal of Coastal Research, v. 23 (3), pp. 771 – 786.
- DeDontney, N.L. (2011), *Branch faulting in subduction and strike-slip setting*, Ph.D. thesis, Harvard Univ., Cambridge, MA, USA.
- DeDontney, N.L. (2016), Groningen seismological model derived from 3D fault based geomechanical model, Research Report, ExxonMobil Upstream Research Company, Spring, TX, USA.
- Dieterich, J.H. (1978), *Time-dependent friction and the mechanics of stick-slip*, Pure Appl. Geophysics, v. 116(4-5), pp. 790-806.
- Dost, B., Goutbeek, F., van Eck, T., Kraaijpoel, D. (2012), *Monitoring induced seismicity in the North of the Netherlands: status report 2010*, KNMI Scientific report, WR 2012-03.
- Eck, T. van, Goutbeek, F., Haak, H., Dost, B. (2006), *Seismic hazard due to small-magnitude, shallow-source, induced earthquakes in The Netherlands*, Engineering Geology, v. 87, pp. 105-121.
- Griffith, W.A., Sanz, P.F., Pollard, D.D. (2009), *Influence of outcrop scale fractures on the effective stiffness of fault damage zone rocks*, Pure Appl. Geophysics, v. 166(10-11), pp. 1595-1627.
- Grueschow, E.R., Dale, B.A., Pakal, R., Haeberle, D., Wallace, J., Asmann, M. (2008), *Well operability limits for managing production from deepwater reservoirs*, International Petroleum Technology Conference, Kuala Lumpur, Malaysia, IPTC-12421.
- Hansen, F.D., Pfeifle, T.W. (1998), *Database of Mechanical and Hydrological Properties of WIPP Anhydrite Derived from Laboratory-Scale Experiments*, Technical Report SAND98-1714, Sandia National Laboratories, Albuquerque, NM, USA and Livermore, CA, USA.
- Hettema, M.H.H., Schutjens, P.M.T.M., Verboom, B.J.M., Gussinklo, H.J. (1998), *Production-induced compaction of sandstone reservoirs: the strong influence of field stress*, SPE European Petroleum Conference, The Hague, The Netherlands, SPE-50630.
- Hettema, M.H.H., Schutjens, P.M.T.M., Verboom, B.J.M., Gussinklo, H.J. (2000), *Production-induced compaction of a sandstone reservoir: the strong influence of stress path*, SPE Reservoir Eval. & Eng., v. 3, pp. 342-347.
- Hsu, S.Y., Searles, K.H., Aylor, A. (2011), *Fatigue-based tubular connection performance for a CSS application*, SPE/IADC Drilling Conference, Amsterdam, Netherlands, SPE-139785.

- Hsu, S.Y., Searles, K.H., Liang, Y., Wang, L., Dale, B.A., Grueschow, E.R., Spuskanyuk, A., Templeton, E., Smith, R.J., Lemoing, D.R.J. (2010), *Casing integrity study for heavy-oil production in cold lake*, SPE Annual Technical Conference, Florence, Italy, SPE-134329.
- Hsu, S.Y., Venkataraman A., Sze E.K. and Searles K.H., inventors, *Integration of geomechanics and seismic analysis for passive seismic feasibility analysis*, U.S. Patent No. US8121792 B2.
- Lele, S.P., Searles, K.H., Hsu, S.Y., Garzon, J.L., Sanz, P.F. (2015), *Geomechanical Analysis to Evaluate Groningen Production Scenarios*, Report URC.2015.050, ExxonMobil Upstream Research Company, Spring, TX, USA.
- Mobach, E., Gussinklo, H.J. (1994), *In-situ reservoir compaction monitoring in the Groningen field*, Eurock SPE/ISRM Rock Mechanics in Petroleum Engineering Conference, Delft, The Netherlands, SPE-28094.
- Muntendam-Bos A.G., de Waal, J.A. (2013), *Reassessment of the probability of higher magnitude earthquakes in the Groningen gas field*, KNMI confidential final report dd. 16-01-2013.
- NAM (2013a) Groningen Petrel model.
- NAM (2013b) Groningen material test data for reservoir layers.
- NAM (2013c), Email communication with C. Visser on material properties for rock layers other than the reservoir layers, April 2013.
- NAM (2013d), Email communication with R. van Eijs on creep properties for Groningen halite layers, June 2013.
- NAM (2013e), *Groningen virgin in-situ stress condition*, Groningen In-Situ Stress –XOM v2.pptx.
- NAM (2013f), MoRes pore pressure data for various history match and production forecast scenarios, Excel spreadsheets.
- NAM (2013g), *Surface subsidence data*, Subsidence_data_for_calibration.xls.
- NAM (2013h), *Reservoir layer strain data*, FSMT_strain_measurements.xls.
- NAM (2013i), *Groningen seismicity data*, Groningen Seismicity 1986-2013.xls.
- NAM (2013j), Report to the technical guidance committee (TBO) study TBO5 on subsurface aspects of induced earthquakes in Groningen field (2013).
- Nygaard, K.J., Cardenas, J., Krishna, P.P., Ellison, T.K., Templeton-Barrett, E.L. (2013), *Technical considerations associated with risk management of potential induced seismicity in injection operations*, 5to. Congresso de Producción y Desarrollo de Reservas, Rosario, Argentina.
- Orlic, B., Van Eijs, R., Scheffers, B. (2001), *Geomechanical modelling of the induced seismicity for a gas field*, 63rd EAGE Conference and Technical Exhibition, Amsterdam (2001), Paper P604.
- Sanz, P.F., Lele, S.P., Searles, K.H., Hsu, S.Y., Garzon, J.L., Burdette, J.A., Kline, W.E., Dale, B.A., Hector, P.D. (2015), *Geomechanical analysis to evaluate production-induced fault reactivation at Groningen gas field*, SPE Annual Technical Conference, Houston, TX, USA; SPE-174942-MS.
- Schoonbeek, J.B. (1976), *Land subsidence as a result of natural gas extraction in the province of Groningen*, SPE European spring meeting, Amsterdam, The Netherlands, SPE-5751.
- Simulia (2014), *Abaqus user and reference manuals*, Dassault Systèmes Simulia Corp., Providence, RI, USA.
- Suckale, J. (2010), *Moderate-to-large seismicity induced by hydrocarbon production*, The Leading Edge, v. 29(3), pp. 310-319.

- Templeton, E.L., Bhat, H.S., Dmowska, R., Rice, J.R. (2010), *Dynamic Rupture through a Branched Fault Configuration at Yucca Mountain, and Resulting Ground Motions*, Bulletin of the Seismological Society of America, v. 100(4), pp. 1485-1497.
- World stress map.